LEVEL

EVOLUTION OF TURBULENCE BY THREE-DIMENSIONAL NUMERICAL PARTICLE-VORTEX TRACING

by

Benoit Couët

SU-IPR Report No. 793

August 1979

INSTITUTE FOR PLASMA RESEARCH
STANFORD UNIVERSITY, STANFORD, CALIFORNIA

EVOLUTION OF TURBULENCE BY THREE-DIMENSIONAL
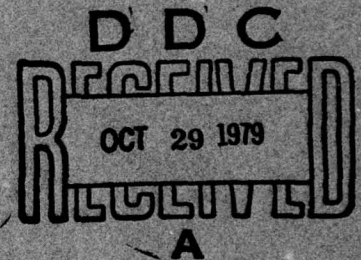
NUMERICAL PARTICLE-VORTEX TRACING

by

Benoit Couët

SU-IPR Report No. -793

August 1979

190

N00014-78-C-0272

Institute for Plasma Research
Stanford University
Stanford, California

332630

ACKNOWLEDGMENTS

I would like to express my deep gratitude to my parents for their constant encouragement through my graduate studies and to my research supervisor, Professor Oscar Buneman, for his teaching, support and scientific insights in the course of my Stanford career so far.

I am indebted to Mr. Earl Knechtel and to Dr. Harvard Lomax, from NASA-Ames Research Center, for providing my first contact with this research area and to Dr. Anthony Leonard, also from NASA, for acting as my second research supervisor and for his constant encouragement to improve the work. Thanks go to Professors Joel Ferziger, George Homsy, and Joseph Oliger for serving on my Graduate Special Committee. They provided me with many useful suggestions. Thanks are due to Drs. Robert Rogallo and Alan Wray who acquainted me with the computer at NASA-Ames and to Mr. Tony Hasegawa for his help in using the graphics system. Heartfelt appreciation is extended to Ms. Joanne Tisch for her patient and very skillful typing.

ABSTRACT

A new method for the numerical simulation of three-dimensional incompressible flows is described. Our vortex-in-cell (VIC) method traces the motion of the vortex filaments in the velocity field which these filaments create. The velocity field is not calculated directly by the Biot-Savart law of interaction but by creating a mesh-record of the vorticity field, then integrating a Poisson's equation via the fast Fourier transform to get the stream function and generating a mesh-record of the velocity field. The computed scales of motion are assumed to be essentially inviscid. Viscous or subgrid-scale effects are incorporated into a filtering procedure in wave vector space.

Three computational experiments were pursued in three-dimensional space. The velocity of translation of a single vortex ring was measured and compared with the Biot-Savart law. The agreement was excellent. Next, the evolution in time of an infinite periodic array of closed vortex filaments (Taylor-Green) was studied. The results were compared with those obtained previously by the spectral method. The Fourier mode spectra were in very good agreement. The third simulation follows a mixing layer from an initial state of uniform vorticity with two- and three-dimensional small perturbations. Streamwise perturbations lead to the usual roll-up of vortex patterns with spanwise uniformity. Combined with spanwise perturbations, it was observed that the third dimension is extremely important in the evolution of a mixing layer even though it is an "ignorable coordinate" in the idealized uniform shear flow. Substantial streamwise vortex deformation and stretching is generated by the spanwise perturbations.

TABLE OF CONTENTS

Chapter I

INTRODUCTION

It is becoming evident that a proper understanding of turbulence
will depend heavily on numerical methods of solving the Navier-Stokes
equations in three dimensions at high Reynolds numbers. In this work,
we describe a new method for the numerical simulation of three-dimen-
sional incompressible flows. Our approach differs from other numerical
fluid simulations in that, rather than solving the Navier-Stokes equa-
tions on an Eulerian mesh, we emphasize the vortical part of the flow
by solving the vorticity equation, using a hybrid method.

Numerics means discretization, and in breaking up the fluid or gas
into discrete elements, one can, and should, make use of the fact that
vortices naturally preserve their identity. Even when the vorticity
is itself continuous, as in laminar shear flow, the parametrization
of fluid elements according to (infinitesimal) vortex filaments helps
greatly toward programming hydro- or gas-dynamics into the computer.

Historically, the first numerical calculation using a two-dimen-
sional discrete vortex element method was made by Rosenhead[1], using
a few vortices. Since then, the same method has been applied to various
two-dimensional shear flows and is summarized in a literature survey by
Fink and Soh[2]. Most of these efforts were directed toward understand-
ing the time evolution of finite-area vorticity regions or the initial
break-up of the laminar shear layer (usually done for short times or
small regions with periodic boundary conditions). Some of these recent
computer calculations involved thousands of vortices[3,4,5]. Other impor-
tant flows were also considered: two-dimensional turbulence[6,7,8,9],
separated flows[10], and stratified flows in both homogeneous and porous

media[11,12].

A flow field can be represented to any required precision by a
sufficiently large assembly of discrete vortices and the time evolution
of the field can be transcribed into a kind of particle mechanics of
these vortices. If one integrates analytically, in two or three dimen-
sions, the Poisson's equation relating the velocity field to the vor-
ticity field (see Eq. 2.4), the result is a direct Biot-Savart integra-
tion or summation over all the vortices making the vorticity field[34].
With N vortices, a time step in a direct summation scheme will in-
volve evaluating N-1 terms for the velocity which displaces a single
vortex, and thus on the order of N×N terms per time step. For large
N , such a code will be very time consuming. Thus, the two-dimensional
mixing layer calculation of Ashurst[7], where the number of vortices was
increased from one to eight hundred, required two hundred and fifty hours
of computing time on a CDC 6600. Understandably, previous direct summa-
tion calculations were much more modest. Michalke[13] studied the
linear and partly nonlinear instability of seventy-two vortices arranged
on three close parallel lines. Acton[14], still in two dimensions,
studied the same problem, but with ninety-six vortices arranged initially
on four close sinusoids, and ran for a longer time. In Acton's simula-
tion, the sinusoid is seen to amplify, break and form two vortex blobs
which then merge into one.

An alternative method for time-stepping a set of parallel vortices
in two dimensions, the cloud-in-cell (CIC) method as it is sometimes
called, was described by Christiansen[15,5,16]. In this algorithm, the
basic variables are still the positions and strengths of the vortices,
but now a grid is laid down in the plane perpendicular to the vortex

filaments and covering the flow area. At every time step, a grid vorticity is generated by distributing the vorticity from each vortex over the four neighboring grid points suitably weighted. This grid vorticity is then used to generate a grid stream function by solving Poisson's equation. The stream function is differenced on the grid to produce a velocity field, which is finally interpolated back to the vortex positions. The advantage of this apparently rather elaborate detour is that the Poisson inversion can be accomplished by fast Fourier transform techniques. If the grid is $M \times M$, this is an order $M^2 \log_2 M$ calculation. Since in a typical 2-D calculation today, the number of grid squares $M \times M$ is some small multiple of the total number of vortices N, this required on the order of $N \log_2 N$ operations per time step. The smoothing and interpolations take of the order N operations. When N is large, $N \log_2 N$ is considerably smaller than $N \times N$.

A disadvantage of the cloud-in-cell method (as against the direct interaction method) is having to watch out for grid effects. In particular, "aliassing" should be avoided or minimized, as in the case of conventional Eulerian fluid simulations[28,57]. To counteract grid effects, Wang[17] did some extensive two-dimensional simulations in which he improved on the CIC method by first, using cubic splines for interpolation (i.e. referring to the nearest 16 grid points for each vortex node rather than to the nearest 4) and second, applying a gaussian shape factor or "filter" in wave vector space. The insensitivity of the resulting potential contours or flow lines to the underlying grid is shown in some diagrams presented in[17].

The "filter" can serve a dual purpose in vortex methods. It obviously helps to de-emphasize the high harmonics which are the most

3

sensitive to grid effects. But it also spreads the individual vortex strands from singular filaments to tubes of finite thickness. It was pointed out[18] that, because high induced velocities occur when two vortices come close together, unless a finite core radius is used, the accuracy of the discrete vortex element method does not improve as more and more elementary vortices are employed to represent a given vorticity field. This small cut-off radius represents the smallest scale we can compute. The effect is not cumulative; the vorticity is spread a little way only.

It is well known in turbulence theory that energy is transferred from large to small scale through the three-dimensional vortex-stretching mechanism. Although many explanations have been given[19], there seems to be little quantitative support. It has also long been understood that jets and wakes can be idealized by a series of vortex rings, but few studies have been carried out in terms of three-dimensional vorticity theory.

In three dimensions, the direct summation scheme has been applied to a small number of simple vortex filaments[20,21,22,23], but at considerable cost because of the time required to sum all the mutual Biot-Savart interactions between the many elements in all the filaments. In our method, the velocity field is not calculated directly by the Biot-Savart law of interaction but by creating a mesh-record of the vorticity field, then integrating a Poisson's equation to generate a mesh-record of the velocity field. The "cell" or "mesh" method speeds up the calculations of the interactions and allows the three-dimensional vortex pushing method to be applied to a space densely filled with vortex filaments, each filament being resolved in fine detail along its length.

Some features of our method are the following: a) each vortex of finite size has a gaussian vorticity distribution, which is achieved by combining quadratic spline interpolation with spectral shaping in three-dimensional wave vector space where Poisson's equation for the velocity field is solved; b) a machine-coded FFT is applied to transform vorticity records from real space to wave vector space, and to transform back velocity records every time step; c) only the spline coefficients of the physical variables are accumulated or recorded on grid points. Good subgrid accuracy is achieved through the spline interpolation, minimizing grid effects and preventing numerical instability. Some of the basic advantages of our discrete vortex element method over the finite-difference methods for numerical simulation of flows are as follows: a) the method lends itself to simulation of flows at high Reynolds number; b) it eliminates the necessity to solve for the irrotational flow domain, which remains passive; c) it eliminates the Courant-Friedrichs-Levy (CFL) condition, which imposes a time-step limitation based upon the arbitrarily chosen mesh size instead of the physical time scale based upon vortex interactions.

Basically, three computational experiments were pursued. The first one involves vortex rings. The velocity of translation of a single vortex ring in three-dimensional space was measured in a vortex-in-cell (VIC) run. This can also be calculated analytically, at some cost, using the well-known Green's function method (a Lagrangian method using the Biot-Savart law). We compare the results of the two methods, (see Chapter IV, section 1).

The second experiment considers a particular periodic vortex pattern due to Taylor and Green[24]. After attempting a perturbation

5

analysis to trace the evolution of this flow, it appeared that, as in Taylor and Green's original work, such an analysis would fail to provide medium to large time solutions, or high Reynolds number solutions. Our vortex-in-cell method was used to print out Fourier mode energy and enstrophy (mean square vorticity). These results were compared with a purely spectral (Galerkin) method, most appropriate to simulate such a naturally periodic flow. Also, a movie tracing the vortex lines in three-dimensional space was produced directly from our vortex-in-cell method, (see Chapter IV, section 2).

Our last experiment is related to the evolution of a mixing layer from an initial state of uniform vorticity with simple two- and three-dimensional small perturbations. We expect the streamwise perturbations, where spanwise uniformity is maintained, to lead to the usual roll-up of vortex patterns[25,26,27]. Combined with a spanwise perturbation of the same type, streamwise distortions of the vortex filaments occur. Again, a movie tracing the vortex filaments in three-dimensional space was produced.

An outline of the remaining chapters of our work is as follows. The fundamentals of vorticity dynamics relevant to our technique are discussed in Chapter II and a description of the computational method is given in Chapter III. In Chapter IV, the results of computational experiments are presented and discussed while conclusions and suggestions are given in Chapter V.

Chapter II

BASIC PRINCIPLES

We assume unbounded incompressible flow, fully periodic in each
of the three dimensions. Starting with the incompressible Navier-
Stokes equations where we assume no external forces, the equation of
motion of the flow field is given by:

$$\frac{D\vec{u}}{Dt} = -\frac{1}{\rho} \nabla p + \nu \nabla^2 \vec{u} \qquad (2.1)$$

where the "material acceleration" is defined: $\frac{D\vec{u}}{Dt} \equiv \frac{\partial \vec{u}}{\partial t} + \vec{u} \cdot \nabla \vec{u}$.
Rather than solving (2.1) on an Eulerian mesh, we want to trace the
motion of the vortex filaments in the velocity field these filaments
create. The collection of vortex filaments in each periodic box forms
the vorticity field, $\vec{\omega} = \nabla \times \vec{u}$. We therefore solve the incompressible
vorticity equation, obtained by taking the curl of (2.1):

$$\frac{D\vec{\omega}}{Dt} = \vec{\omega} \cdot \nabla \vec{u} + \nu \nabla^2 \vec{\omega} \qquad (2.2)$$

By using the equation of continuity,

$$\nabla \cdot \vec{u} = 0 \qquad (2.3)$$

we find that the velocity field can be determined kinematically from

$$\nabla^2 \vec{u} = -\nabla \times \vec{\omega} \qquad (2.4)$$

In the following, we use the large-eddy simulation approach[28] where
one calculates precisely the large-scale motions and models approxi-
mately the effects of the finer subgrid scales. The separation of
the large and small eddies mathematically can be achieved by filter-
ing[29]. If $\widetilde{f}$ is some flow field containing all the scales, we

7

define the large-scale or resolvable-scale component of $\widetilde{f}$ to be a convolution of $\widetilde{f}$ with a filter function $G(\vec{r})$,

$$ f(\vec{r}) = \iiint G(\vec{r} - \vec{r}') \, \widetilde{f}(\vec{r}') \, d\vec{r} \qquad (2.5) $$

In the present method, the computed scales of motion are assumed to be essentially inviscid. Any actual viscous effects are on a subgrid scale and are incorporated into the filtering procedure described in more detail in the next chapter.

From Helmholtz's theorem, the motion is purely kinematic and the vortex filaments follow material lines. Also, by definition of $\vec{\omega}$, $\nabla \cdot \vec{\omega} = 0$, and Kelvin's theorem states that, in an ideal fluid, the velocity circulation Γ around a closed "fluid" contour is constant in time, that is $\dfrac{d\Gamma}{dt} = 0$ where

$$ \Gamma = \oint \vec{u} \cdot d\vec{\ell} = \iint \vec{\omega} \cdot d\vec{A} \qquad (2.6) $$

Here A is the cross-section area of the filament. In particular, the effective vorticity field $\vec{\omega}$ in each periodic box is obtained from the actual vorticity $\widetilde{\vec{\omega}}$ by filtering:

$$ \vec{\omega}(\vec{r}, t) = \iiint G(\vec{r} - \vec{r}') \, \widetilde{\vec{\omega}}(\vec{r}', t) \, d\vec{r}' \ . \qquad (2.7) $$

The unfiltered vorticity $\widetilde{\vec{\omega}}$ is generated by the space curve $\vec{r}_i(\xi, t)$ as follows,

$$ \widetilde{\vec{\omega}}(\vec{r}, t) = \sum_i \Gamma_i \int \delta(\vec{r} - \vec{r}_i(\xi, t)) \, \frac{\partial \vec{r}_i}{\partial \xi} \, d\xi \qquad (2.8) $$

and is highly singular. Here ξ is a parameter which traces each filament along its length at any instant in time. The summation is over individual vortex filaments. The evolution of each space curve

is determined from the continuous velocity field by

$$\frac{\partial \vec{r_i}(\xi,t)}{\partial t} = \iiint G(\vec{r_i}-\vec{r}') \; \vec{u}(r',t) \; d\vec{r}' \qquad (2.9)$$
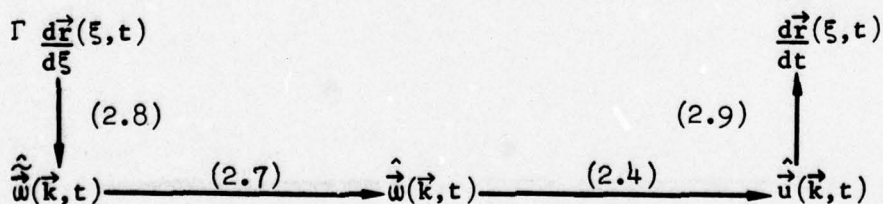
with $\vec{u}$ determined from (2.4).

In summary, equations (2.7), (2.8), (2.9) and (2.4) describe the physics of vortical flow which must be discretized for solution on the computer.

9

Chapter III

DESCRIPTION OF COMPUTATIONAL METHOD

For a variety of reasons, the vorticity field and other fields
are conveniently expressed in Fourier space, just as in the more
successful numerical attacks on the turbulence problem by solution of
the Navier-Stokes equation[30-33]. The main reason the fields compo-
nents are recorded in spectral form is that calculus (differentiation
and integration) translates to algebra (multiplication and division)
in the spectral domain. Of course, this implies periodicity in all
three dimensions.

Working in Fourier space also provides additional benefit from
the control one obtains over the filtering operation: the convolution
integral in (2.5) becomes a product in Fourier space. Translating
in Fourier space the basic principles given in the previous chapter,
we can draw a computational chain of operations. Starting with a
given set of vortex lines with their circulation Γ , we want to find
their displacement:

$$\Gamma \ \frac{d\vec{r}}{d\xi}(\xi,t) \qquad\qquad\qquad\qquad \frac{d\vec{r}}{dt}(\xi,t)$$

$$\Big\downarrow (2.8) \qquad\qquad\qquad\qquad (2.9) \Big\uparrow$$

$$\hat{\vec{\tilde{\omega}}}(\vec{k},t) \xrightarrow{\quad (2.7) \quad} \hat{\vec{\omega}}(\vec{k},t) \xrightarrow{\quad (2.4) \quad} \hat{\vec{u}}(\vec{k},t)$$

The numbers refer to the equations of the previous chapter. The
different parts of the scheme will now be explained, namely the
numerical modeling of the vortex filaments, the interpolations that
take place in order to use the fast Fourier transform, the shaping
of the vortices and the time-stepping procedure.

III.1 Filament Modeling

In our model, one describes each vortex filament by a succession of closely spaced markers. Considering a single vortex in (2.8), we have

$$\widetilde{\vec{w}}(\vec{r}) = \Gamma \oint \delta(\vec{r} - \vec{r}(\xi)) \frac{\partial \vec{r}}{\partial \xi} d\xi$$

at an instant t, where Γ is given by (2.6). Taking the Fourier transform, we get

$$\hat{\vec{w}}(\vec{k}) = \iiint e^{-i\vec{k}\cdot\vec{r}} \Gamma \oint \delta(\vec{r} - \vec{r}(\xi)) \frac{\partial \vec{r}}{\partial \xi} d\xi \, d\vec{r} \qquad (3.1)$$

If we now discretize $\vec{r}$ into piece-wise linear sections,

$$\vec{r}(\xi)_{j,j-1} = \xi\vec{r}_j + (1-\xi)\vec{r}_{j-1} , \qquad 0 \leq \xi \leq 1 ,$$

then

$$\hat{\vec{w}}(\vec{k}) = \sum_{j=1}^{m} \Gamma \int_0^1 (\vec{r}_j - \vec{r}_{j-1}) e^{-i\vec{k}\cdot\vec{r}(\xi)_{j,j-1}} d\xi \qquad (3.2)$$

where m is the total number of markers describing the filament and $\vec{r}_m = \vec{r}_o$. Integrating (3.2) and letting

$$\vec{k} \cdot \frac{(\vec{r}_j - \vec{r}_{j-1})}{2} = \epsilon_j ,$$

we obtain

$$\hat{\vec{w}}(\vec{k}) = \Gamma \sum_{j=1}^{m} \frac{i(\vec{r}_j - \vec{r}_{j-1})}{2\epsilon_j} \left(e^{-i\vec{k}\cdot\vec{r}_j} - e^{-i\vec{k}\cdot\vec{r}_{j-1}} \right)$$

$$= \Gamma \sum_{j=1}^{m} \frac{i(\vec{r}_j - \vec{r}_{j-1})}{2\epsilon_j} e^{-i\vec{k}\cdot\frac{1}{2}(\vec{r}_j + \vec{r}_{j-1})} \left(e^{-i\epsilon_j} - e^{i\epsilon_j} \right)$$

11

$$= \Gamma \sum_{j=1}^{m} (\vec{r}_j - \vec{r}_{j-1})\, e^{-i\vec{k}\cdot\frac{1}{2}(\vec{r}_j + \vec{r}_{j-1})}\, \frac{\sin \epsilon_j}{\epsilon_j} \quad (3.3)$$

The labor of evaluating the trigonometric functions for all sections of the filament in (3.3) to obtain one Fourier component $\hat{\tilde{w}}(\vec{k})$ would be prohibitive if each vortex required at each time step the evaluation of all the Fourier harmonics $\vec{k}$. All this might turn out to be as expensive as the primitive process of summing up all direct interactions among the vortices[34]. It is more efficient to first distribute vorticity onto the grid according to an interpolation process and then perform an FFT. Considering equation (3.3), it amounts to two things. First, we should be able to express $\sin \epsilon_j / \epsilon_j$ as a linear combination of $e^{-i\vec{k}\cdot\vec{f}}$ where $\vec{f}$ is a function of $\vec{r}_j$ and $\vec{r}_{j-1}$. Secondly, the resulting trigonometric exponential functions should be approximated onto the mesh in Fourier space so that the FFT can be performed. As of the substitution of $\sin \epsilon_j / \epsilon_j$, we went back to Eq. (3.2) and evaluated it by gaussian quadrature[35] to obtain,

$$\hat{\tilde{w}}(\vec{k}) = \Gamma \sum_{j=1}^{m} \frac{(\vec{r}_j - \vec{r}_{j-1})}{2}$$

$$\times \left\{ e^{-i\vec{k}\cdot\frac{1}{2}\left[(1+3^{-\frac{1}{2}})\vec{r}_j + (1-3^{-\frac{1}{2}})\vec{r}_{j-1}\right]} + e^{-i\vec{k}\cdot\frac{1}{2}\left[(1-3^{-\frac{1}{2}})\vec{r}_j + (1+3^{-\frac{1}{2}})\vec{r}_{j-1}\right]} \right\}$$

Indeed this is equivalent to the approximation,

$$\frac{\sin \epsilon_j}{\epsilon_j} \simeq \frac{e^{-i\epsilon_j 3^{-\frac{1}{2}}} + e^{i\epsilon_j 3^{-\frac{1}{2}}}}{2} = \cos\left(\frac{\epsilon_j}{3^{\frac{1}{2}}}\right)$$

(See Appendix I for derivation.)

12

What we want now is to replace the pure harmonic $e^{i\vec{k}\cdot\vec{r}}$ for arbitrary $\vec{r}$ by an approximant to be evaluated on the discrete spatial mesh.

III.2 Interpolation

In each of the three dimensions, we use quadratic spline interpolation to approximate e^{ikx} in terms of e^{ikn}. In particular, e^{ikx} is represented in the general interval $n - \frac{1}{2} \leq x \leq n + \frac{1}{2}$ as the superposition of three parabolic arcs as follows:

$$e^{ikx} \rightarrow \frac{1}{2} g_{n+1} (x-n+\frac{1}{2})^2 + g_n (\frac{3}{4} - (x-n)^2)$$

$$+ \frac{1}{2} g_{n-1} (n+\frac{1}{2}-x)^2 \tag{3.4}$$

This representation ensures continuity of function and slope between adjacent intervals. The spline coefficients g_n are usually chosen sc as to force agreement between function and approximant at the centers of the range in which each quadratic polynomial is used. In our case, we shall inject, at this point, only the information that the spline coefficients g_n must share the phase shifts, e^{ik}, per interval, with the function to be interpolated. Thus we take $g_n = S(k) e^{ikn}$ where $S(k)$ is independent of n. (3.4) then becomes:

$$e^{ikx} \rightarrow S(k)\left[\frac{1}{2} (x-n+\frac{1}{2})^2 e^{ik(n+1)} + \left(\frac{3}{4} - (x-n)^2\right)e^{ikn}\right.$$

$$\left. + \frac{1}{2} (n+\frac{1}{2}-x)^2 e^{ik(n-1)}\right] \tag{3.5}$$

or

$$e^{ikx} \rightarrow S(k)\left[1 - \frac{(1+4x^2)}{2} \sin^2 \frac{k}{2} + ix \sin k\right]$$

13

Note that the choice $4/(3+\cos k)$ for $S(k)$ would force agreement between function and approximant at $x = 0$.

We observe that the representative substitution for a general interval (3.5) means one pretabulates the spline coefficients

$$\sum_k S(k)\, f(k)\, e^{ikn}$$, not functions values, and one applies the spline

weights to the entries in this table for evaluation of local function values. The indicated summation over k is, of course, done as a fast Fourier transform. But one does not transform the original spectrum $f(k)$, one transforms $S(k)$ times the spectrum.

The adjustment factors $S(k)$ must still be specified. As mentioned, in conventional interpolation, one pins the interpolant to the function at specified points: the mid-points in each interval for quadratic interpolation. This is appropriate when one has no more information on a function than the values at integer abscissae. In our case, we have more information available.

Since we know the function to be approximated throughout the interval in principle from its Fourier harmonics, we can make a less biased choice of $S(k)$. We can minimize the mean square error over the interval by choice of $S(k)$. Using standard procedures, one finds that $S(k)\, P(x)$ deviates from e^{ikx} with the least mean square error when

$$S(k) = \int_{-\frac{1}{2}}^{\frac{1}{2}} P(x)\, e^{-ikx}\, dx \Big/ \int_{-\frac{1}{2}}^{\frac{1}{2}} P^2(x)\, dx \qquad (3.6)$$

and the mean square error is then

$$1 - \left(\int_{-\frac{1}{2}}^{\frac{1}{2}} P(x)\, e^{-ikx}\, dx \right)^2 \Big/ \int_{-\frac{1}{2}}^{\frac{1}{2}} P^2(x)\, dx$$

14

Here $P(x)$ is the polynomial in brackets in (3.5). With our new choice of $S(k)$, we can define the second order spline as that second order polynomial which joins smoothly (up to the first derivative continuous) with the corresponding polynomial in the adjacent intervals and which departs from the given function with least mean square error.

The numerator in (3.6) is recognized to be the Fourier transform of the second order spline when the trignometric functions in P are expressed in terms of complex exponentials. The second order spline is known to be the second convolution of the rectangle function with itself. The rectangle function $(= 1$ for $|x| < \frac{1}{2}$, $= 0$ for $|x| > \frac{1}{2})$ transforms to $\frac{2}{k} \sin \frac{k}{2}$[36]. Thus the numerator in the expression (3.6) for $S(k)$ is $\left(\frac{2}{k} \sin \frac{k}{2}\right)^3$. As for the denominator D in (3.6) one finds:

$$D = \frac{16 + 13 \cos k + \cos^2 k}{30}$$

$$= 1 - \sin^2 \frac{k}{2} + \frac{2}{15} \sin^4 \frac{k}{2}$$

The formula for the mean square error now becomes

$$1 - \left(\frac{2}{k} \sin \frac{k}{2}\right)^6 \bigg/ D$$

The square root of the mean square error is plotted versus k in Figure 1. One finds that for small k, the rms error is of order k^3, specifically the rms error is
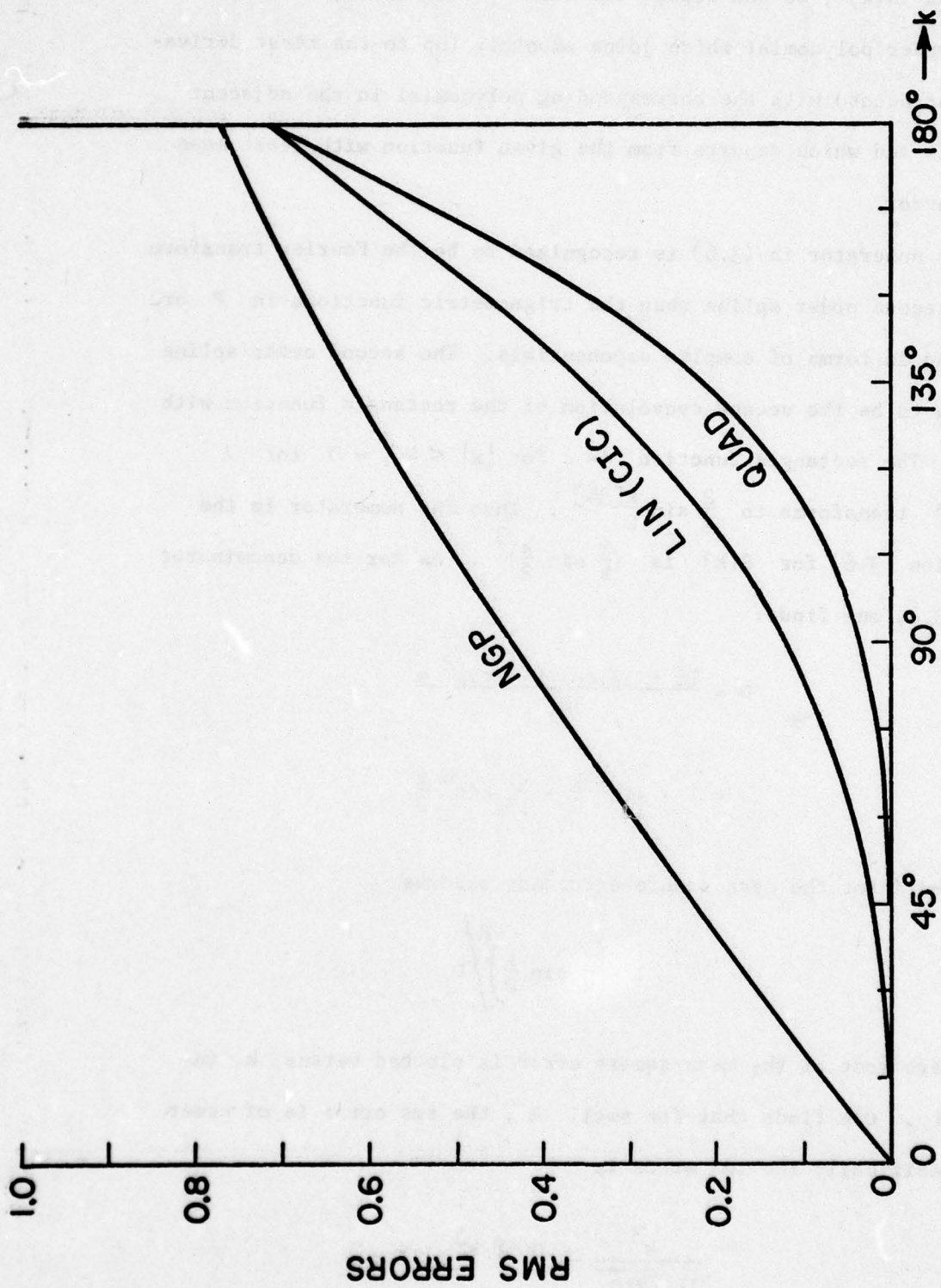
$$\frac{k^3}{12\sqrt{210}} \simeq .0058 \, k^3$$

15

Figure 1. Square root of the mean square error k for nearest grid point, linear and quadratic interpolation of a pure harmonic.

As mentioned in the previous section, the purpose of interpolation is, in fact, to distribute vorticity onto a grid. Figure 2 illustrates a one-dimensional model where three quadratic spline distributions of vorticity with different total amplitudes are shown to have their centers located at positions a, b, and c. It also shows that three nearest grid points to each of the centers will share the vorticity distribution according to the spline function weighting on them. In other words, this is a particular way to distribute a finite-sized vorticity on its neighboring grid points. In our example, grid points N-2 to N will share the vorticity at "a" with N-1 getting most weighting. Similarly points N-1 to N+2 will share the vorticities "b" and "c". It is the array of this vorticity distribution that will be transformed to calculate the potential array and velocity field array. The quadratic spline weighting is superior to the zero-order weighting (NGP model) and first-order weighting (CIC model) in the sense of creating less field-noise and resulting in smoother simulation functions[37,38]. This is an obvious conclusion since vorticity is now distributed among three grid points instead of one or two as in the other models and the interpolated distribution is quadratic rather than a piece-wise step function, or first-order linear function, with discontinuous derivatives. There is also a reduction of aliassing. In three dimensions, the three nearest grid points in each dimension (27 in all) will share the vorticity distribution according to the spline function weighting on them.

The sensitivity to grids being introduced for interpolation purposes was tested by Buneman[37,38,39] and Wang[17]. Buneman[37] showed that substantial distortion of the local stream function can result
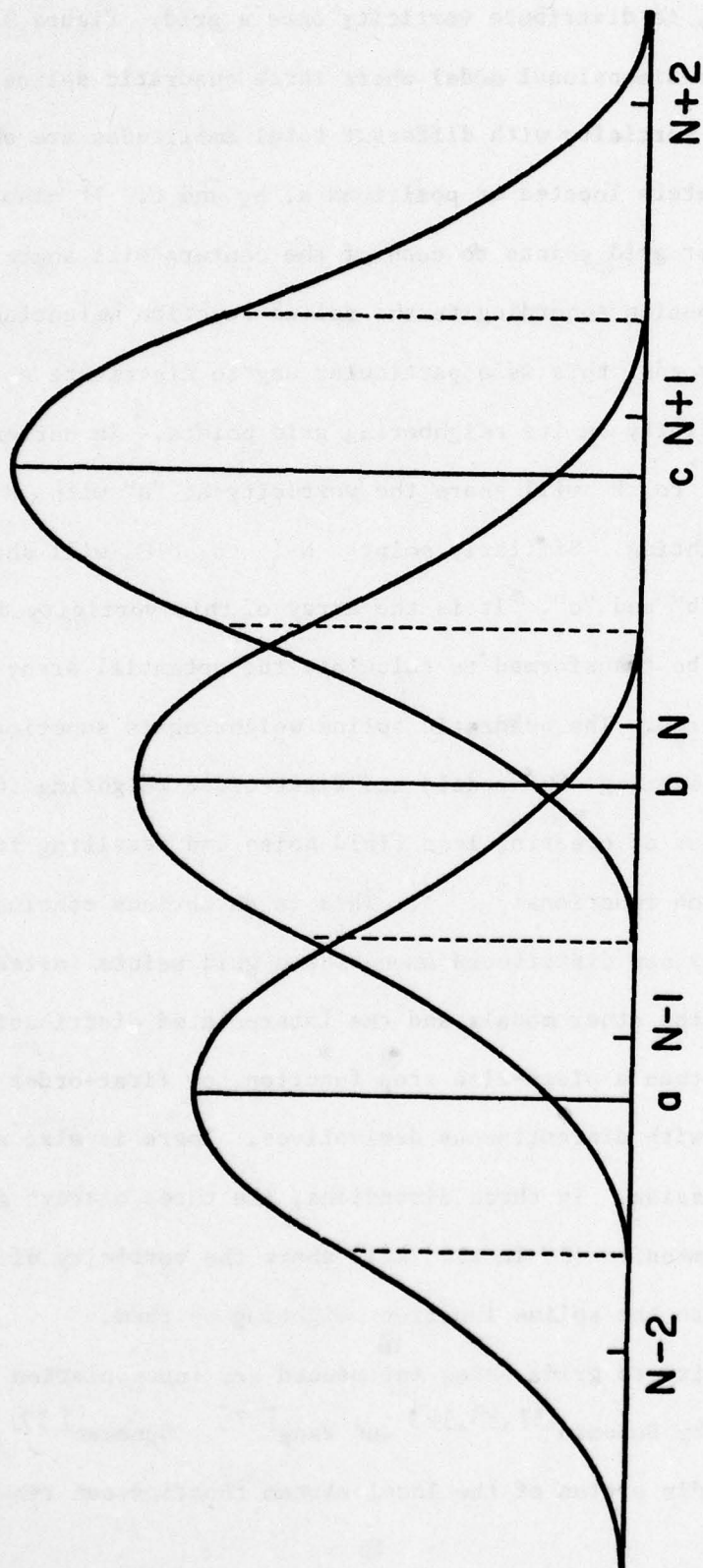
17

Figure 2 . Quadratic spline vorticity distribution of three typical particles on their nearby grid points.

from linear interpolation if the vortex is located at other than the symmetric positions in the grid. By using least-mean-square fitted quadratic splines, it was shown that the stream function is virtually insensitive to the grids such that the same undistorted stream function will appear no matter where the vortex is located. Figure 3 illustrates that at four different subgrid positions, the first for the vortex center directly on a grid point, the last for the vortex center in the middle of the cell and the two cases in between for typical unsymmetrical vortex positions: the stream lines of the vortex are perfectly circular and unaffected by the existence of the grid points.

III.3 Shape Factor, Subgrid "Viscosity"

It is intuitively obvious that low-$|\vec{k}|$ harmonics are interpolated by a certain tabulation mesh better than high-$|\vec{k}|$ harmonics. Aliassing sets a limit at $k_{max} = \pi/\Delta$ for each component of $\vec{k}$ ($\Delta \equiv$ mesh spacing): any harmonic with a k-component higher than this will be misinterpreted by the interpolator as a corresponding lower harmonic with all k-components lying within the interval $(-\pi/\Delta, \pi/\Delta)$. In effect, the interpolator will add a mixture of overtones to the approximation of a pure harmonic. A reduction of aliassing was already achieved by going to a higher order interpolation than linear. Another way to suppress aliasses is to de-emphasize harmonics in the range near k_{max}.

The effects of a finite cut-off of the spectrum on the physics to be computed is an important question separate from the question of interpolation. Two aspects of the cut-off problem are worth emphasizing.
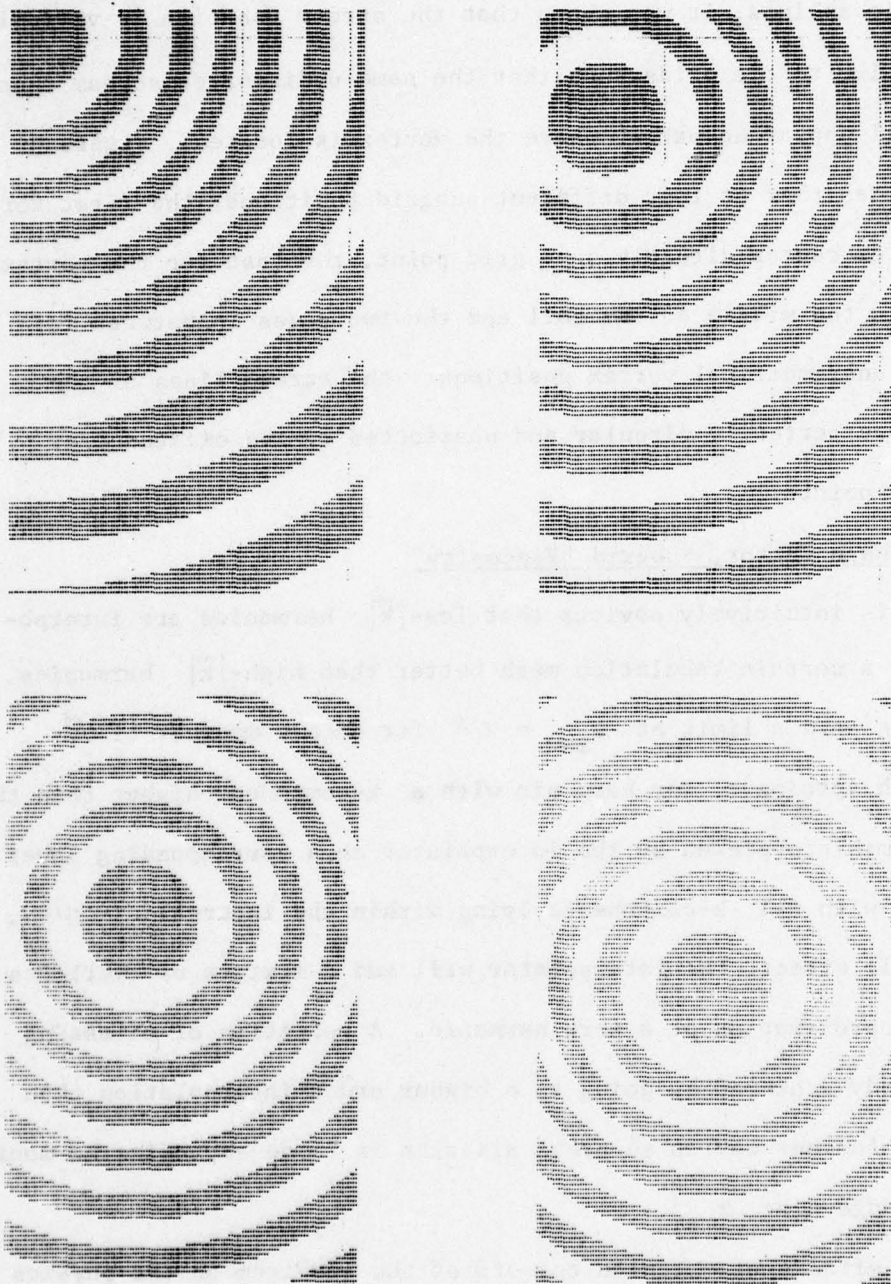
Figure 3 . Stream function contours of a single vortex at different subgrid positions.

Firstly, a sharp cut-off in Fourier space is undesirable (no matter how perfectly each harmonic is evaluated) because it surrounds the objects that interact via the field with halos in real space. The halos decay only weakly with distance, like Δ/r . If, instead, the spectrum is brought to zero more smoothly, say at least parabolically, such halos become attenuated more strongly. A bell-shaped cut-off factor, say $\hat{G}^2(|\vec{k}|)$, suggests itself. Consequently, even if the object of interpolation studies is to push up the maximum usable $|\vec{k}|$, it should concentrate on performance in the range of low and intermediate $|\vec{k}|$; $|\vec{k}|$-values near k_{max} become irrelevant. It is important to distinguish between the factor $\hat{G}^2(|\vec{k}|)$ introduced into the spectrum by such shaping and the compensating adjustment factors $S^2(k)$ which improves interpolation performance. The square is quoted here because both the vorticity deposition and the local effects of the velocity field call for interpolations.

Secondly, any cut-off factor $\hat{G}^2(|\vec{k}|)$ implies a shape for the interacting vortices which is the Fourier transform of $\hat{G}(|\vec{k}|)$. The dual appearance of the shape factors is emphasized by the fact that the interpolation errors, likewise, appear twice, as mentioned above. So the shape enters the field interaction process twice, namely both when the velocity field harmonics are excited by the local sources (vortices) and when the velocity field harmonics react back on them. Therefore, any such factor in the spectral domain (introduced primarily for the purpose of fitting the field harmonics into a finite computer) can be interpreted physically as vorticity-spreading.

There are good reasons for introducing shapes of the interacting elements even when no interpolation is used at all and spectral data

21

are evaluated precisely, without grids and tabulations. When a problem is solved entirely in the spectral domain, non-linear terms, i.e. products of transformed variables, manifest themselves as convolutions[33]. Here the cascading into higher harmonics (for which there is no room in the computer) has to be suppressed artificially by some cut-off or shape-factor. Secondly, the interacting "fluid elements" in the real world are usually much more numerous than those that can be accomodated in a computer with its peripheral storage. Each element in the computer stands in for a swarm of real elements. It should therefore be given a spread.

In our simulation so far, we use a cubical mesh system, that is $\Delta x = \Delta y = \Delta z = 1$. Therefore, we note that the shape factor $G(\vec{r})$ should be isotropic in space: it knows no coordinate axes. Hence $\hat{G}(|\vec{k}|)$ is isotropic in $\vec{k}$-space, being a function only of $|\vec{k}|$. The compensating adjustment factors $S^2(k)$, on the contrary, must be functions of the components of $\vec{k}$. Since one has an a priori freedom of choice as regards $G(\vec{r})$ or $\hat{G}(|\vec{k}|)$, one is at liberty to tailor $G(\vec{r})$ so that it de-emphasizes the poorly interpolated (badly aliassed) harmonics near $|\vec{k}| = \pi$. Nevertheless a gaussian profile $G(\vec{r})$ seems to be more readily accepted as realistic: for a viscous vortex ring with small cross-section, Tung and Ting[40] and Saffman[41] found that the distribution of vorticity across the core is gaussian. It has also the advantage of being well confined both in real and Fourier space. However, with a finite band-width available for $\hat{G}(|\vec{k}|)$, one can only approach a gaussian profile since the finite k-range always causes some small residual halos. A fair compromise is achieved by taking a cubic spline profile, tending to zero cubically as k_{max}

is approached:

$$1 - \frac{6}{\pi^2} |\vec{k}|^2\left(1 - \frac{|\vec{k}|}{\pi}\right) \qquad \text{for} \quad |\vec{k}| \le \frac{\pi}{2} ,$$

$$2\left(1 - \frac{|\vec{k}|}{\pi}\right)^3 \qquad \text{for} \quad \frac{\pi}{2} \le |\vec{k}| \le \pi$$

This choice is quite unrelated to the use of splines for interpolation. The cubic spline profile was used for the quantity $\hat{G}^2(|\vec{k}|)$, not for $\hat{G}(|k|)$. The transform into real space is $\left(\frac{4}{\pi|\vec{r}|} \sin \frac{\pi|\vec{r}|}{4}\right)^4$. This is positive everywhere and has very small sidebands (or aliasses): the first satellite is two thousandth of the center peak. Both this $\hat{G}^2(|\vec{k}|)$ and the corresponding profile in real space look very much like gaussians. In fact, by using the Central Limit theorem[36], one sees that

$$\hat{G}^2(|\vec{k}|) \approx \exp\left(- \frac{6 |\vec{k}|^2}{\pi^2}\right),$$

Figure 4, which implies

$$\hat{G}(|\vec{k}|) \approx \exp\left(- \frac{3 |\vec{k}|^2}{\pi^2}\right) \tag{3.7}$$

By transforming back into real space, we get

$$G(\vec{r}) \cong \exp\left(- \frac{\pi^2|\vec{r}|^2}{12}\right) \tag{3.8}$$

A spread-out vortex with gaussian profile is the result of viscosity having acted, for a time proportional to the effective area of spread[41], on an initially ideal filamentary vortex. However, the area of the spread, i.e. the "age" of the vortices, is fixed as shown by (3.8). Therefore, all vortices represented in this manner have the same "middle-aged" spread!
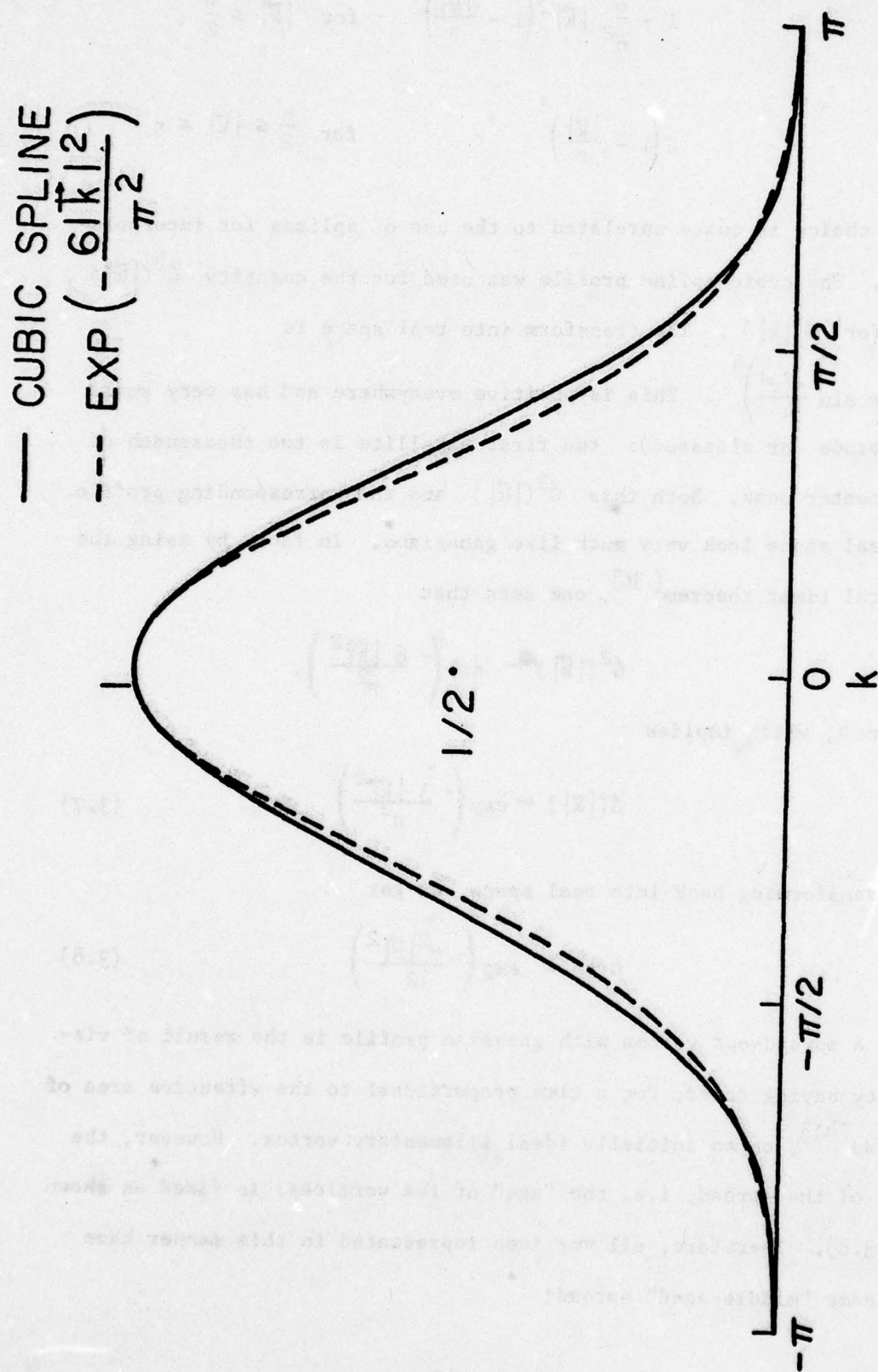
23

Figure 4. Cubic spline function with its gaussian approximation.

To summarize the interpolation and shaping operations, we start
with a vorticity field having singularities on each filament, Eq.
(2.8). The use of a grid with spacing Δ and Fourier transform
methods eliminates the singularities since only harmonic numbers up
to π/Δ are recognized and the vortices are thus automatically
broadened by what is approximately equivalent to a rectangular filter
in Fourier space. In addition, further shaping of the vorticity dis-
tribution is achieved by explicit application of another filter whose
representation in Fourier space is $\hat{G}(\vec{k})$. The effective vorticity
field $\vec{\omega}$ is then represented by a filtering operation on singular
$\tilde{\vec{\omega}}$ as shown by (2.7) where G now indicates the transverse profile
of the vortex filaments. We choose $\hat{G}(\vec{k})$ to be almost gaussian
(bell-shaped, coming to zero smoothly before the spectrum would cut
off more drastically), (Figure 4) and then each filament acquires a
transverse profile in real space that is nearly gaussian. The shape
factor G is applied again when one calculates the evolution of each
space curve in time from the continuous velocity field $\vec{u}(\vec{r},t)$, Eq.
(2.9) with $\vec{u}$ determined from (2.4). In practice, this means apply-
ing the square of the transform of G as a filter in Fourier space.
The use of the filter $\hat{G}$ provides damping of the high wavenumber
components of the field, damping that would otherwise occur through
subgrid scale dissipation or by viscous dissipation[28].

III.4 Solving

The advance of vortices from one time step to the next in our
code requires the handling of (6 field components * 32^3 mesh points =)
196608 field components and about 32000 "vortex-markers". If we now
consider Eq. (2.4) in Fourier space, the velocity field at the loca-
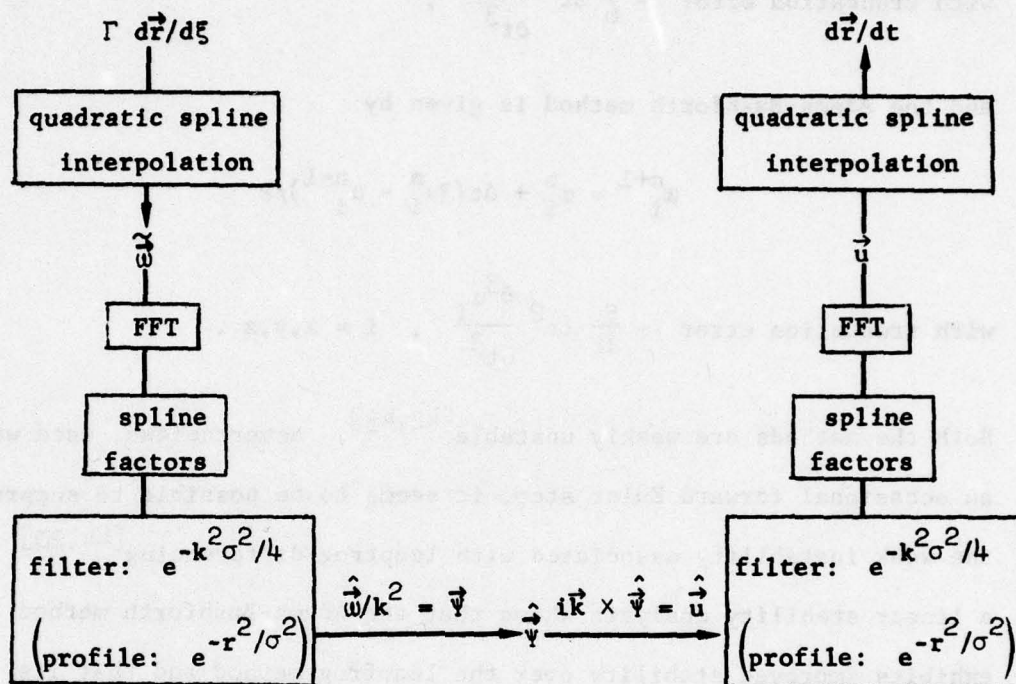tion of a "vortex-marker" is obtained by weighting the entries in the

25

table of spline amplitudes with the spline weights. The latter are deduced from the relative position of a vortex in its interpolation cell. The spline amplitudes are obtained from the velocity harmonics by first multiplying with a factor $S(k_x)$ and two similar factors which have k_y and k_z in place of k_x, then calling a three-dimensional FFT on the resulting array.

The same factors appear again when the displacement of the kth vorticity harmonic is calculated. The interpolation can be done for the sum of all the harmonics, and the table into which one interpolates are then the FFT's of the harmonics of vorticity, modified by the factors insuring best mean square fit in each dimension.

In going from the table of spline amplitudes for vorticity to the table of spline amplitudes for velocity harmonics, one therefore has not only to perform a forward and backward FFT, with Eq. (2.4) in Fourier space in between, but one must also introduce the squares of the spline fitting factors indicated above.

Similarly, we mentioned that any vorticity shaping factor should be introduced both when the local velocity field action on the distributed vorticity cloud is evaluated and when its excitation of the vorticity harmonics is accumulated. In both cases, one could perform a convolution in real space, but it is much quicker to replace this by a multiplication in Fourier space. The transform of the shape factor is therefore introduced squared along with the above mentioned spline fitting factors in the course of solving the equations for the velocity field in Fourier space. It is convenient to introduce the (squared) shape factor along with the inverse Poisson operator $1/|\vec{k}|^2$. In our 32^3 code, there are only 256 possible different values of $|\vec{k}|^2$ in the sphere $|\vec{k}| \le k_{max}$ (64 values for a 16^3 code),

26

so any function of $|\vec{k}|$ can readily be pretabulated. The schematic description given below summarizes the algorithm.

$$\Gamma \; d\vec{r}/d\xi \qquad\qquad\qquad\qquad\qquad\qquad\qquad d\vec{r}/dt$$

<div align="center">

quadratic spline interpolation

$\tilde{\vec{\omega}}$

FFT

spline factors

filter: $e^{-k^2\sigma^2/4}$ (profile: e^{-r^2/σ^2})

</div>

<div align="center">

quadratic spline interpolation

$\vec{u}$

FFT

spline factors

filter: $e^{-k^2\sigma^2/4}$ (profile: e^{-r^2/σ^2})

</div>

$$\hat{\tilde{\vec{w}}}/k^2 = \hat{\vec{\psi}} \qquad i\vec{k} \times \hat{\vec{\psi}} = \hat{\tilde{\vec{u}}}$$

III.5 Time Advancing

The choice of a time differencing method is dictated by the trade-off between the increased cost per step (in computation time and/or storage) of high-accuracy methods and the large time step allowed by such methods. When the choice is made on this basis, we are interested in knowing only that the method is stable for the time step chosen. There is no reason to choose a method with extra stability if the cost is higher. Two commonly used methods, which are second-order accurate and require only one function evaluation per time step, are the leapfrog and the Adams-Bashforth methods. Both are multi-step explicit methods and require storage for two time steps. The leapfrog method is given by

$$\omega_i^{n+1} = \omega_i^{n-1} + 2\Delta t \, u_i^n$$

with truncation error $-\dfrac{1}{6} \Delta t^2 \dfrac{\partial^3 u_i}{\partial t^3}$,

and the Adams-Bashforth method is given by

$$\omega_i^{n+1} = \omega_i^n + \Delta t (3u_i^n - u_i^{n-1})/2$$

with truncation error $-\dfrac{5}{12} \Delta t^2 \dfrac{\partial^3 u_i}{\partial t^3}$, $i = x, y, z$.

Both the methods are weakly unstable[42,43]. Nevertheless, used with an occasional forward Euler step, it seems to be possible to suppress the weak instability associated with leapfrog differencing[44,20]. Also, a linear stability analysis shows that the Adams-Bashforth method exhibits improved stability over the leapfrog method and that its total spurious computational production of kinetic energy is small[44]. In this work, we started using the leapfrog method mainly to test our code on the rings experiments and then after used the Adams-Bashforth method. The first step in time differencing is generated by Euler's method:

$$\omega_i^1 = \omega_i^0 + \Delta t \, u_i^0$$

Chapter IV

RESULTS

The numerical solution of the scheme described in the previous chapters for different initial conditions were carried out on the CDC-7600 computer at NASA-Ames Research Center. The computing time per computational time step to move a vortex made of m markers was approximately as follows:

$$0.34 + m/5000 \text{ for a } 16^3 \text{ calculation,}$$
$$0.91 + m/1275 \text{ for a } 32^3 \text{ calculation.}$$

In our 32^3 algorithm, some programming refinements have been made; since the vorticity field and velocity field are purely real functions in real space, it is possible to use a complex Fourier transform of length 16 to get the vorticity transform of length 32 and similarly to transform back the velocity harmonics to obtain the velocity field in real space. (See Appendix II for derivation and[45].) This trick improves speed as well as it saves storage.

IV.1 Single Vortex Rings

A first experiment was done, with a 16^3 mesh, on a single vortex ring of radius R about the z-axis. Its center is initially located at $(8,8,8)$ in our mesh and thereafter moves along the z-axis. The circulation is $\Gamma = 2$. In particular, we investigated the initial speed of the vortex ring as a function of radius and position around the ring.

To check the accuracy of our mesh technique we also computed the speed of the vortex ring using a continuum or Green's function approach. Since the filter we use in the mesh method is approximately gaussian (Eq. 3.8), we consider a single vortex ring of gaussian cross-section.

29

On the one hand, if we consider equations (2.7) and (2.9) in Fourier space, they become respectively,

$$\hat{\vec{w}}(\vec{k},t) = \hat{G}(|\vec{k}|) \cdot \hat{\dot{\vec{w}}}(\vec{k},t) \qquad (4.1)$$

and

$$\frac{\partial \vec{r}_i}{\partial t}(\xi,t) = \left(\frac{1}{2\pi}\right)^3 \iiint e^{i\vec{k}\cdot\vec{r}_i} \hat{G}(|\vec{k}|) \cdot \hat{\vec{u}}(\vec{k},t) \, d\vec{k} \qquad (4.2)$$

On the other hand, equation (2.4) translates to

$$\hat{\vec{u}}(k,t) = \frac{i\vec{k} \times \hat{\vec{w}}(\vec{k},t)}{k^2} \qquad (4.3)$$

in Fourier space. Equation (3.1) together with (4.1) gives, for a single vortex filament of gaussian cross-section,

$$\hat{\vec{w}}(\vec{k},t) = \Gamma \hat{G}(|\vec{k}|) \oint e^{-i\vec{k}\cdot\vec{r}'} \frac{\partial \vec{r}'}{\partial \xi} \, d\xi$$

Using (4.2) and (4.3), we then get

$$\frac{\partial \vec{r}}{\partial t}(\xi,t) = \frac{\Gamma}{(2\pi)^3} \iiint \frac{\hat{G}^2(|\vec{k}|)}{k^2} \oint e^{-i\vec{k}\cdot(\vec{r}'-\vec{r})} \, i\vec{k} \times \frac{\partial \vec{r}'}{\partial \xi} \, d\xi \, d\vec{k} \qquad (4.4)$$

For the $\vec{k}$-space integration, we introduce spherical coordinates

$$\vec{k} = |\vec{k}| \sin(\theta)\cos(\varphi)\vec{e}_1 + |\vec{k}| \sin(\theta)\sin(\varphi)\vec{e}_2 + |\vec{k}| \cos(\theta)\vec{e}_3$$

(see Figure 5)

Figure 5. Vector $\vec{k}$ in
       spherical coordinates.

30
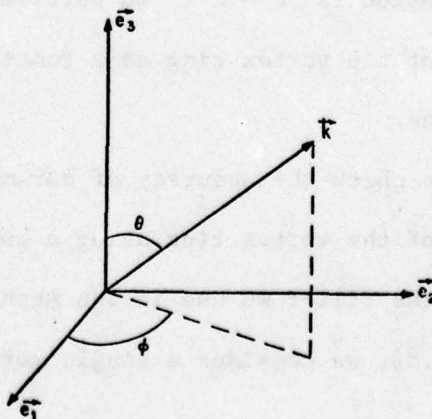
where we choose $\vec{e}_3 = \dfrac{\vec{r}'-\vec{r}}{|\vec{r}'-\vec{r}|}$.

This choice of $\vec{e}_3$ and the fact that $\vec{e}_1 \cdot \vec{e}_3 = \vec{e}_2 \cdot \vec{e}_3 = 0$ implies that $\vec{k} \cdot (\vec{r}'-\vec{r}) = |\vec{k}| \cos(\theta)|\vec{r}'-\vec{r}|$. After integrating with respect to φ , (4.4) becomes

$$\frac{\partial \vec{r}}{\partial t}(\xi,t)\frac{\Gamma}{(2\pi)^2}\int_0^\infty \frac{G^2(|\vec{k}|)\,|\vec{k}|\,i}{|\vec{r}'-\vec{r}|}\int_0^\pi e^{-i|\vec{k}|\cos(\theta)|\vec{r}'-\vec{r}|}\sin(\theta)\cos(\theta)$$

$$\oint (\vec{r}'-\vec{r})\times\frac{\partial\vec{r}'}{\partial\xi}\,d\xi\,d\,\theta\,d|\vec{k}|$$

Now, let $\zeta = \cos(\theta)$ which implies $d\zeta = -\sin(\theta)d\,\theta$,

$$\frac{\partial \vec{r}}{\partial t}(\xi,t) = \frac{\Gamma}{(2\pi)^2}\int_0^\infty \frac{G^2(|\vec{k}|)\,|\vec{k}|\,i}{|\vec{r}'-\vec{r}|}\int_{-1}^1 e^{-i|\vec{k}|\zeta|\vec{r}'-\vec{r}|}\zeta$$

$$\oint (\vec{r}'-\vec{r})\times\frac{\partial\vec{r}'}{\partial\xi}\,d\xi\,d\zeta\,d|\vec{k}|$$

But

$$\int_{-1}^1 e^{-i|\vec{k}|\zeta|\vec{r}'-\vec{r}|}\,\zeta\,d\zeta = 2i\left[\frac{\cos(|\vec{k}||\vec{r}'-\vec{r}|)}{|\vec{k}||\vec{r}'-\vec{r}|} - \frac{\sin(|\vec{k}||\vec{r}'-\vec{r}|)}{|\vec{k}|^2|\vec{r}'-\vec{r}|^2}\right]$$

So the integral over $|\vec{k}|$ becomes

$$-2\int_0^\infty \frac{G^2(|\vec{k}|)\cos(|\vec{k}||\vec{r}'-\vec{r}|)}{|\vec{r}'-\vec{r}|^2}\,d|\vec{k}| + 2\int_0^\infty \frac{G^2(|\vec{k}|)\sin(|\vec{k}||\vec{r}'-\vec{r}|)}{|\vec{r}'-\vec{r}|^3\,|\vec{k}|}\,d|\vec{k}|$$

Since $G(|\vec{k}|)$ is of the form $e^{-|\vec{k}|^2\sigma^2/4}$ (see Eq. (3.7)), where σ is the width of the gaussian filter, the sum of these two integrals is, following [35] and [46]:

$$- \frac{(2\pi)^{\frac{1}{2}} e^{-|\vec{r}'-\vec{r}|^2/2\,\sigma^2}}{\sigma|\vec{r}'-\vec{r}|^2} + \frac{\pi}{|\vec{r}'-\vec{r}|^3} \; \text{erf}\!\left(\frac{|\vec{r}'-\vec{r}|}{\sigma \, 2^{\frac{1}{2}}}\right)$$

We finally obtain for (4.4),

$$\frac{\partial \vec{r}}{\partial t}\,(\xi, t) = \frac{\Gamma}{4\pi} \oint \frac{F(|\vec{r}-\vec{r}'|/\sigma \, 2^{\frac{1}{2}})}{|\vec{r}-\vec{r}'|^3}(\vec{r}'-\vec{r}) \times \frac{\partial \vec{r}'}{\partial \xi}\, d\xi \qquad (4.5)$$

where

$$F(\zeta) = \text{erf}\,(\zeta) - 2\pi^{-\frac{1}{2}}\zeta \, e^{-\zeta^2} \qquad (4.6)$$

(4.5) gives the filtered velocity of translation in free space for a single vortex filament of gaussian cross-section. It should be mentioned that for $\sigma^2 \ll R^2$, (4.5) can be approximated to yield

$\frac{\partial \vec{r}}{\partial t} \approx \frac{\Gamma}{4\pi R}\left[\ln\!\left(\frac{8R}{\sigma}\right) - C\right]\vec{e}_z$ where $C = 1.058$ and $\vec{e}_z$ is the unit vector in the direction of translation z (see Appendix III for derivation). Note that the actual speed of a thin vortex ring with a gaussian distribution of vorticity has been calculated by Saffman[41] and is given by the above formula but with $C = 0.558$. The difference is due to the fact that Saffman's result is based on the collective motion of an infinite number of vortex tubes with internal interaction between the filaments whereas our result represents the speed of a single computational ring filament.

In Figures 6 and 7, we plot the velocities of translation measured at two positions around the ring versus different ring radii R. Remember that the vortex-in-cell (VIC) method used here implies periodic boundary conditions in each of the three dimensions. Therefore, velocities measured at, say $(R+8,8,8)$ and $(8+R/2^{\frac{1}{2}}, 8+R/2^{\frac{1}{2}}, 8)$ are not quite the same: see Figure 8. In order to explain the difference, we note that

32
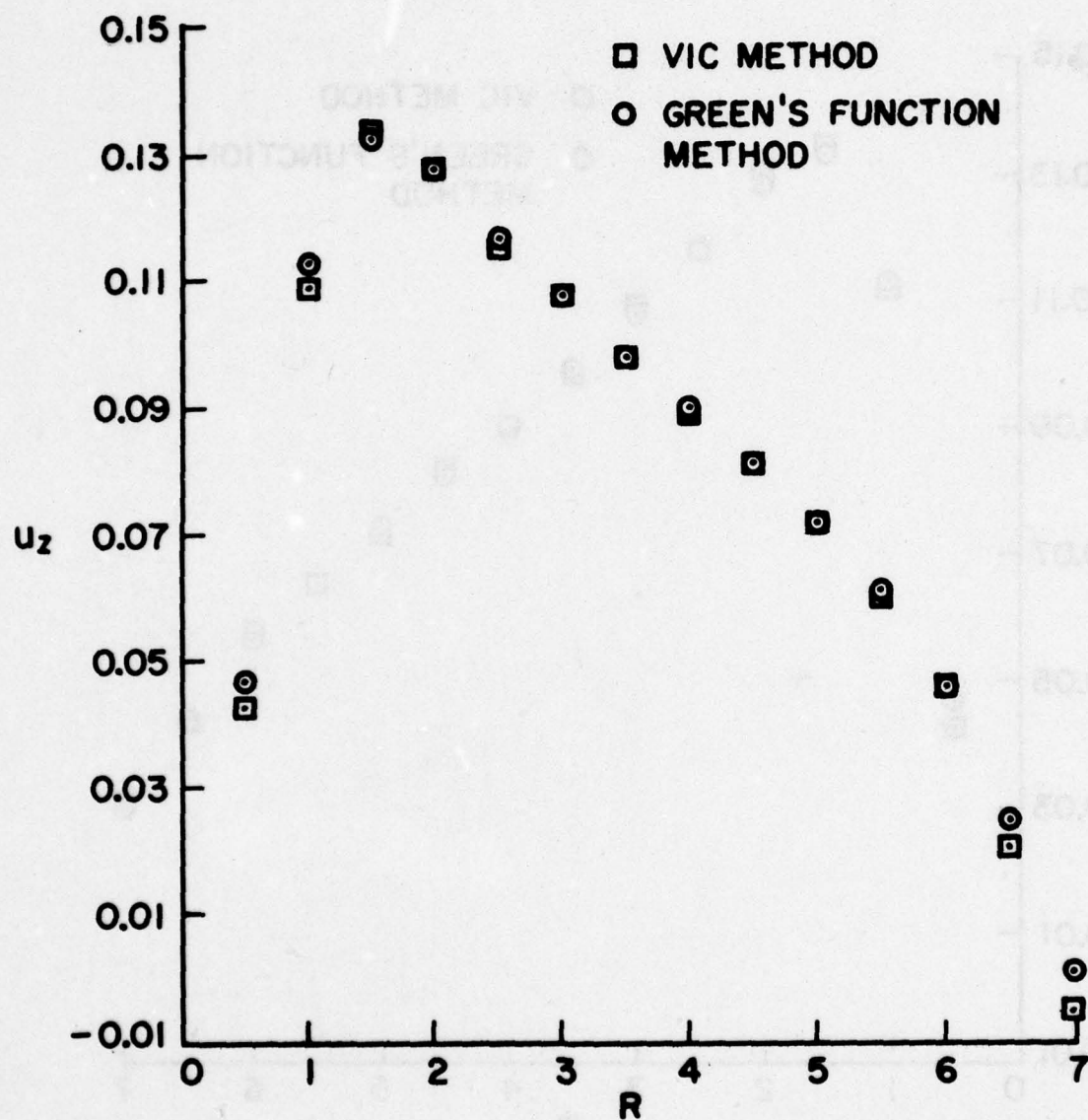
Figure 6. Velocity of translation (minimum) versus radius for a periodic array of single vortex rings.
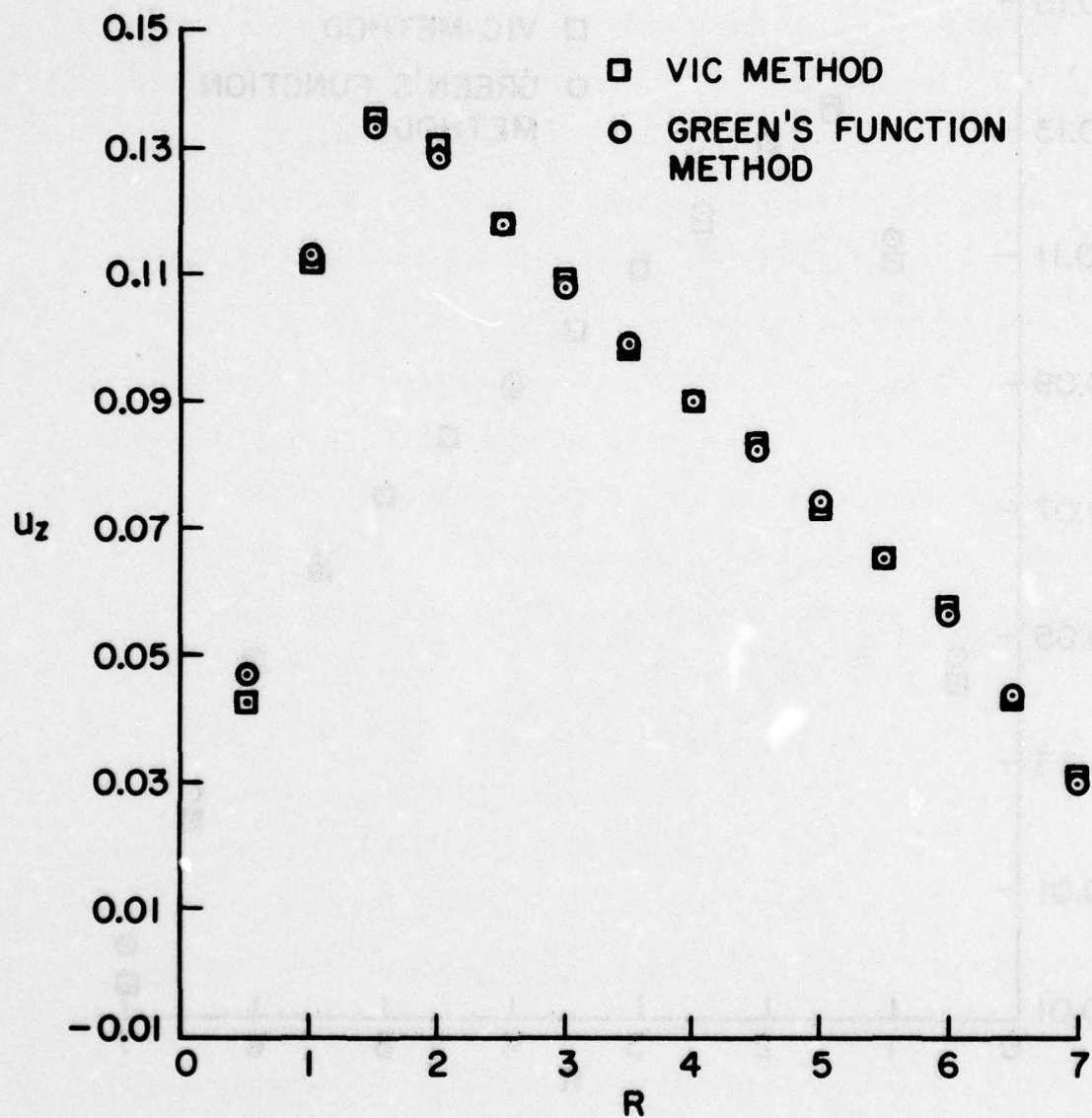
Figure 7. Velocity of translation (maximum) versus radius for a periodic array of single vortex rings.
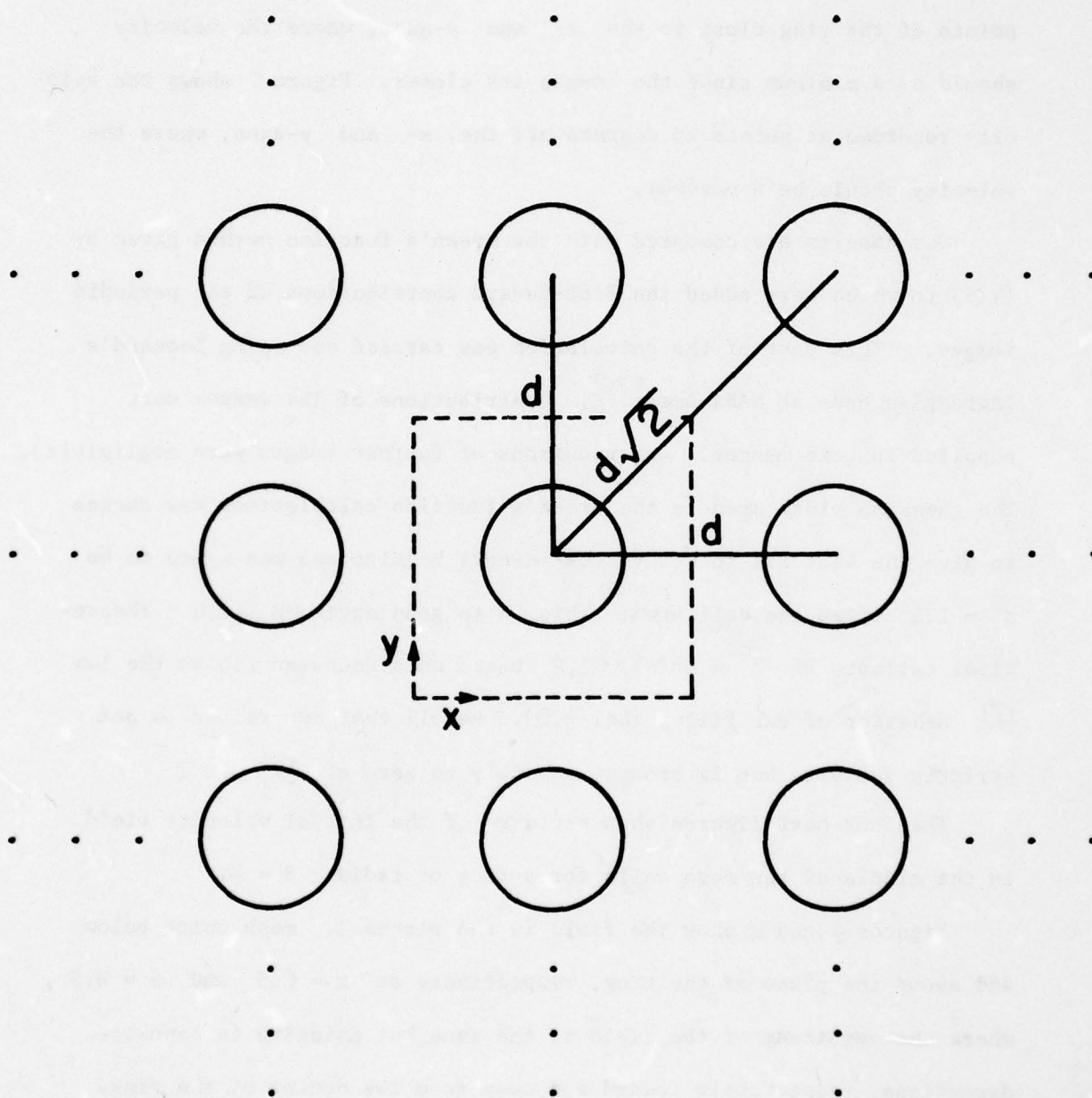
Figure 8. Periodic array of single vortex rings, all having the same circulation.

the Fourier transform creates images in a cartesian fashion as seen in a (x-y)-plane (Figure 8). The images oriented diagonally with respect to our computational ring are farther so they will not slow our ring down as much as the ones on the axes. Figure 6 shows the velocity recorded at points of the ring close to the x- and y-axes, where the velocity should be a minimum since the images are closer. Figure 7 shows the velocity recorded at points 45 degrees off the x- and y-axes, where the velocity should be a maximum.

Our results are compared with the Green's function method given by (4.5) to which were added the Biot-Savart contributions of the periodic images. (This part of the calculation was carried out using Leonard's lagrangian code at NASA-Ames[20]. Contributions of 124 images were supplied in this manner. Contributions of further images were negligible). The gaussian width used in the Green's function calculations was chosen to give the best fit to the vortex-in-cell results and was found to be $\sigma^2 = 1.1$ times the cell area. This is in good agreement with a theoretical estimate of $\sigma^2 = 12/\pi^2 \simeq 1.2$ based on a gaussian fit to the low $|\vec{k}|$ behavior of our filter (Eq. 3.8). Recall that our filter is not strictly gaussian but is brought smoothly to zero at $|\vec{k}| = \pi$.

The four next figures show pictures of the initial velocity field in the middle of the mesh cells for a ring of radius $R = 4$.

Figures 9 and 10 show the field in the planes 1.5 mesh units below and above the plane of the ring, respectively at $z = 6.5$ and $z = 9.5$, where the magnitude of the field is the same but pointing in opposite directions, respectively toward and away from the center of the ring. Figures 11 and 12 show the field in the planes $x = 6.5$ and $x = 9.5$. Figure 13 shows the lateral vortex profile in the (x-z)-plane at four
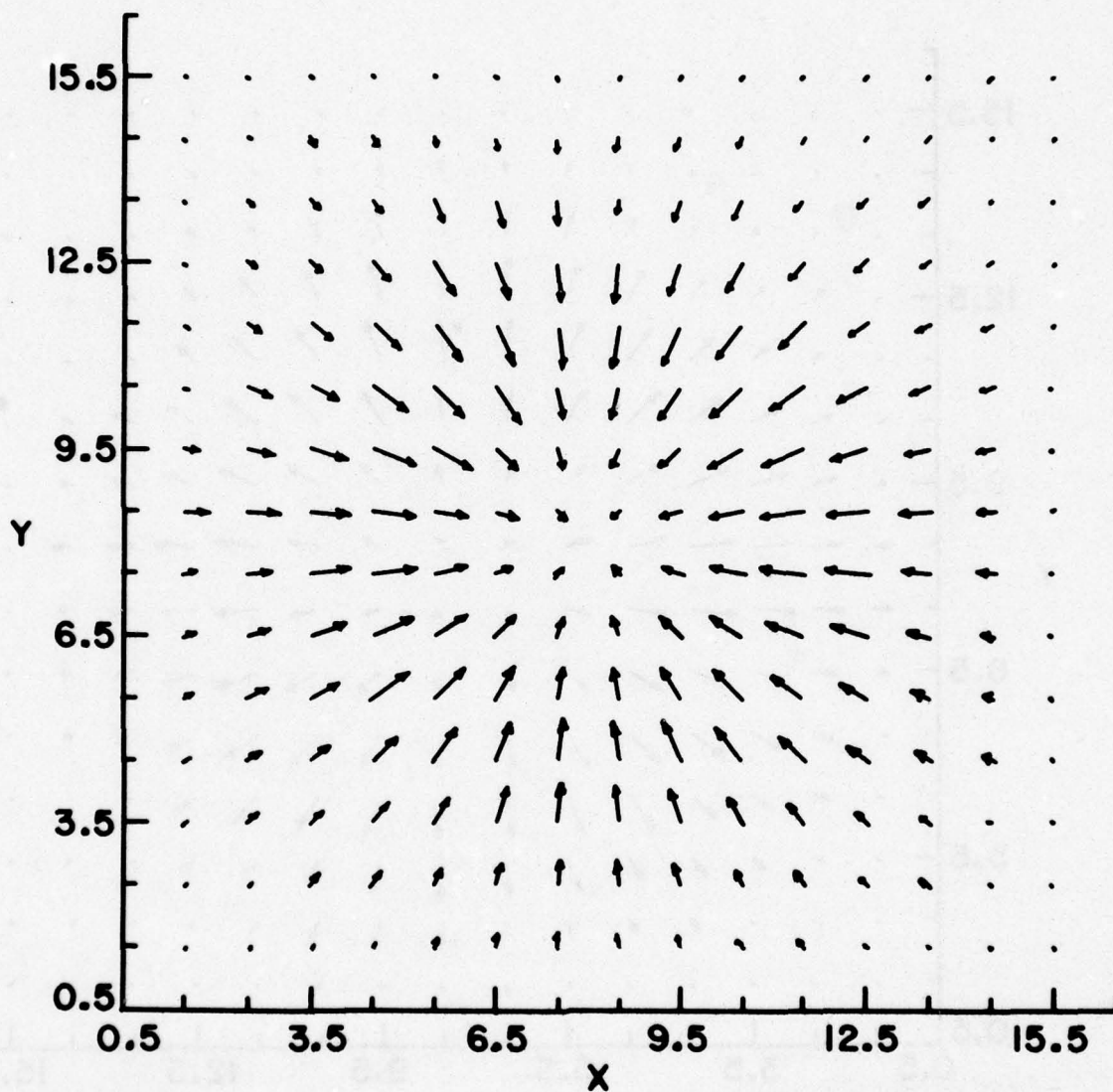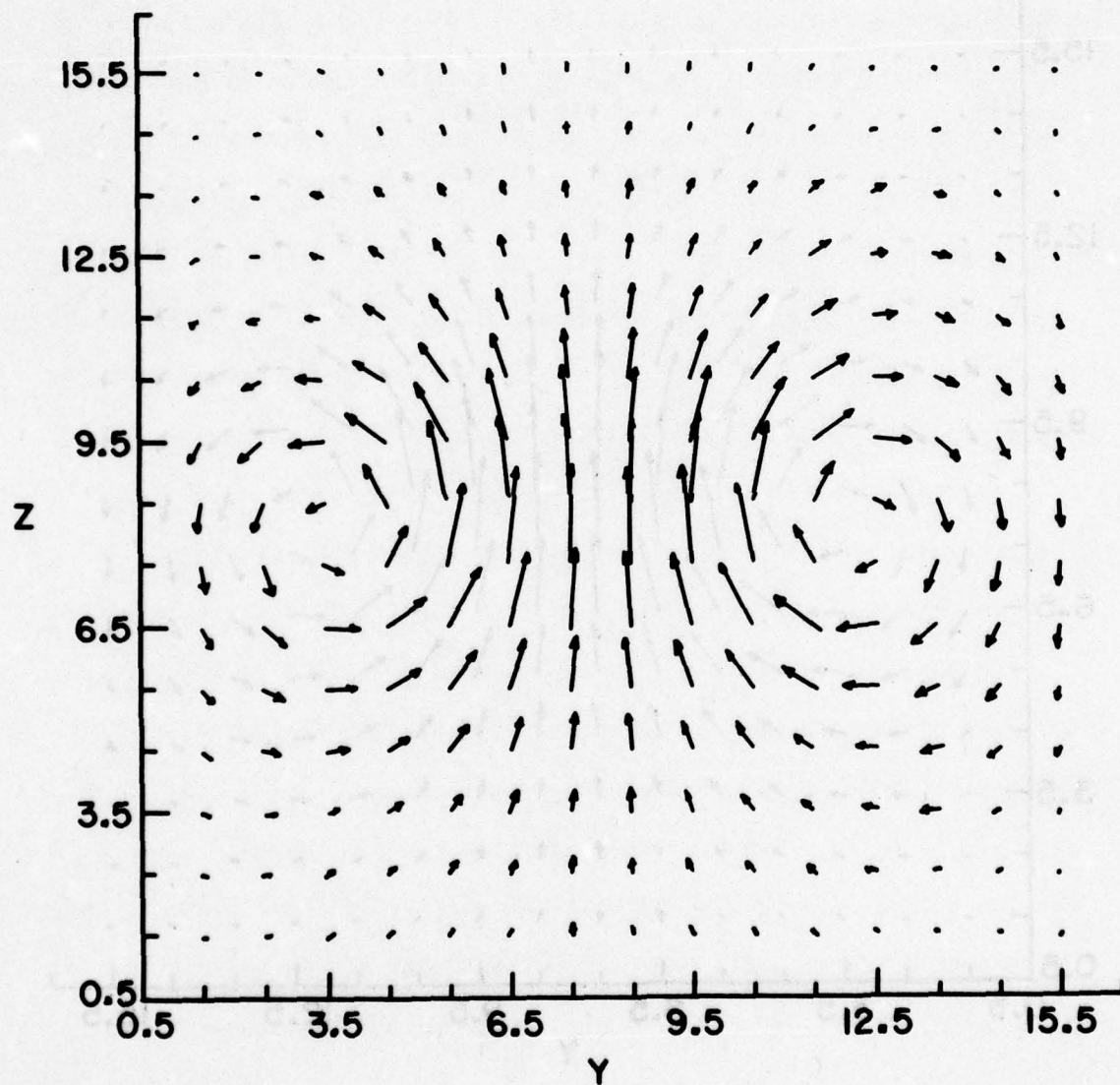
Figure 9. Projection on (x-y)-plane (z = 6.5) of the velocity field in the middle of the cells for a single vortex ring (R = 4) centered at (8,8,8) in a 16×16×16 mesh.
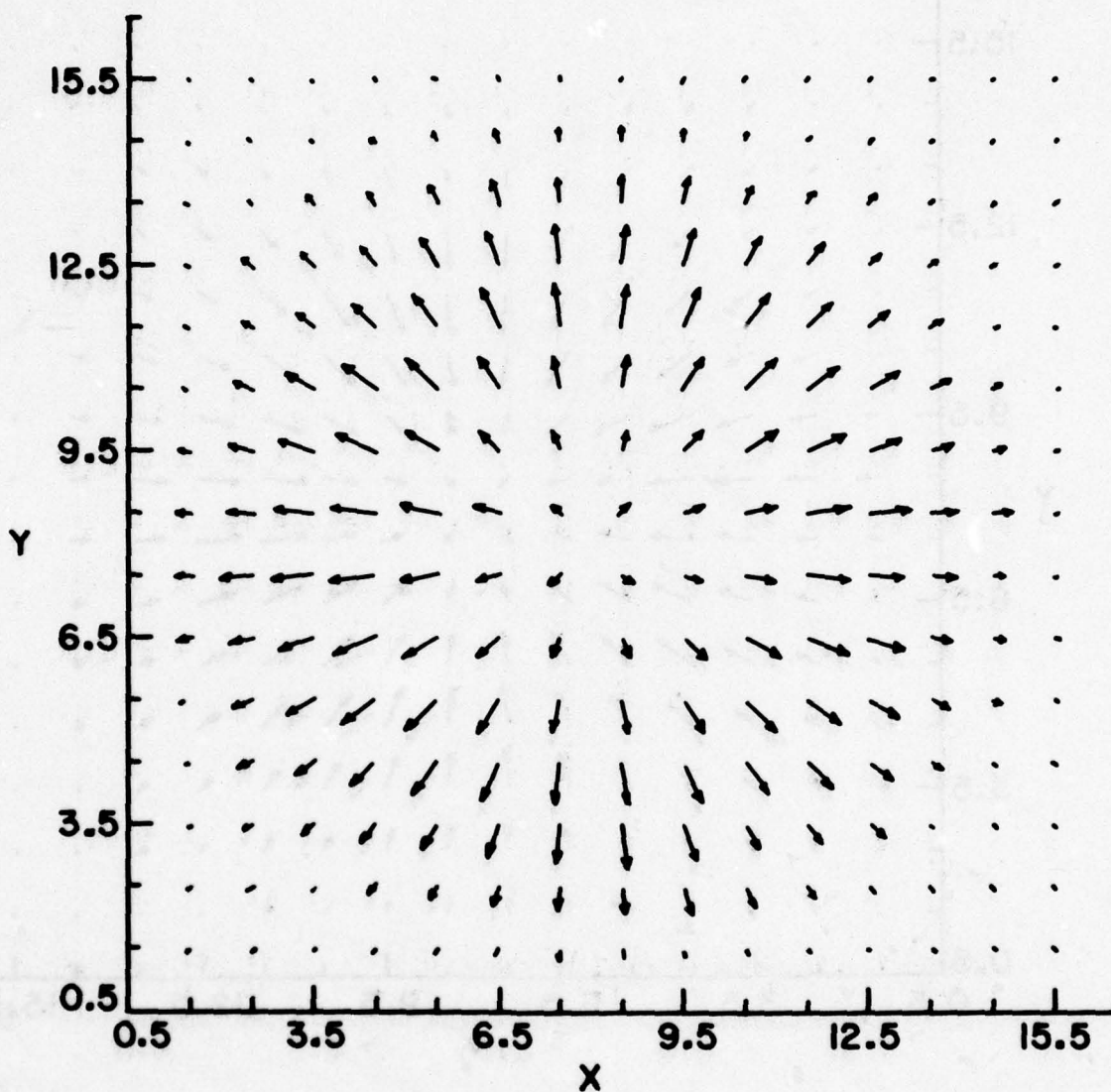
Figure 10. Projection on (x-y)-plane (z = 9.5) of the velocity field
in the middle of the cells for a single vortex ring (R = 4)
centered at (8,8,8) in a 16x16x16 mesh.

38
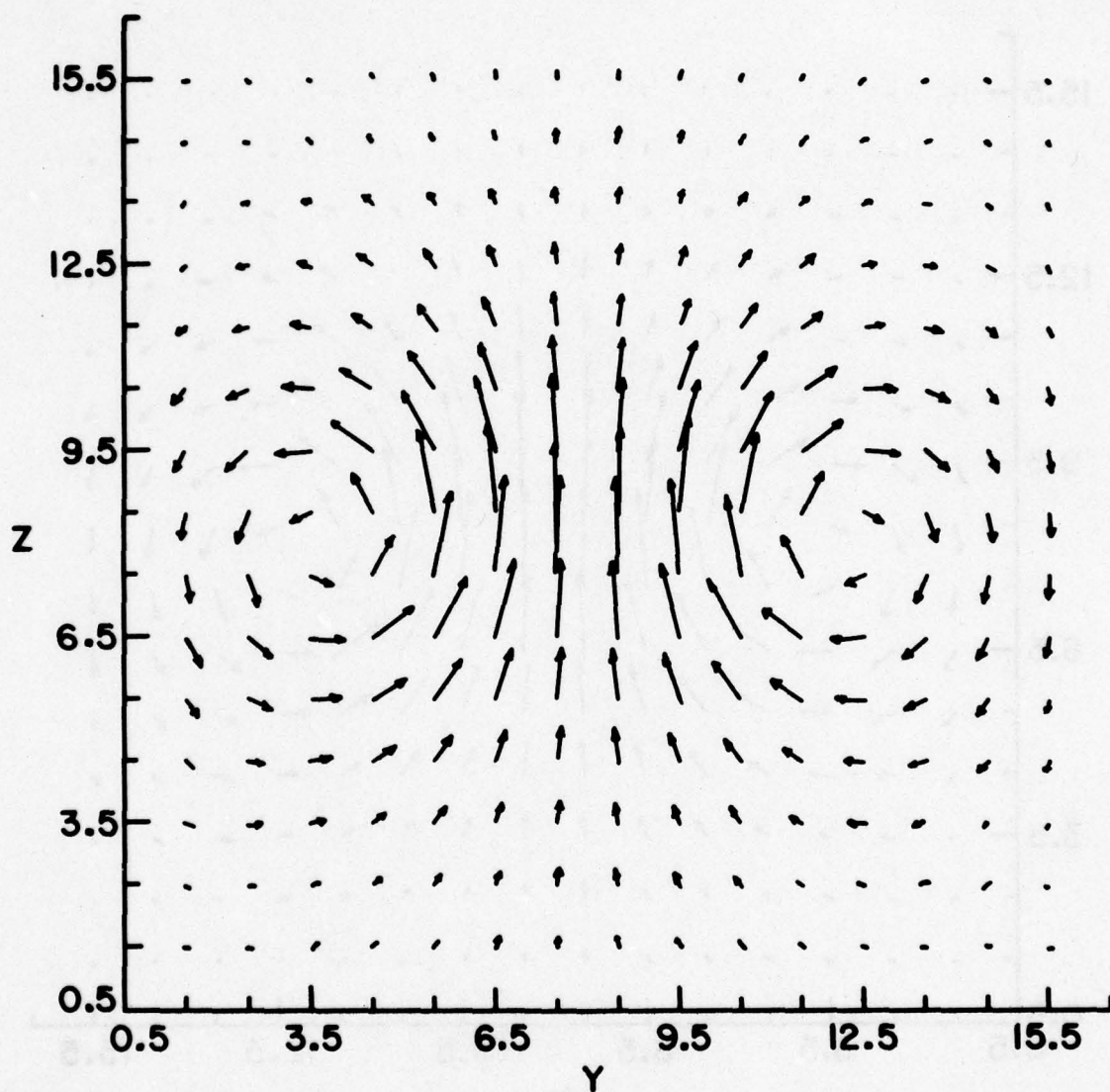
Figure 11. Projection on (y-z)-plane (x = 6.5) of the velocity field in the middle of the cells for a single vortex ring (R = 4) centered at (8,8,8) in a 16×16×16 mesh.

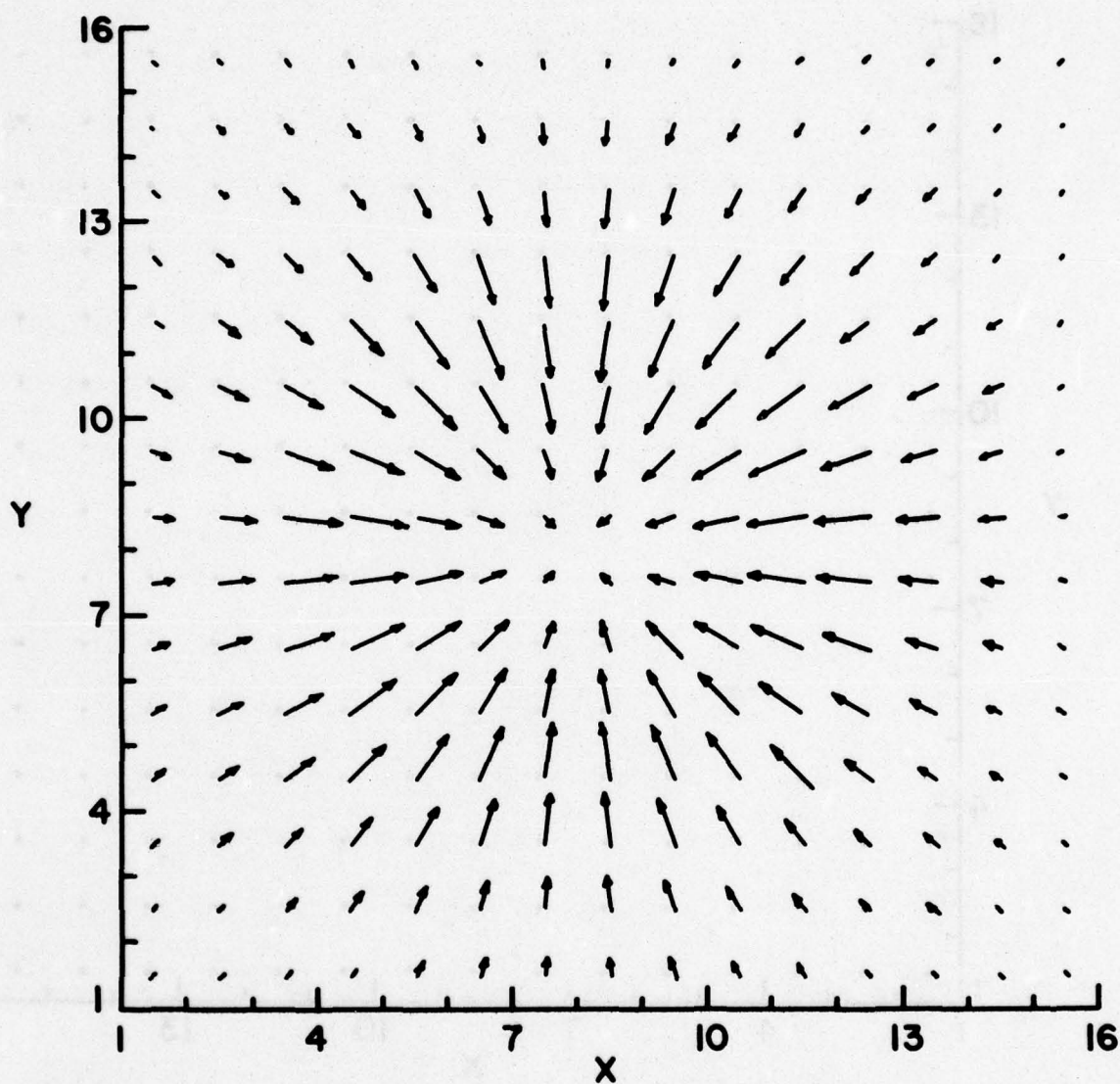Figure 12. Projection on (y-z)-plane (x = 9.5) of the velocity field
in the middle of the cells for a single vortex ring (R = 4)
centered at (8,8,8) in a 16×16×16 mesh.
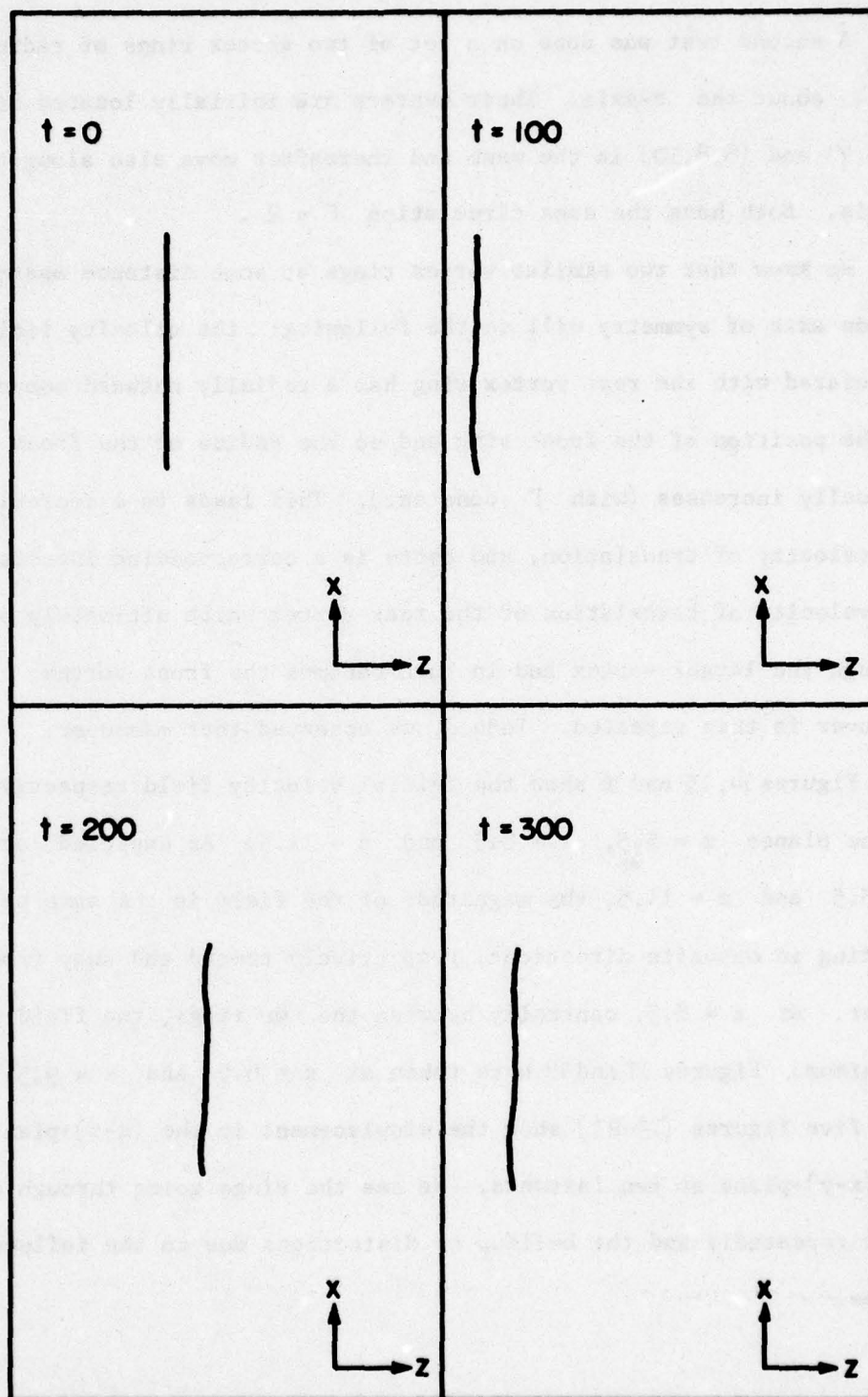
Figure 13. Displacement of a single vortex ring (R = 4) in a periodic space at four instants.

instants. We can see the constancy of the motion in time.

A second test was done on a set of two vortex rings of radius $R = 4$ about the z-axis. Their centers are initially located at $(8,8,7)$ and $(8,8,10)$ in the mesh and thereafter move also along the z-axis. Both have the same circulation $\Gamma = 2$.

We know that two similar vortex rings at some distance apart on a common axis of symmetry will do the following: the velocity field associated with the rear vortex ring has a radially outward component at the position of the front ring and so the radius of the front ring gradually increases (with Γ constant). This leads to a decrease in its velocity of translation, and there is a corresponding increase in the velocity of translation of the rear vortex which ultimately passes through the larger vortex and in turn becomes the front vortex. The maneuver is then repeated. Indeed, we observed that maneuver.

Figures 14, 15 and 16 show the initial velocity field respectively in the planes $z = 5.5$, $z = 8.5$ and $z = 11.5$. As expected, at $z = 5.5$ and $z = 11.5$, the magnitude of the field is the same but pointing in opposite directions, respectively toward and away from the center. At $z = 8.5$, centrally between the two rings, the field reaches a minimum. Figures 17 and 18 were taken at $x = 6.5$ and $x = 9.5$. The last five figures (19-23) show the displacement in the (x-z)-plane and the (x-y)-plane at ten instants. We see the rings going through each other repeatedly and the buildup of distortions due to the influence of images.

Figure 14. Projection on (x-y)-plane (z = 5.5) of the velocity field in the middle of the cells for a pair of vortex rings (R = 4) centered at (8,8,7) and (8,8,10) respectively in a 16×16×16 mesh.
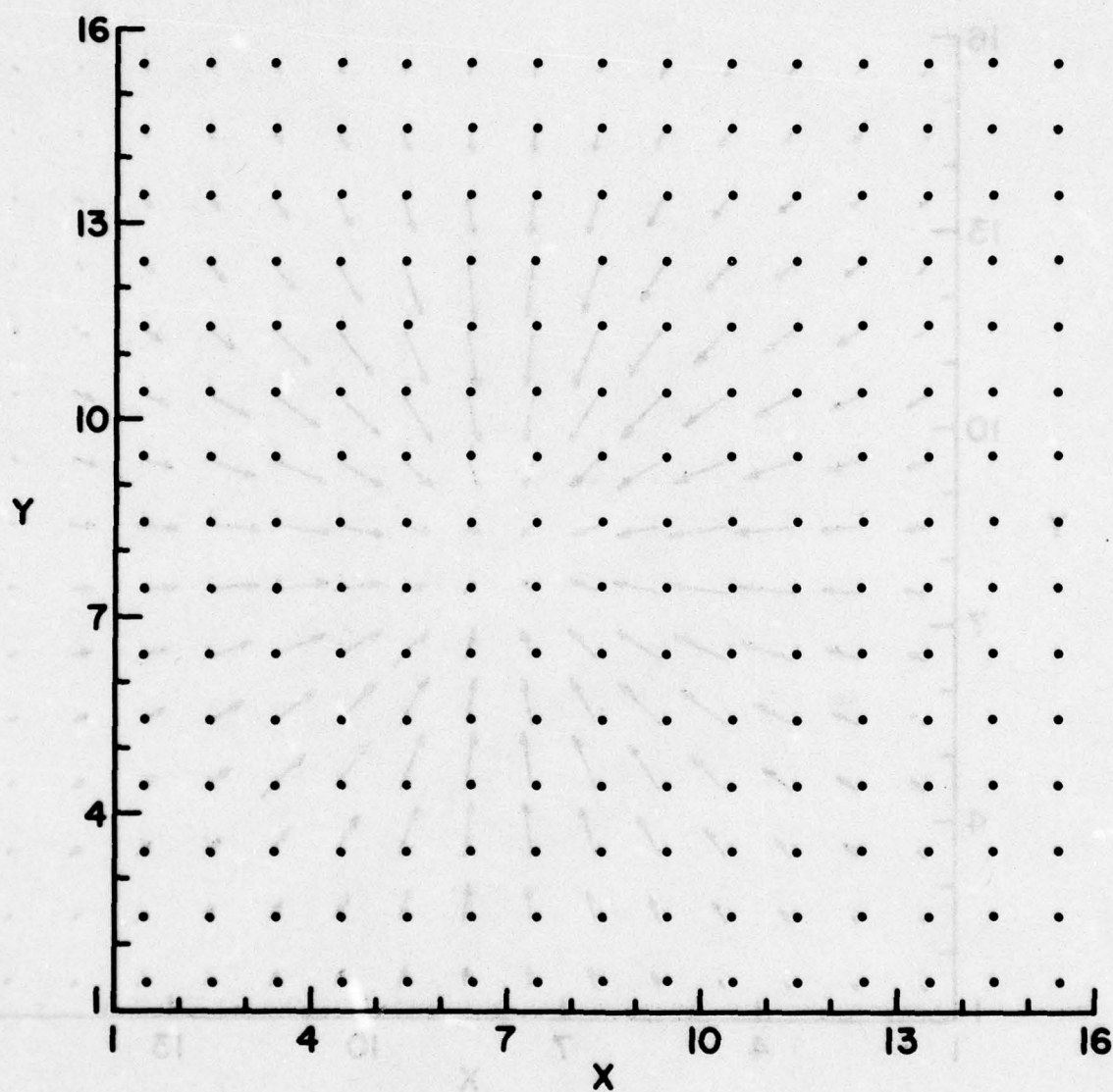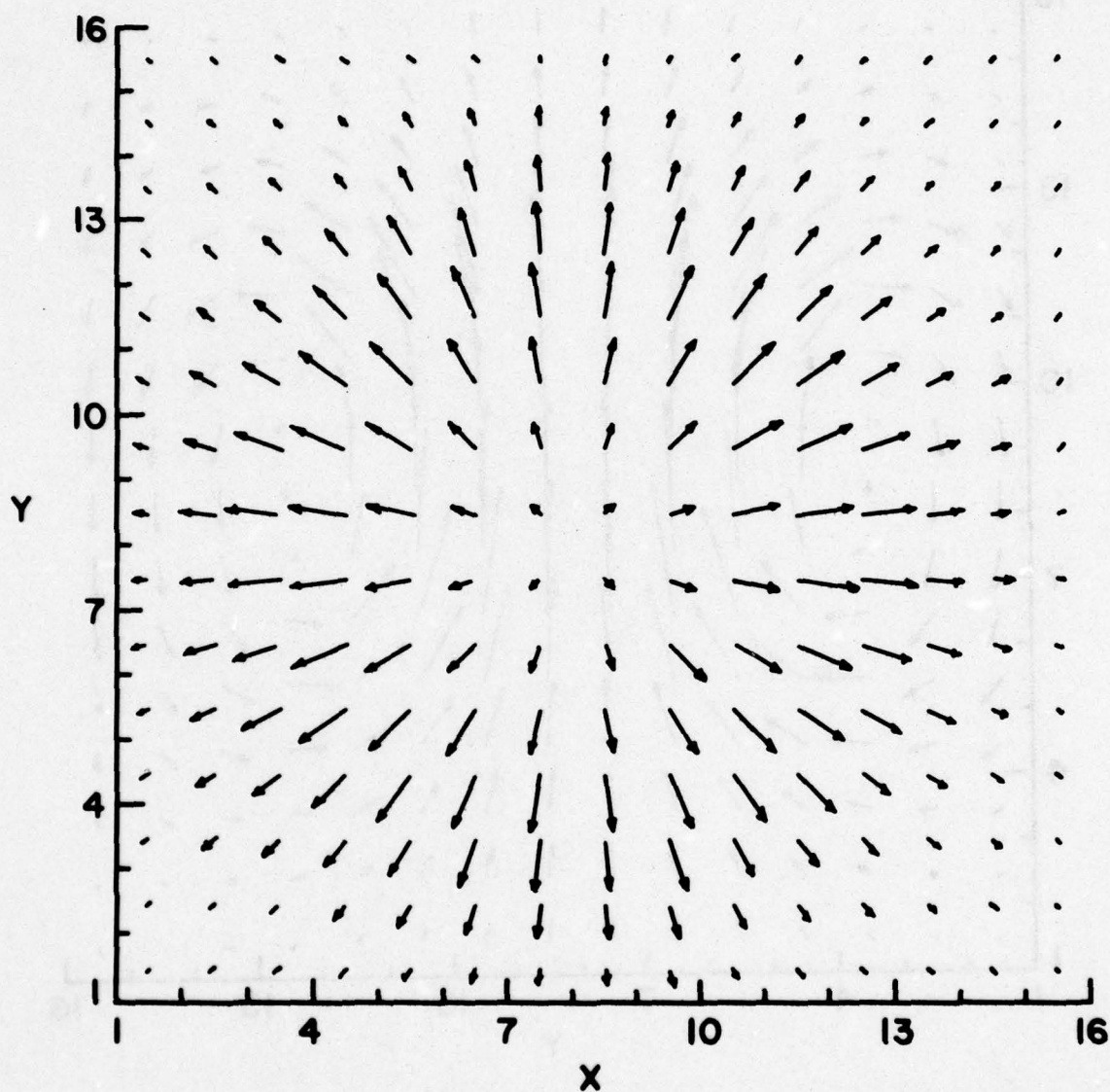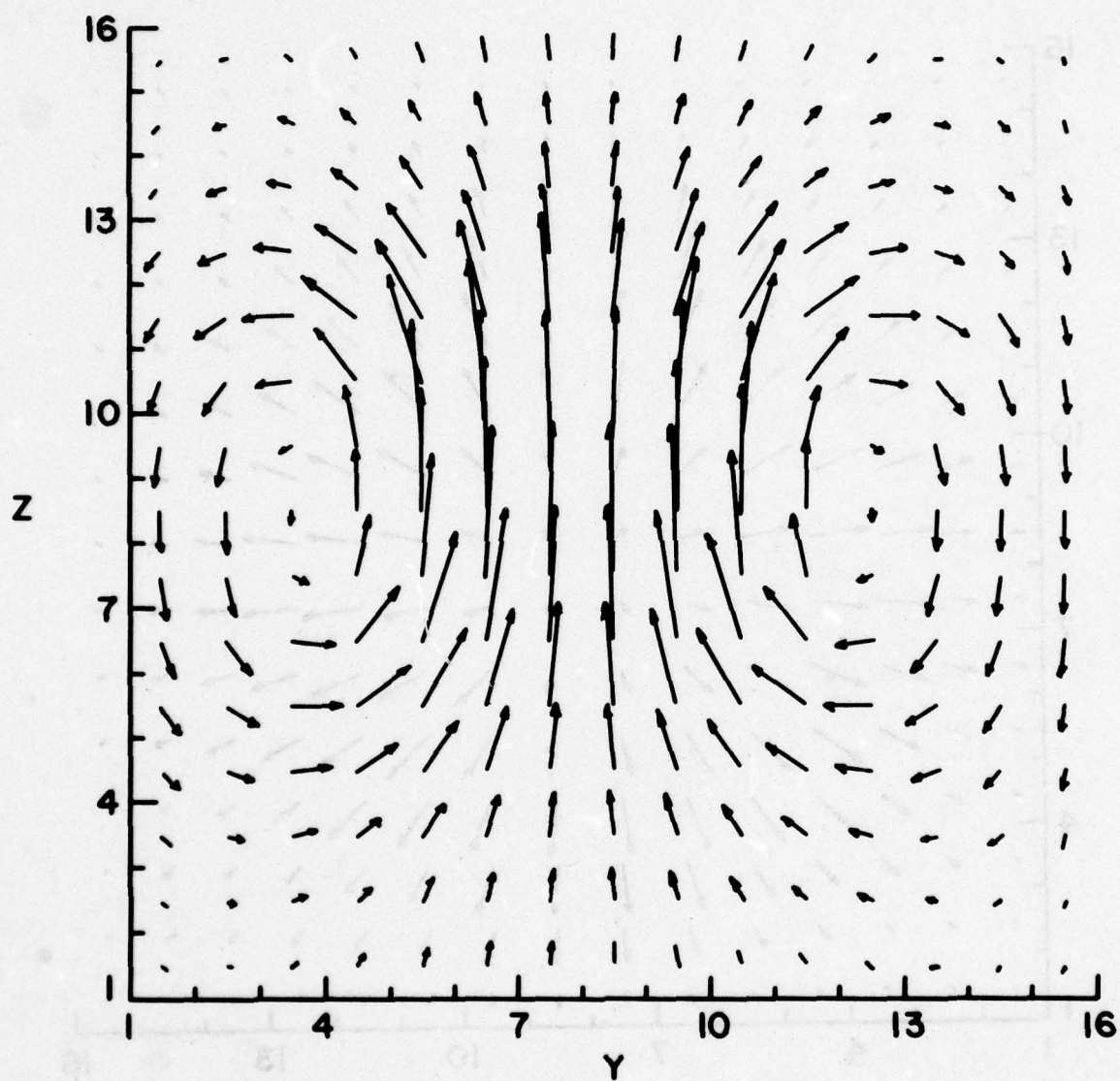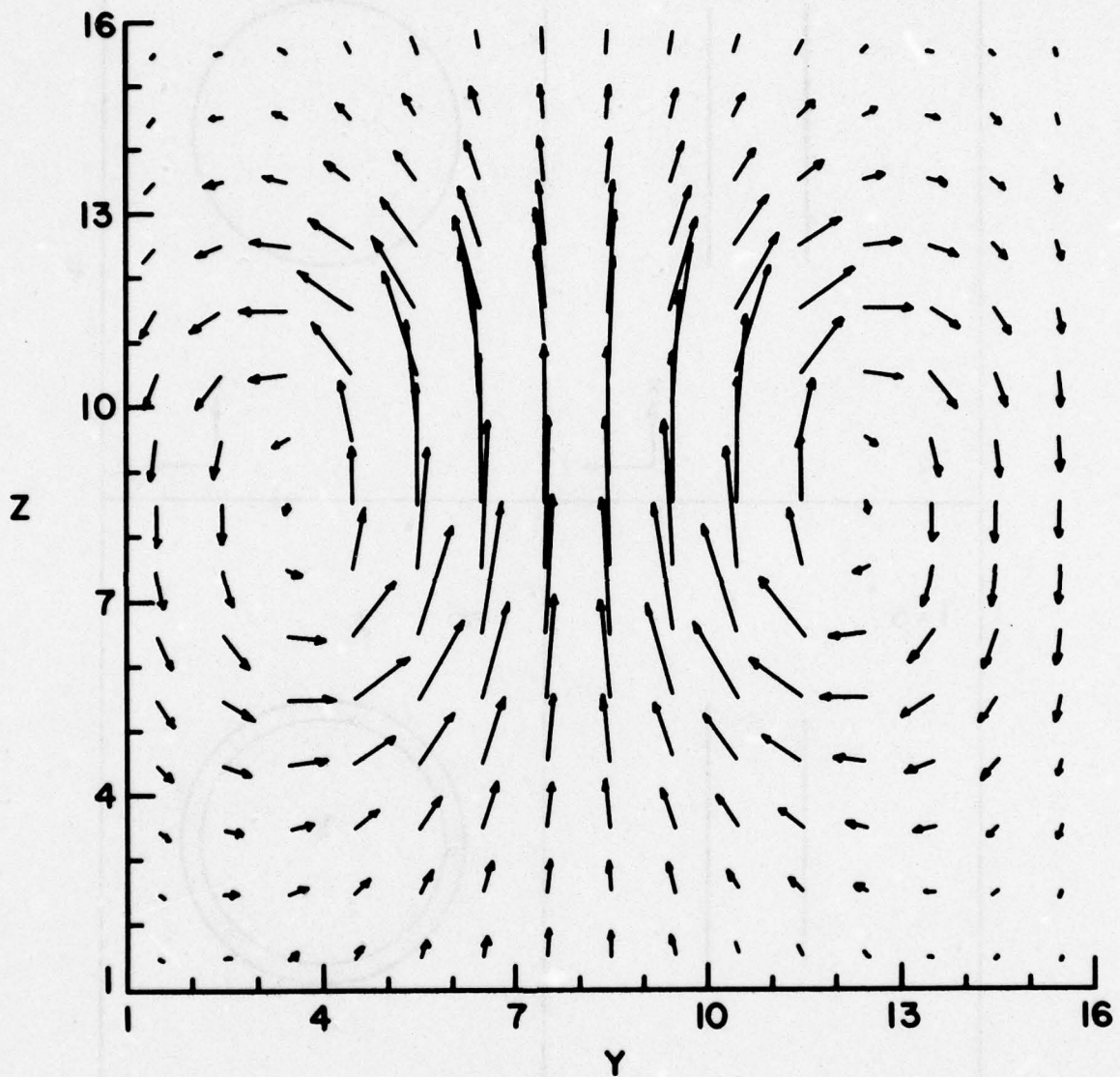
43

Figure 15. Projection on (x-y)-plane (z = 8.5) of the velocity field in
the middle of the cells for a pair of vortex rings (R = 4)
centered at (8,8,7) and (8,8,10) respectively in a 16×16×16 mesh.

Figure 16. Projection on (x-y)-plane (z = 11.5) of the velocity field in the middle of the cells for a pair of vortex rings (R = 4) centered at (8,8,7) and (8,8,10) respectively in a 16x16x16 mesh.

Figure 17.   Projection on (y-z)-plane (x = 6.5) of the velocity field in
the middle of the cells for a pair of vortex rings (R = 4)
centered at (8,8,7) and (8,8,10) respectively in a 16×16×16 mesh.

46

Figure 18. Projection on (y-z)-plane (x = 9.5) of the velocity field in
the middle of the cells for a pair of vortex rings (R = 4)
centered at (8,8,7) and (8,8,10) respectively in a 16×16×16 mesh.
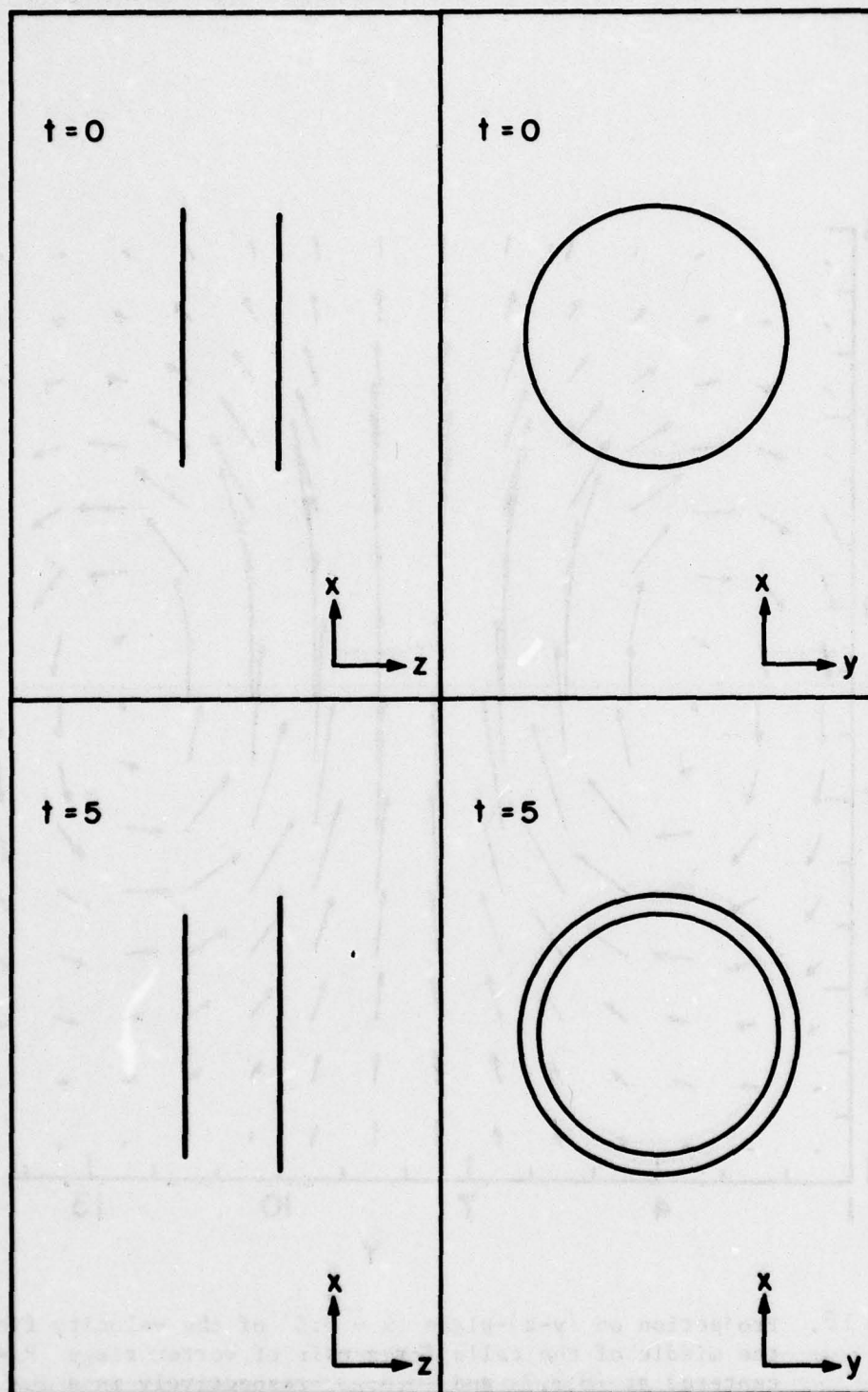
Figure 19. Displacement of a pair of vortex rings (R = 4) in a periodic space at ten instants.
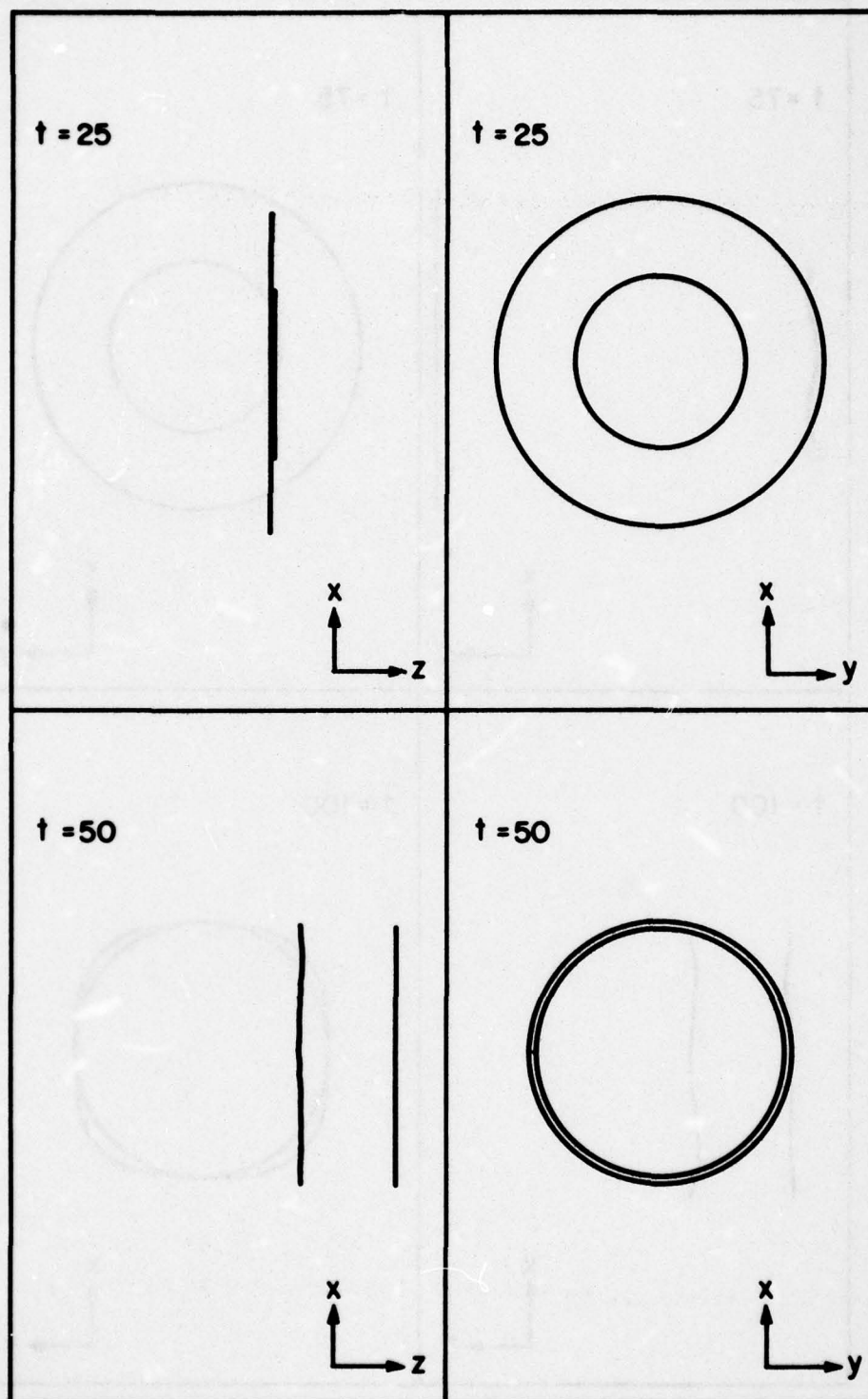
Figure 20. Continuation of Figure 19.
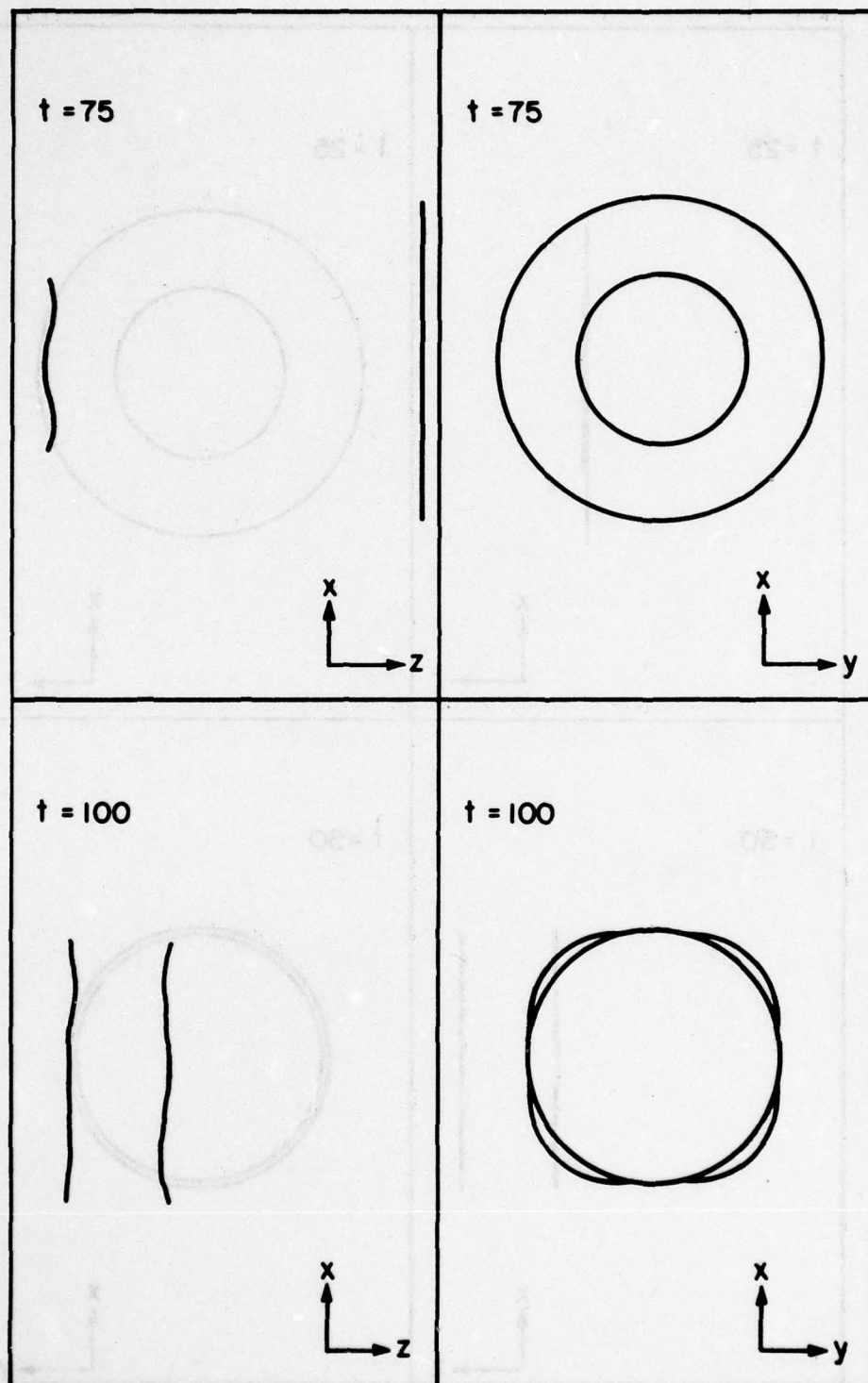
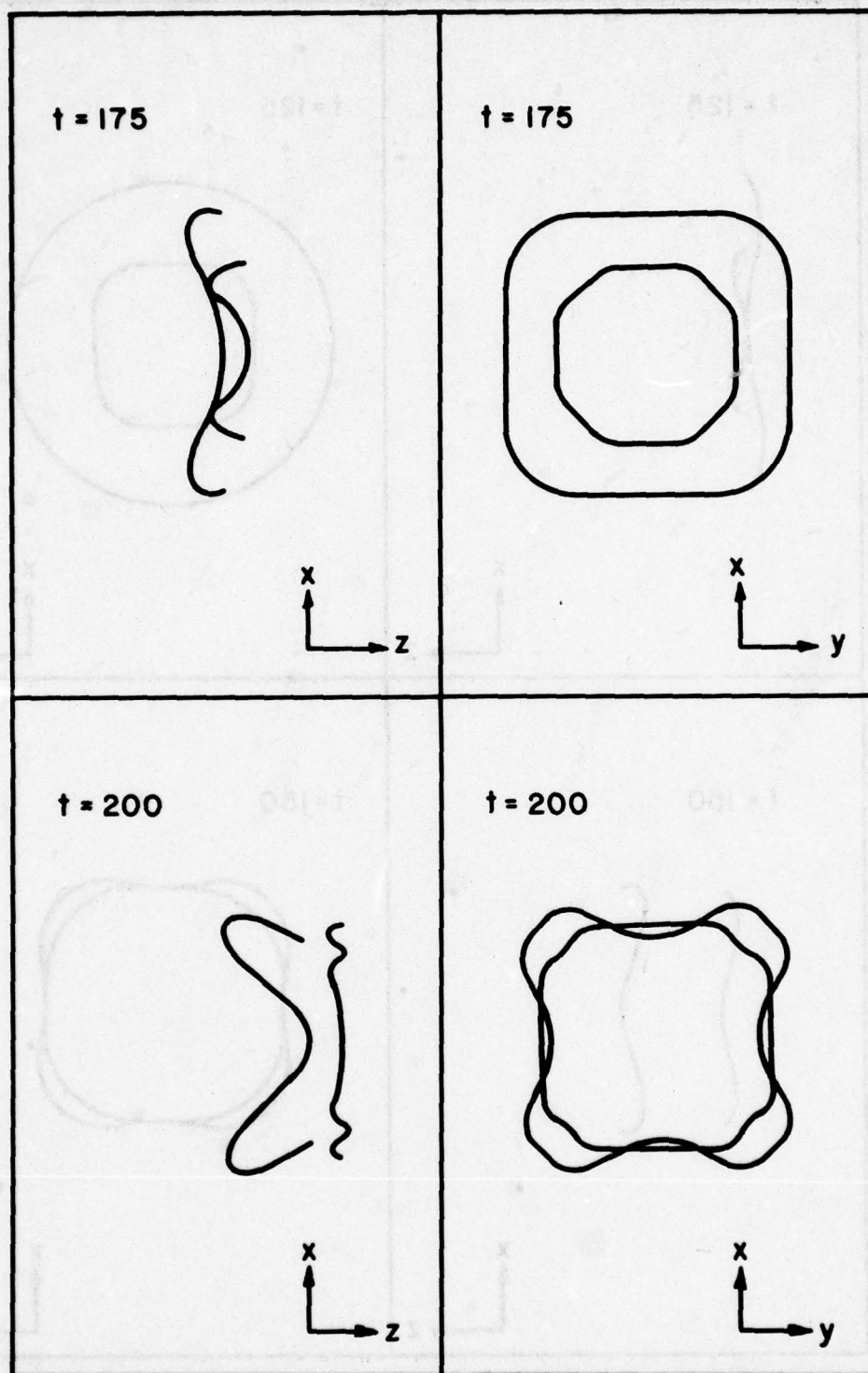Figure 21. Continuation of Figure 19.
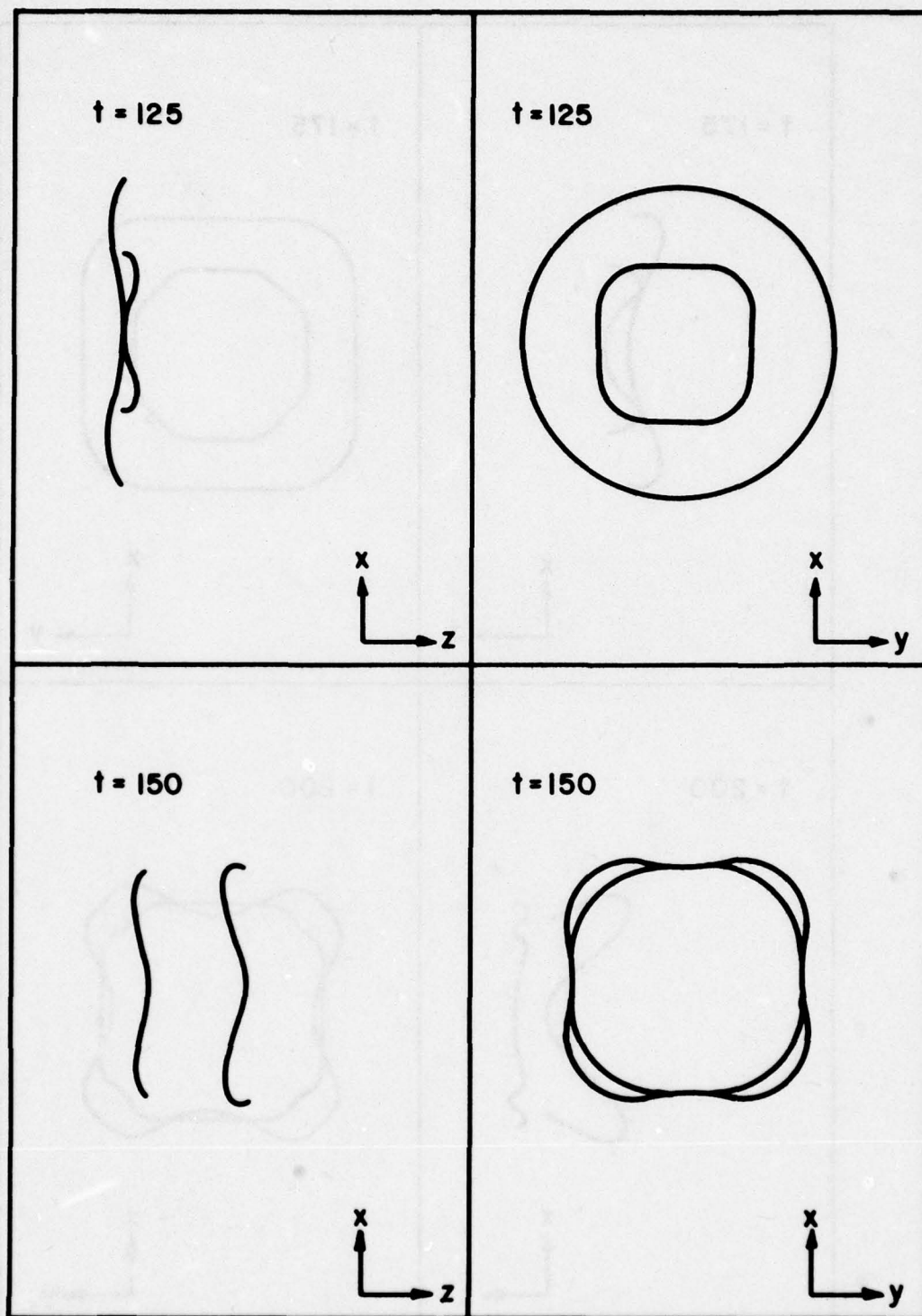
Figure 22. Continuation of Figure 19.

51

Figure 23. Continuation of Figure 19

52

IV.2 Taylor-Green Vortex System

In a classic paper, Taylor and Green[24] considered the dynamical evolution of a model three-dimensional vortex field in order to clarify the dynamics of turbulence. The relatively simple Taylor-Green flow pattern illustrates the basic turbulence decay mechanisms: production of small eddies and enhancement of dissipation. The latter is associated with an increase of vorticity and with the stretching of the vortex lines. The Taylor-Green system has also proved exceedingly useful for testing numerical and perturbation methods, as we will discuss below.

In their paper, Taylor and Green made an attempt to trace the subsequent motion of an infinite incompressible fluid with velocity components u_x, u_y, u_z, given initially by

$$u_x = A \cos(ax) \sin(by) \sin(cz)$$

$$u_y = B \sin(ax) \cos(by) \sin(cz) \qquad (4.7)$$

$$u_z = C \sin(ax) \sin(by) \cos(cz)$$

The arbitrarily assigned constants a, b, c, A, B, C, should fulfill the incompressibility condition, $\text{div}(\vec{u}) = 0$ or $Aa + Bb + Cc = 0$. The flow is triply periodic and a typical example of the initial flow pattern for a given set of constants is shown in Figures 24 and 25. At an early stage of their calculations, Taylor and Green realized that it was impossible to obtain significant results in the general case when the initial motion is represented by (4.7), so they confined their attention to a special case, namely $a = b = c$, $A = -B$ and $C = 0$.

$$u_x = A \cos(ax) \sin(ay) \sin(az)$$

$$u_y = -A \sin(ax) \cos(ay) \sin(az) \qquad (4.8)$$

$$u_z = 0$$

53

The motion remains periodic in x, y and z for all time, with wave-lengths $2\pi/a$ in each of the x,y and z directions. Taylor and Green used power series in the time t to find u_x, u_y, u_z, and the pressure p at time t. They took averages throughout a periodicity cube and deduced the series for the mean square vorticity, $\overline{\omega^2}$, as far as the term t^5.

In order that the effect of vortex lines stretching may be illustrated, the vortex motion must be three-dimensional and possess a definite scale. It is difficult to think of a motion possessing these characteristics for which the calculations would be easier than for the motion (4.8). That is the reason why the vortex system derived from (4.8) has undergone many analytical studies since the original paper of Taylor and Green[47-54]. Numerical solution of the Navier-Stokes equations (2.1) and (2.3) by a spectral method has also been applied[50] to the Taylor-Green system (4.8).

In our case, for reasons to be explained below, we went back to (4.7) and considered another special case, namely when a = b = c and -A = 2B = 2C .

$$u_x = 2A \cos(ax) \sin(ay) \sin(az)$$

$$u_y = -A \sin(ax) \cos(ay) \sin(az) \qquad (4.9)$$

$$u_z = -A \sin(ax) \sin(ay) \cos(az)$$

See Figures 24 and 25. This flow is symmetric in the coordinates y and z . The initial vorticity field $\vec{\omega} = \nabla \times \vec{u}$ is

$$\omega_x = 0$$

$$\omega_y = 3aA \cos(ax) \sin(ay) \cos(az) \qquad (4.10)$$

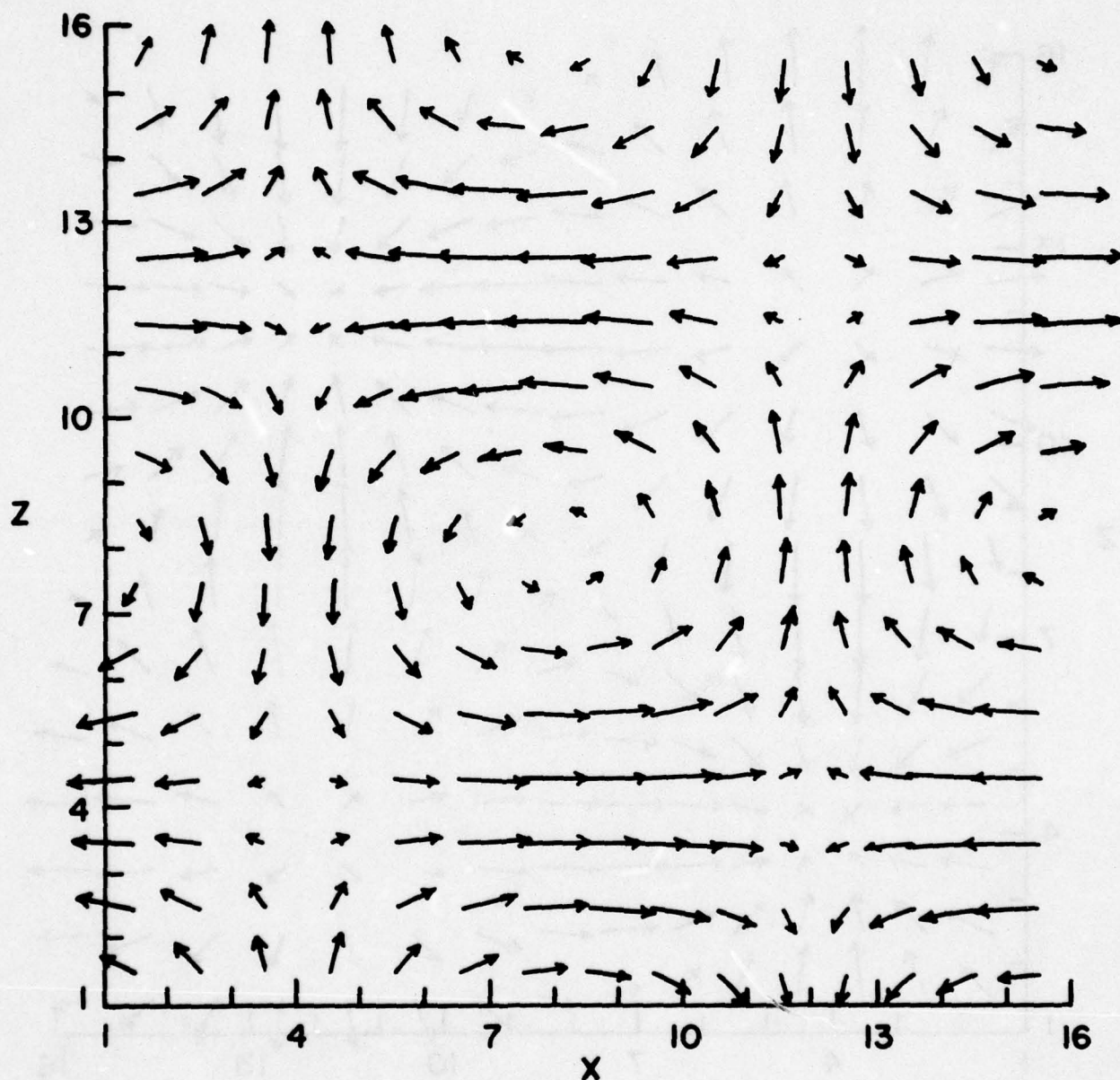$$\omega_z = 3aA \cos(ax) \cos(ay) \sin(az)$$

54

Figure 24. Projection on (x-z)-plane (y = 1.5) of the velocity field in the
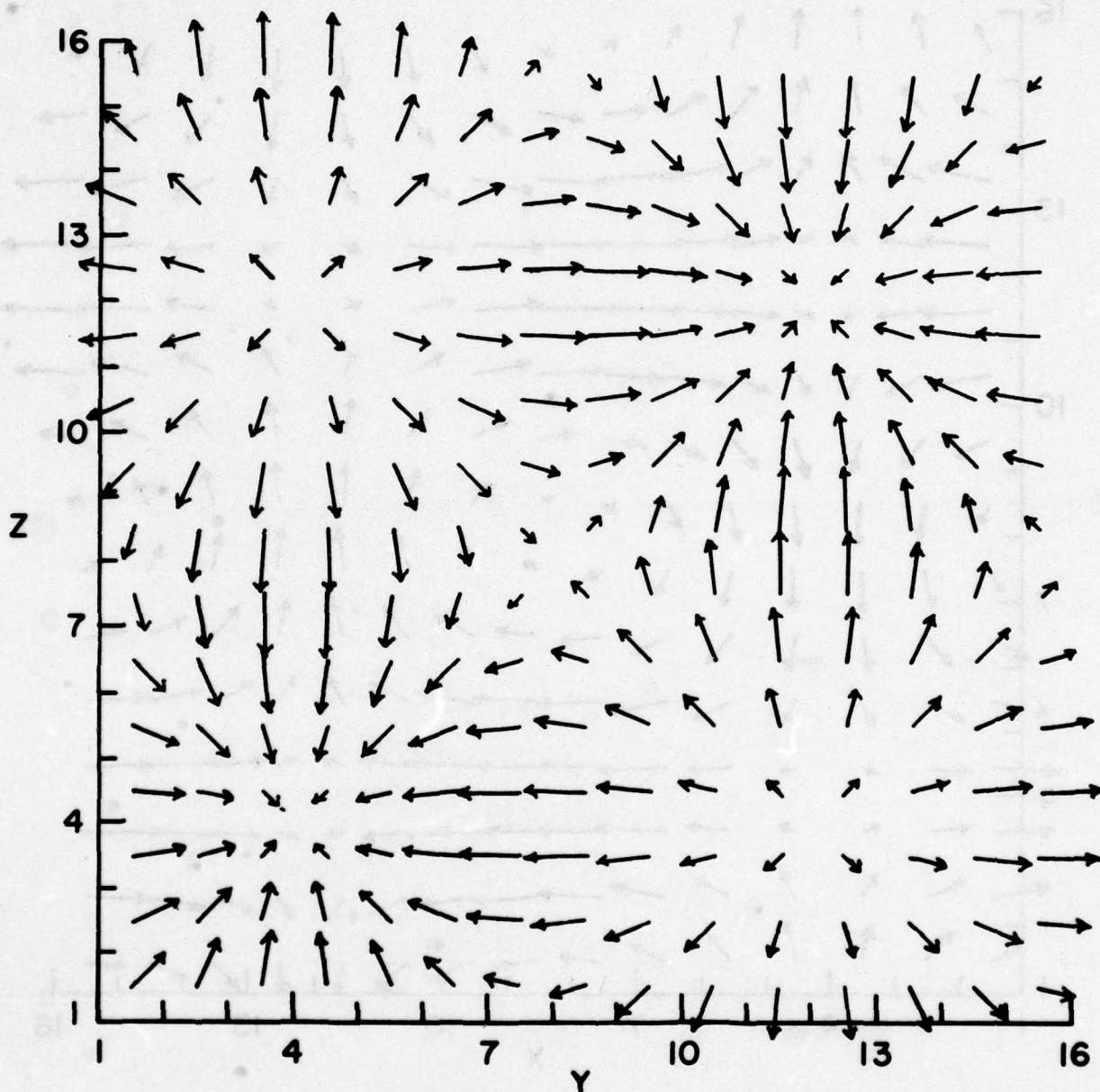middle of the cells for a Taylor-Green system (eq. 4.9) in a
16x16x16 mesh.

55

Figure 25. Projection on (y-z)-plane (x = 5.5) of the velocity field in the middle of the cells for a Taylor-Green system (eq. 4.9) in a 16×16×16 mesh.

The initial vortex lines are the planar curves

$$\sin(ay) \sin(az) = \text{const.}$$

in the planes $x = \text{const.}$

See Figure 26 for an illustration of the vortex lines.

The quantity $\vec{w} \cdot \vec{\nabla u}$, which represents amplification and rotation of the vorticity vector by the strain rate[19], is initially nonzero. Therefore, the vortex lines given by Eq. 4.11 will induce a velocity field which, while transporting the lines, may also change their lengths. Also, since the initial value of each component of $(\vec{u} \times \vec{w})$ is nonzero, the three components of velocity continue to be nonzero after the initial instant and the field becomes truly three-dimensional. (4.8) and (4.9) are perhaps the simplest examples of self-induced vortex stretching in a three-dimensional velocity field. We chose to study the system (4.9) mainly because the vortex lines (4.11) (which we trace numerically in our code) are easier to define and discretize than the ones resulting from the system (4.8) which are the twisted curves

$$\sin(ax)/\sin(ay) = \text{const.}, \quad \sin^2(ax) \cos(az) = \text{const.}$$

On the other hand, we do not know of any paper describing a perturbation analysis of the motion initiated by (4.9). Therefore, before going into the details of the numerical simulation we will investigate the evolution of our Taylor-Green vortex system (4.9) by developing a perturbation solution to the Navier-Stokes equations (2.1), (2.3) in powers of the Reynolds number Re rather than in powers of the time t . Goldstein[47] developed such a series solution for the system (4.8) and found that this series is more inclusive than a series in time t in the sense that each term of his series was a resummation of an infinite number of
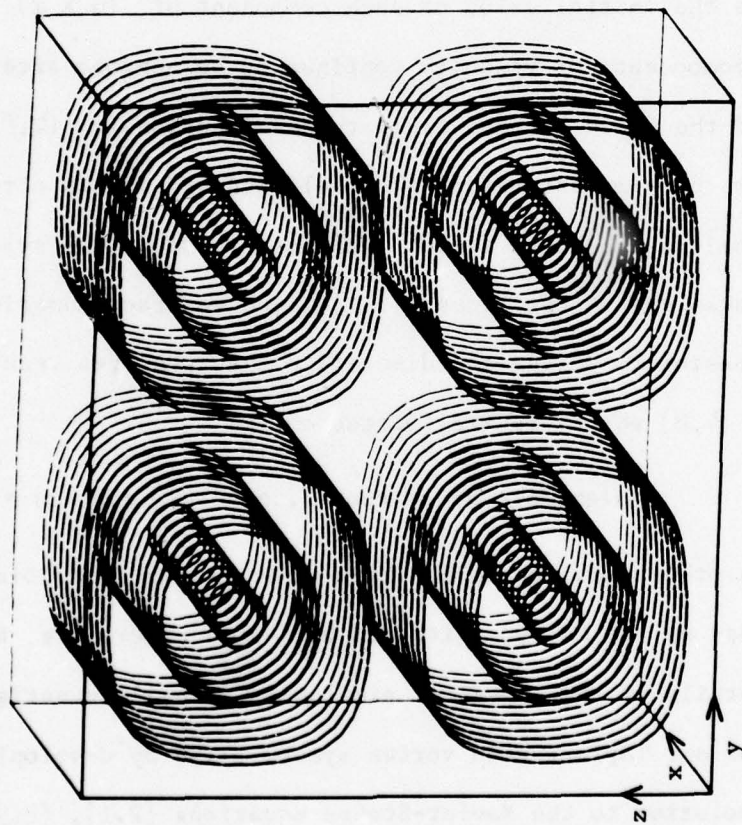
57

Figure 26. Illustration of the vortex lines for a Taylor-Green system (eq. 4.9) at $t = 0$.

partial terms of Taylor and Green's series. It can also be shown that each term of the series in time is derived from only a finite number of terms of the series in Re .

The dynamical problem is to solve the Navier-Stokes equations for incompressible flow:

$$\frac{\partial \vec{u}}{\partial t} + \vec{u} \cdot \nabla \vec{u} = -\frac{1}{\rho} \nabla p + \nu \nabla^2 \vec{u} \qquad (2.1)$$

$$\nabla \cdot \vec{u} = 0 \qquad (2.3)$$

subject to the (incompressible) initial conditions (4.9). The pressure field in (2.1) is effectively a "Lagrange multiplier" that insures compliance with the incompressibility constraint (2.3). Taking the divergence of the equation of motion (2.1) and applying the equation of continuity (2.3), we find the following equation for the pressure:

$$\frac{-1}{\rho} \nabla^2 p = \left(\frac{\partial u_x}{\partial x}\right)^2 + \left(\frac{\partial u_y}{\partial y}\right)^2 + \left(\frac{\partial u_z}{\partial z}\right)^2$$

$$+ 2\left(\frac{\partial u_y}{\partial x} \frac{\partial u_x}{\partial y} + \frac{\partial u_z}{\partial y} \frac{\partial u_y}{\partial z} + \frac{\partial u_x}{\partial z} \frac{\partial u_z}{\partial x}\right) \qquad (4.12)$$

We reduce all the equations to non-dimensional form by writing

$$u'_x = \frac{u_x}{A} , \quad u'_y = \frac{u_y}{A} , \quad u'_z = \frac{u_z}{A} , \quad p' = \frac{p}{\rho A^2} ,$$

$$x' = ax, \ y' = ay, \ z' = az, \ t' = Aat , \qquad (4.13)$$

$$\omega'_x = \frac{\omega_x}{aA} , \quad \omega'_y = \frac{\omega_y}{aA} , \quad \omega'_z = \frac{\omega_z}{aA} ,$$

$$Re = \frac{A}{\nu a}$$

59

From then on, to simplify the notation, we drop the prime so that equations (2.3), (2.1), and (4.12) become

$$\nabla \cdot \vec{u} = 0 \qquad (4.14)$$

$$\frac{\partial \vec{u}}{\partial t} + \vec{u} \cdot \nabla \vec{u} = - \nabla p + \frac{1}{Re} \nabla^2 \vec{u} \qquad (4.15)$$

$$- \nabla^2 p = \left(\frac{\partial u_x}{\partial x}\right)^2 + \left(\frac{\partial u_y}{\partial y}\right)^2 + \left(\frac{\partial u_z}{\partial z}\right)^2$$

$$+ 2 \left(\frac{\partial u_y}{\partial x} \frac{\partial u_x}{\partial y} + \frac{\partial u_z}{\partial y} \frac{\partial u_y}{\partial z} + \frac{\partial u_x}{\partial z} \frac{\partial u_z}{\partial x}\right). \qquad (4.16)$$

The initial conditions (4.9) are

$$u_x = 2 \cos(x) \sin(y) \sin(z)$$

$$u_y = - \sin(x) \cos(y) \sin(z) \qquad (4.17)$$

$$u_z = - \sin(x) \sin(y) \cos(z)$$

at $t = 0$.

For small values of the Reynolds number the last term in (4.15) dominates while the quadratic terms remain bounded and may be neglected; thus we have to solve the equation

$$\frac{\partial \vec{u}}{\partial t} = \frac{1}{Re} \nabla^2 \vec{u} \qquad (4.18)$$

with the initial conditions (4.17). The solution is

$$u_{x0} = 2 e^{-3t/Re} \cos(x) \sin(y) \sin(z)$$

$$u_{y0} = - e^{-3t/Re} \sin(x) \cos(y) \sin(z) \qquad (4.19)$$

$$u_{z0} = - e^{-3t/Re} \sin(x) \sin(y) \cos(z)$$

For the second approximation, we substitute from (4.19) into the quadratic terms in (4.15) and into (4.16), solve (4.16) for p , substitute the value found for p into (4.15), and then solve (4.15) again for $\vec{u}$. This process is equivalent to substituting

$$t/Re = T ,\qquad (4.20)$$

expanding $\vec{u}$, p in series

$$\vec{u} = \vec{u}_0 + \vec{u}_1 Re + \vec{u}_2 Re^2 + \vec{u}_3 Re^3 + \ldots\ldots ,$$

$$(4.21)$$

$$p = p_0 + p_1 Re + p_2 Re^2 + p_3 Re^3 + \ldots\ldots ,$$

substituting into (4.15) and (4.16) and equating coefficients of powers of Re . In this way we find the equations

$$- \nabla^2 p_0 = \left(\frac{\partial u_{x0}}{\partial x}\right)^2 + \left(\frac{\partial u_{y0}}{\partial y}\right)^2 + \left(\frac{\partial u_{z0}}{\partial z}\right)^2$$

$$+ 2\left(\frac{\partial u_{y0}}{\partial x}\frac{\partial u_{x0}}{\partial y} + \frac{\partial u_{z0}}{\partial y}\frac{\partial u_{y0}}{\partial z} + \frac{\partial u_{x0}}{\partial z}\frac{\partial u_{z0}}{\partial x}\right)$$

$$- \nabla^2 p_1 = \frac{2\partial u_{x0}}{\partial x}\frac{\partial u_{x1}}{\partial x} + \frac{2\partial u_{y0}}{\partial y}\frac{\partial u_{y1}}{\partial y} + \frac{2\partial u_{z0}}{\partial z}\frac{\partial u_{z1}}{\partial z} \qquad (4.22)$$

$$+ 2\left(\frac{\partial u_{y0}}{\partial x}\frac{\partial u_{x1}}{\partial y} + \frac{\partial u_{y1}}{\partial x}\frac{\partial u_{x0}}{\partial y} + \frac{\partial u_{z0}}{\partial y}\frac{\partial u_{y1}}{\partial z} + \frac{\partial u_{z1}}{\partial y}\frac{\partial u_{y0}}{\partial z}\right.$$

$$\left. + \frac{\partial u_{x0}}{\partial z}\frac{\partial u_{z1}}{\partial x} + \frac{\partial u_{x1}}{\partial z}\frac{\partial u_{z0}}{\partial x}\right)$$

and so on, together with

61

$$\nabla^2 \vec{u}_1 - \frac{\partial \vec{u}_1}{\partial T} = \vec{u}_0 \cdot \nabla \vec{u}_0 + \nabla p_0$$

(4.23)

$$\nabla^2 \vec{u}_2 - \frac{\partial \vec{u}_2}{\partial T} = \vec{u}_0 \cdot \nabla \vec{u}_1 + \vec{u}_1 \cdot \nabla \vec{u}_0 + \nabla p_1$$

and so on. The solutions required for p_0, p_1, etc., are the periodic solutions; the solutions required for $\vec{u}_1$, $\vec{u}_2$, etc., are periodic, and are zero when $T = 0$.

Substituting from (4.19) into the first of equations (4.22) we find that

$$\nabla^2 p_0 = \tfrac{1}{2} e^{-6T} \Big(4 \cos(2x) + \cos(2y) + \cos(2z) - \cos(2x) \cos(2y)$$

(4.24)

$$- \cos(2x) \cos(2z) - 4 \cos(2y) \cos(2z) \Big)$$

Hence

$$p_0 = -\frac{1}{16} e^{-6T} \Big(8 \cos(2x) + 2 \cos(2y) + 2 \cos(2z) - \cos(2x) \cos(2y)$$

$$- \cos(2x) \cos(2z) - 4 \cos(2y) \cos(2z) \Big)$$

(4.25)

From the first of equations (4.23), it may now be found that

$$\nabla^2 u_{y1} - \frac{\partial u_{y1}}{\partial T} = - \frac{3}{8} e^{-6T} \Big(\cos(2x) \sin(2y) \Big)$$

(4.26)

Also $u_{y1} = 0$ when $T = 0$. Hence

$$u_{y1} = - f_1 \cos(2x) \sin(2y)$$

(4.27)

where

$$f_1 = \frac{3}{16} \left(e^{-8T} - e^{-6T} \right)$$

$$= - 3 \left(\frac{T}{8} - \frac{7 T^2}{8} + \frac{37 T^3}{12} - \frac{175 T^4}{24} + \ldots \right)$$

(4.28)

62

u_{z1} may be found similarly. It is easy to see from the expressions for $\vec{u}_0$, p_0 that the expression for u_{z1} may be obtained from that u_{y1} by interchanging y and z. Hence

$$u_{z1} = -f_1 \cos(2x) \sin(2z) \tag{4.29}$$

After verifying that u_{x1} contains no term independent of x, we find u_{x1} from the equation of continuity, the result being

$$u_{x1} = f_1 \left(\sin(2x) \cos(2z) + \sin(2x) \cos(2y) \right) \tag{4.30}$$

Proceeding in the same way, we find the following expressions for p_1, $\vec{u}_2$, p_2, $\vec{u}_3$. See Tables 1, 2, and 3. We note that the expression for u_{z2} is obtained from that for u_{y2} by interchanging y and z, and so on. From the first velocity approximation (i.e. $\vec{u}_0$) on, if one expands the exponential factors (e^{-3T}, f_1, the g's, h_1) in Taylor series, one can show that these factors are ascending powers in T starting respectively from the zeroth order in T up. Considering (4.20) and (4.21), we conclude that the solution of the equation of motion, for large Reynolds number and for sufficiently small values of t, can be represented by

$$\vec{u} = \vec{u}_0^{(0)}(x,y,z) + \vec{u}_1^{(1)}(x,y,z)\, t + \vec{u}_2^{(2)}(x,y,z)\, t^2 + \ldots \tag{4.31}$$

where $\vec{u}_n^{(n)}(x,y,z)$ is the factor of T^n in the expansion of $\vec{u}_n$, $n = 0, 1, 2, 3, \ldots$.

TABLE 1

Expressions for p_1 and $\vec{u}_2$

	p_1	u_{x2}	u_{y2}	u_{z2}
$\sin(3x)\,\sin(y)\,\sin(z)$	$\frac{9}{44}(e^{-11T} - e^{-9T})$	0	0	0
$\sin(x)\,\sin(y)\,\sin(3z)$	$\frac{9}{88}(e^{-11T} - e^{-9T})$	0	0	0
$\sin(x)\,\sin(3y)\,\sin(z)$	$\frac{9}{88}(e^{-11T} - e^{-9T})$	0	0	0
$\cos(x)\,\sin(y)\,\sin(z)$	0	$\frac{22}{3}g_1$	0	0
$\cos(3x)\,\sin(y)\,\sin(z)$	0	$\frac{38}{11}g_2$	0	0
$\cos(x)\,\sin(3y)\,\sin(z)$	0	$-\frac{23}{11}g_2$	0	0
$\cos(x)\,\sin(y)\,\sin(3z)$	0	$-\frac{23}{11}g_2$	0	0
$\cos(3x)\,\sin(3y)\,\sin(z)$	0	$-\frac{11}{19}g_3$	0	0
$\cos(3x)\,\sin(y)\,\sin(3z)$	0	$-\frac{11}{19}g_3$	0	0
$\sin(x)\,\cos(y)\,\sin(z)$	0	0	$-\frac{11}{3}g_1$	0
$\sin(x)\,\cos(3y)\,\sin(z)$	0	0	$\frac{8}{11}g_2$	0
$\sin(x)\,\cos(y)\,\sin(3z)$	0	0	$-\frac{1}{11}g_2$	0
$\sin(3x)\,\cos(y)\,\sin(z)$	0	0	$-\frac{57}{11}g_2$	0
$\sin(3x)\,\cos(3y)\,\sin(z)$	0	0	$\frac{11}{19}g_3$	0
$\sin(x)\,\sin(y)\,\cos(z)$	0	0	0	$-\frac{11}{3}g_1$
$\sin(x)\,\sin(y)\,\cos(3z)$	0	0	0	$\frac{8}{11}g_2$
$\sin(x)\,\sin(3y)\,\cos(z)$	0	0	0	$-\frac{1}{11}g_2$
$\sin(3x)\,\sin(y)\,\cos(z)$	0	0	0	$-\frac{57}{11}g_2$
$\sin(3x)\,\sin(y)\,\cos(3z)$	0	0	0	$\frac{11}{19}g_3$

TABLE 2

Expressions for p_2 and $\vec{u}_3$

	p_2	u_{x3}	u_{y3}	u_{z3}
$\cos(2x)$	l_1	0	0	0
$\cos(2y)$	l_2	0	0	0
$\cos(2z)$	l_2	0	0	0
$\cos(2y)\cos(2z)$	l_3	0	0	0
$\cos(2x)\cos(2y)$	l_4	0	0	0
$\cos(2x)\cos(2z)$	l_4	0	0	0
$\cos(2x)\cos(2y)\cos(2z)$	l_5	0	0	0
$\cos(4x)$	l_6	0	0	0
$\cos(4y)$	l_7	0	0	0
$\cos(4z)$	l_7	0	0	0
$\cos(4x)\cos(2y)\cos(2z)$	l_8	0	0	0
$\cos(4x)\cos(2y)$	l_9	0	0	0
$\cos(4x)\cos(2z)$	l_9	0	0	0
$\cos(4y)\cos(2z)$	l_{10}	0	0	0
$\cos(2y)\cos(4z)$	l_{10}	0	0	0
$\cos(2x)\cos(4y)$	l_{11}	0	0	0
$\cos(2x)\cos(4z)$	l_{11}	0	0	0
$\cos(2x)\cos(4y)\cos(2z)$	l_{12}	0	0	0
$\cos(2x)\cos(2y)\cos(4z)$	l_{12}	0	0	0
$\sin(2x)\cos(2y)$	0	$-h_1$	0	0
$\sin(2x)\cos(2z)$	0	$-h_1$	0	0
$\cos(2x)\sin(2y)$	0	0	h_1	0
$\cos(2x)\sin(2z)$	0	0	0	h_1
...	0	....	....	....
...	0	....	....	....
...	0	....	....	....

TABLE 3 -- Expressions for g_1, g_2, g_3, h_1 and the l's

	g_1	g_2	g_3	h_1	l_1	l_2	l_3	l_4	l_5	l_6	l_7	l_8	l_9	l_{10}	l_{11}	l_{12}
e^{-3T}	$\frac{-3}{2816}$	0	0	0	0	0	0	0	0	0	0	0	0	0	0	0
e^{-6T}	0	0	0	$\frac{-3}{2048}$	$\frac{1}{256}$	$\frac{1}{1024}$	$\frac{-1}{512}$	$\frac{-1}{2048}$	0	0	0	0	0	0	0	0
e^{-8T}	0	0	0	$\frac{-59}{21504}$	0	0	0	0	0	0	0	0	0	0	0	0
e^{-9T}	$\frac{3}{704}$	$\frac{-3}{64}$	$\frac{-57}{3520}$	0	0	0	0	0	0	0	0	0	0	0	0	0
e^{-11T}	$\frac{-9}{2816}$	$\frac{3}{64}$	$\frac{57}{2816}$	0	0	0	0	0	0	0	0	0	0	0	0	0
Te^{-11T}	0	$\frac{3}{32}$	0	0	0	0	0	0	0	0	0	0	0	0	0	0
e^{-12T}	0	0	0	$\frac{243}{5120}$	$\frac{23}{352}$	$\frac{-35}{2816}$	$\frac{13}{512}$	$\frac{47}{5632}$	$\frac{-15}{176}$	$\frac{555}{5632}$	$\frac{3}{11264}$	$\frac{-381}{84480}$	$\frac{-51}{3520}$	$\frac{27}{2816}$	$\frac{-3}{1600}$	$\frac{57}{16896}$
e^{-14T}	0	0	0	$\frac{-133}{3072}$	$\frac{-195}{2816}$	$\frac{129}{11264}$	$\frac{-21}{512}$	$\frac{-177}{22528}$	$\frac{15}{176}$	$\frac{-327}{2816}$	$\frac{-51}{5632}$	$\frac{-9}{4224}$	$\frac{849}{56320}$	$\frac{-27}{2816}$	$\frac{3}{1280}$	$\frac{-261}{67584}$
Te^{-14T}	0	0	0	$\frac{-17}{256}$	$\frac{-57}{352}$	$\frac{3}{176}$	0	$\frac{-9}{704}$	$\frac{15}{88}$	$\frac{-57}{352}$	$\frac{3}{176}$	$\frac{57}{2112}$	$\frac{171}{7040}$	$\frac{-27}{1408}$	0	$\frac{-1}{352}$
e^{-16T}	0	0	0	0	0	0	$\frac{9}{512}$	0	0	$\frac{9}{512}$	$\frac{9}{1024}$	$\frac{9}{1536}$	0	0	0	0
e^{-19T}	0	0	$\frac{-57}{14080}$	0	0	0	0	0	0	0	0	0	0	0	0	0
e^{-22T}	0	0	0	$\frac{3}{71680}$	0	0	0	0	0	0	0	$\frac{3}{3840}$	$\frac{-3}{5120}$	0	$\frac{-3}{6400}$	$\frac{1}{2048}$

We see that when u_x is expressed as a triple Fourier series the coefficients of the various terms are expressible as series of ascending powers of Re multiplied by functions of T , the coefficient of cos x sin y sin z being an even series commencing with the zeroth power of Re , that of $\sin(2x) \cos(2z)$ and $\sin(2x) \cos(2y)$ being an odd series commencing with a term in Re , those of

$$\cos(3x) \sin(y) \sin(z) \ , \ \cos(x) \sin(3y) \sin(z) \ , \ \cos(x) \sin(y) \sin(3z) \ ,$$
$$\cos(3x) \sin(3y) \sin(z) \ , \ \cos(3x) \sin(y) \sin(3z)$$

being even series commencing with terms in Re^2 , and so on. Similar results hold for u_y and u_z . (See equations (4.19), (4.27), (4.29), (4.30) and Tables 1-3.) Hence, going back to the "prime" notation and equations (4.13), if we write

$$q^2 = u_x^2 + u_y^2 + u_z^2 \ , \ q'^2 = u_x'^2 + u_y'^2 + u_z'^2 = q^2/A^2 \ ,$$

$$\omega^2 = \omega_x^2 + \omega_y^2 + \omega_z^2 \ , \ \omega'^2 = \omega_x'^2 + \omega_y'^2 + \omega_z'^2 = \omega^2/a^2A^2 \ ,$$

(4.32)

and denote by $\overline{q'^2}$ and $\overline{\omega'^2}$ the space-average values of q'^2 and ω'^2 taken throughout a periodicity cube, it follows from the orthogonal property of the terms in the triple Fourier series that $\overline{q'^2}$ and $\overline{\omega'^2}$ will be expressible as even power series in Re and can be obtained correct to the term in Re^4 if in u_x' the coefficient of $\cos(x') \sin(y') \sin(z')$ is found to Re^4 , that of $\sin(2x') \cos(2z')$ and $\sin(2x') \cos(2y')$ to Re^3 , and the remaining coefficients to Re^2 , with corresponding results for u_y' and u_z' . Hence to find $\overline{q'^2}$ and $\overline{\omega'^2}$ as far as the term in Re^4 it remains only to find the coefficients of $\sin(x') \cos(y') \sin(z')$ in u'_{y4} . Further, of all

67

the terms in $\vec{u}_3^{\,\prime}$ only those in h_1 are required in finding $\overline{q'^2}$ and $\overline{w'^2}$ to Re^4 : the remaining terms in $\vec{u}_3^{\,\prime}$ (the dotted lines in Table 2) affect only the terms in Re^6 in $\overline{q'^2}$ and $\overline{w'^2}$, and need not to be found if we are finding $\overline{q'^2}$ and $\overline{w'^2}$ only up to Re^4 .

In the same way when p' is expressed as a triple Fourier series, $\cos(2x')$, $\cos(2y')$, $\cos(2z')$, $\cos(2x')\cos(2y')$, $\cos(2x')\cos(2z')$, $\cos(2y')\cos(2z')$ occur with coefficients which are even power series in Re beginning with the zeroth power of Re , $\sin(3x')\sin(y')\sin(z')$, $\sin(x')\sin(y')\sin(3z')$, $\sin(x')\sin(3y')\sin(z')$ with coefficients which are odd power series in Re beginning with terms in Re , and so on, as can be seen from equation (4.25) and Tables 1-3. Hence the average values of the pressure and of the pressure-gradient are expressible as even power series in Re , with coefficients which are functions of T , and from equation (4.25) and Tables 1-3 the constant and the Re^2 term can be found. No terms in $\sin(x')\sin(y')\sin(z')$ have been found to occur in p_3' . No further calculations of the expressions for p' have, however, been carried out, so the average values of the pressure and the pressure gradient could be found only as far as the term in Re^2 .

The coefficient of $\sin(x')\cos(y')\sin(z')$ in u_{y4}' was found to be k_1 , where

$$k_1 = \frac{-5315\,e^{-3T}}{141295616} + \frac{3\,e^{-9T}}{16384} + \frac{173\,e^{-11T}}{1376256} - \frac{991\,e^{-15T}}{450560} + \frac{55163\,e^{-17T}}{26492928}$$

$$+ \frac{401\,T\,e^{-17T}}{157696} - \frac{441\,e^{-19T}}{2883584} - \frac{27\,T\,e^{-19T}}{180224} - \frac{3\,e^{-25T}}{3153920} \qquad (4.33)$$

The expressions for $\vec{u}'$ required to calculate $\overline{q'^2}$ and $\overline{w'^2}$ to

the terms in Re^4 are therefore (see equations (4.19), (4.20), (4.21), (4.27), (4.29), (4.30) and Tables 1-3)

$$u'_x = \left(2e^{-3T} + \frac{22}{3} g_1 Re^2 - 2 k_1 Re^4\right) \cos(x') \sin(y') \sin(z')$$

$$+ \left(f_1 Re - h_1 Re^3\right)\left(\cos(2y') + \cos(2z')\right) \sin(2x')$$

$$+ \frac{38}{11} g_2 Re^2 \cos(3x') \sin(y') \sin(z')$$

$$- \frac{23}{11} g_2 Re^2 \left(\sin(3y') \sin(z') + \sin(y') \sin(3z')\right) \cos(x')$$

$$- \frac{11}{19} g_3 Re^2 \left(\sin(3y') \sin(z') + \sin(y') \sin(3z')\right) \cos(3x') ,$$

$$u'_y = \left(- e^{-3T} - \frac{11}{3} g_1 Re^2 + k_1 Re^4\right) \sin(x') \cos(y') \sin(z')$$

$$+ \left(- f_1 Re + h_1 Re^3\right) \cos(2x') \sin(2y')$$

$$- \frac{57}{11} g_2 Re^2 \sin(3x') \cos(y') \sin(z')$$

$$+ \frac{8}{11} g_2 Re^2 \sin(x') \cos(3y') \sin(z')$$

$$- \frac{1}{11} g_2 Re^2 \sin(x') \cos(y') \sin(3z')$$

$$+ \frac{11}{19} g_3 Re^2 \sin(3x') \cos(3y') \sin(z')$$

$$u'_z = \left(- e^{-3T} - \frac{11}{3} g_1 Re^2 + k_1 Re^4\right) \sin(x') \sin(y') \cos(z')$$

$$+ \left(- f_1 Re + h_1 Re^3\right) \cos(2x') \sin(2z')$$

$$- \frac{57}{11} g_2 Re^2 \sin(3x') \sin(y') \cos(z')$$

$$+ \frac{8}{11} g_2 \ Re^2 \ \sin(x') \ \sin(y') \ \cos(3z')$$

$$- \frac{1}{11} g_2 \ Re^2 \ \sin(x') \ \sin(3y') \ \cos(z')$$

$$+ \frac{11}{19} g_3 \ Re^2 \ \sin(3x') \ \sin(y') \ \cos(3z') \ . \tag{4.34}$$

Hence

$$\overline{q'^2} = \frac{6}{8} \left(e^{-3T} + \frac{11}{3} g_1 \ Re^2 - k_1 \ Re^4 \right)^2 + \left(f_1 \ Re - h_1 \ Re^3 \right)^2$$

$$+ \frac{1}{4} \ Re^4 \left(\frac{415}{11} g_2^2 + \frac{242}{361} g_3^2 \right) + \ . \ . \ . \ .$$

$$= \frac{3}{4} \left(e^{-6T} + Re^2 \ F_1 + Re^4 \ F_2 + \ . \ . \ . \ . \right) \tag{4.35}$$

where F_1 and F_2 are given in Table 4.

In the same way, if we write down the formulae for $\vec{\omega}'$ corresponding to (4.34) and take the mean value of the sum of the squares, we find that

$$\overline{\omega'^2} = \frac{18}{8} \left(e^{-3T} + \frac{11}{3} g_1 \ Re^2 - k_1 \ Re^4 \right)^2 + 8 \left(f_1 \ Re - h_1 \ Re^3 \right)^2$$

$$+ Re^4 \left(\frac{415}{4} g_2^2 + \frac{121}{38} g_3^2 \right) + \ . \ . \ . \ .$$

$$= \frac{9}{4} \left(e^{-6T} + Re^2 \ G_1 + Re^4 \ G_2 + \ . \ . \ . \ . \right) \tag{4.36}$$

where G_1 and G_2 are given in Table 4.

There is some independent verification of these results since $\overline{q'^2}$ and $\overline{\omega'^2}$ are related. By multiplying the equations of motion in order by u_x, u_y, u_z and adding we obtain the usual equation of energy, which, when average values are taken, becomes

$$\frac{d}{dt} \left(\tfrac{1}{2} \ \rho \ \overline{q^2} \right) = - \overline{w} \tag{4.37}$$

70

TABLE 4

Expressions for F_1, F_2, G_1 and G_2

	F_1	F_2	G_1	G_2
e^{-6T}	$-\dfrac{1}{128}$	$\dfrac{6393}{70647808}$	$-\dfrac{1}{128}$	$\dfrac{6393}{70647808}$
e^{-12T}	$\dfrac{5}{64}$	$-\dfrac{5}{4096}$	$\dfrac{5}{32}$	$-\dfrac{5}{2048}$
e^{-14T}	$-\dfrac{15}{128}$	$-\dfrac{275}{344064}$	$-\dfrac{35}{128}$	$-\dfrac{275}{147456}$
e^{-16T}	$\dfrac{3}{64}$	$\dfrac{59}{43008}$	$\dfrac{1}{8}$	$\dfrac{59}{16128}$
e^{-18T}	0	$\dfrac{5741}{102400}$	0	$\dfrac{17223}{102400}$
e^{-20T}	0	$-\dfrac{435971}{4139520}$	0	$-\dfrac{1620677}{4967424}$
Te^{-20T}	0	$-\dfrac{5867}{39424}$	0	$-\dfrac{29335}{59136}$
e^{-22T}	0	$\dfrac{215465}{4325376}$	0	$\dfrac{2058619}{12976128}$
Te^{-22T}	0	$\dfrac{12979}{90112}$	0	$\dfrac{132809}{270336}$
$T^2 e^{-22T}$	0	$\dfrac{1245}{11264}$	0	$\dfrac{415}{1024}$
e^{-28T}	0	$\dfrac{411}{7884800}$	0	$\dfrac{137}{563200}$
e^{-30T}	0	$-\dfrac{33}{573440}$	0	$-\dfrac{33}{114688}$
e^{-38T}	0	$\dfrac{3}{819200}$	0	$\dfrac{19}{819200}$

71

where

$$\frac{W}{\mu} = 2\left[\left(\frac{\partial u_x}{\partial x}\right)^2 + \left(\frac{\partial u_y}{\partial y}\right)^2 + \left(\frac{\partial u_z}{\partial z}\right)^2\right] + \left(\frac{\partial u_z}{\partial y} + \frac{\partial u_y}{\partial z}\right)^2$$

$$+ \left(\frac{\partial u_x}{\partial z} + \frac{\partial u_z}{\partial x}\right)^2 + \left(\frac{\partial u_y}{\partial x} + \frac{\partial u_x}{\partial y}\right)^2$$

$$= \omega_x^2 + \omega_y^2 + \omega_z^2 - 2\left[\frac{\partial}{\partial x}(u_y\omega_z - u_z\omega_y) + \frac{\partial}{\partial y}(u_z\omega_x - u_x\omega_z)\right.$$

$$\left. + \frac{\partial}{\partial z}(u_x\omega_y - u_y\omega_x)\right] + \nabla^2 q^2 , \tag{4.38}$$

so that

$$\frac{\overline{W}}{\mu} = \overline{\omega^2} , \tag{4.39}$$

and

$$\frac{d}{dt}\left(\tfrac{1}{2}\overline{q^2}\right) = -\nu\overline{\omega^2} , \tag{4.40}$$

i.e.

$$\frac{d}{dt'}\left(\tfrac{1}{2}\overline{q'^2}\right) = -\frac{\overline{\omega'^2}}{Re} \tag{4.41}$$

Hence

$$\frac{d}{dT}\left(\tfrac{1}{2}\overline{q'^2}\right) = -\overline{\omega'^2} \tag{4.42}$$

From (4.35) and (4.36) it follows that the F and G are connected by the relations

$$G_1 = -\frac{1}{6}\frac{dF_1}{dT} , \quad G_2 = -\frac{1}{6}\frac{dF_2}{dT} , \tag{4.43}$$

which are seen from Table 4 to be satisfied.

Our formulae include those that could be obtained by developing in powers of the time t . The trick is to replace the exponentials in our formulae by their expansions in T and then use (4.20) to get the per-

72

turbation solutions in powers of t . Notice that finite order trunca-
tions of (4.35) or (4.36) do not have the singular behavior exhibited
by truncations of a series in powers of t as $t \to \infty$. However,
examination of the displayed terms of (4.35) or (4.36) suggests that
for $t/Re \geqslant 1$, perturbation series in powers of Re may diverge for
$Re \geqslant 12$.

Neither perturbation series in powers of t nor Re can describe
the evolution of the flow field for large t or Re . In addition to
the fundamental fluid dynamical interest in the development of the
Taylor-Green vortex, the flow is a most convenient one on which to
debug and perform tests of our vortex-in-cell (VIC) method. For these
purposes, we compared our results with the ones obtained from a program
developed by Rogallo[55] for the simulation of homogeneous incompressible
turbulence. In Rogallo's algorithm, the velocity field is represented
spatially by a truncated triple Fourier series (spectral method) and
followed in time using a fourth-order Runge-Kutta scheme. Notice that
for the Taylor-Green vortex, the results from this spectral method are
infinite-order accurate, i.e. errors go to zero faster than any finite
power of $1/k_{max}$ as $k_{max} \to \infty$, in contrast to the finite order accur-
acy of difference schemes[56]. Since there are no experimental results
of the Taylor-Green system to compare with and the perturbation analysis
being woefully inadequate to describe either the large t or the large
Re behavior, the spectral method provides the best results to compare
with.

The Taylor-Green system is one of continuous vorticity (eq. 4.10),
and it is important to represent such a continuum by a sufficient number
of discrete vortex filaments. These are given by eq. 4.11. Assuming

73

our computational box in the range $[-\pi, \pi]$ in each dimension, Figure 26 shows the initial discretized vortex filaments. Each filament having effectively a gaussian core, they were distributed in such a fashion as to fill the space up equally. To assign the proper circulation Γ to each of them, let's consider eq. 4.10 at $z' = \pm \pi/2$ (i.e. $z = \pi/2a$) which implies $\omega'_x = \omega'_y = 0$ and $\omega'_z = -3\cos(x')\cos(y')$. Using eq. 2.6, we obtain

$$\Gamma = -3\iint_A \cos(x')\cos(y')\,dx'\,dy'$$

where the surface A is taken to be a square centered at each filament. This gives us a range of circulation values identical for all octants of our space except for their sign alternating from one octant to another. Figure 24 and 25 display that feature.

These initial conditions being set in our code, we let the program run and made up a movie tracing the vortex lines in the three dimensions. Figure 27 shows four stills of that movie. The movie was taken from a 16x16x16 computational box with the vorticity field represented by 144 vortex filaments, each broken into an average of 24 nodes. The limitation in the total number of nodes is owing to the 3-D graphic system that can only display about 3700 three-dimensional points per frame. Also, the graphics package draws straight lines between nodes whereas throughout the computations sharp corners were eliminated by smoothing and quadratic spline interpolation. The movie showed that the vortex filaments themselves do not remain planar and that there is a considerable tendency towards disordering, convoluting and stretching. However, it was observed that the symmetry of the initial conditions in the y- and z-directions is generally preserved throughout the entire calculation except for
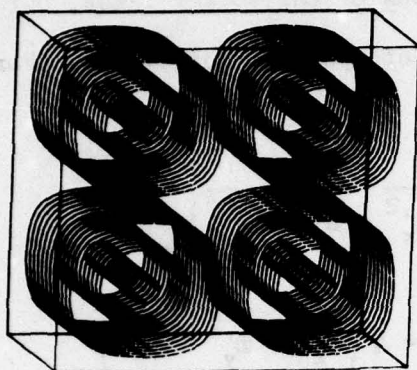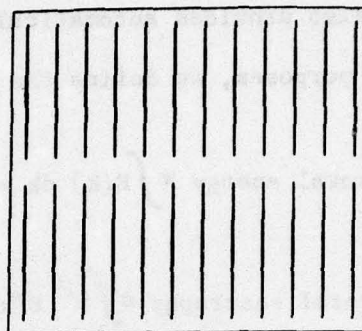
Tilted (y-z)-plane at t = 0 .   (x-z)-plane at t = 0 .

Figure 27. Taylor-Green system. 144 vortex filaments made of 3456 nodes
in a 16x16x16 mesh.
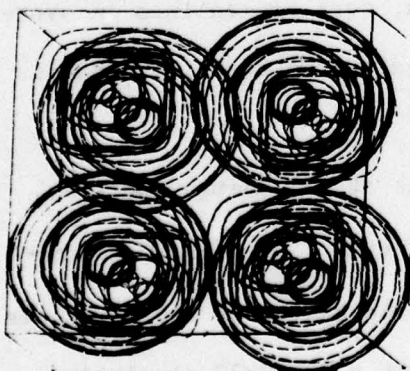
Tilted (y-z)-plane at t = 0.6 .   (x-y)-plane at t = 1.8 .
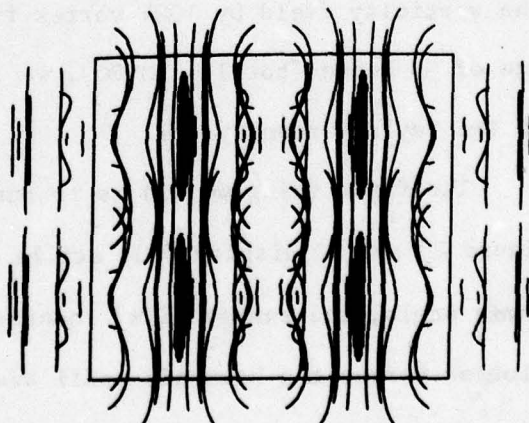
minor discrepancies which occur when the instabilities make the flow erratic.

Besides being able to follow the motions of the vortex lines, our code also provides automatically all kinds of spectral quantities. For later purposes, we define the following:

$$\text{total energy} \equiv \int E(k)\ dk = \tfrac{1}{2}\ \overline{q'^2} = \tfrac{1}{2}\left(\overline{u_x'^2} + \overline{u_y'^2} + \overline{u_z'^2}\right)$$

$$\text{total enstrophy} \equiv \int k^2\ E(k)\ dk = \tfrac{1}{2}\ \overline{\omega'^2} = \tfrac{1}{2}\left(\overline{\omega_x'^2} + \overline{\omega_y'^2} + \overline{\omega_z'^2}\right)$$

$$\text{streamwise component of total energy} \equiv \int E_x(k)\ dk = \tfrac{1}{2}\ \overline{u_x'^2}$$

$$\text{cross-flow component of total energy} \equiv \int E_y(k)\ dk = \tfrac{1}{2}\ \overline{u_y'^2}$$

$$\text{spanwise component of total energy} \equiv \int E_z(k)\ dk = \tfrac{1}{2}\ \overline{u_z'^2}$$

After rescaling our problem to a 32×32×32 simulation and representing the vorticity field by 1024 vortex filaments, each broken into an average of 30 nodes (total = 30720), we investigated the spectral dynamics of the Taylor-Green system.

The first thing we did is to run a movie of the energy spectrum. Figure 28 and 29 display four stills of that movie. On a semi-logarithmic scale, the energy $E(k)$ contained in the shells of radius k is plotted versus the harmonic radii available in a 32×32×32 simulation. The upper right corner displays the running time and the total enstrophy.

The seven next figures (Figures 30 to 36) display the energy contained in the seven lowest modes as time goes. Our vortex-in-cell (VIC) results are compared with the ones given by the 32×32×32 spectral

76
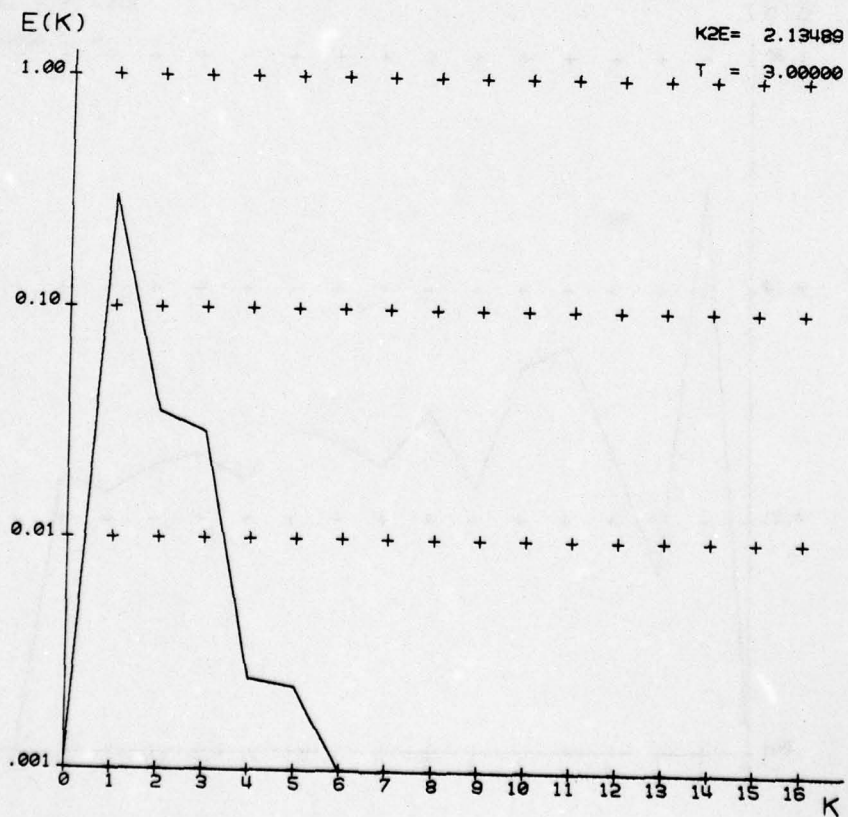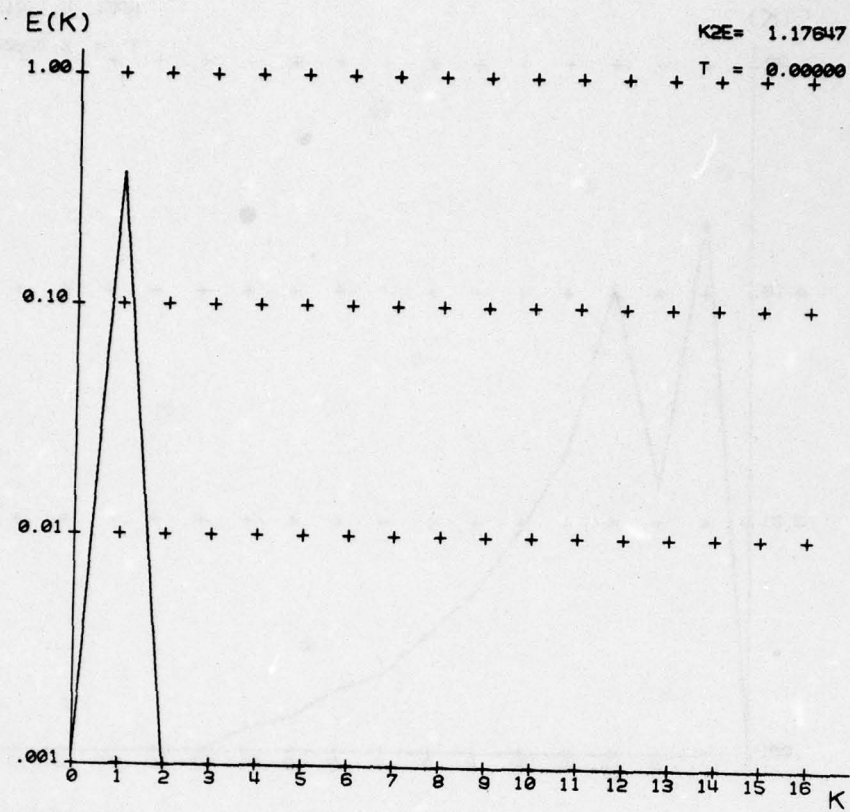
Figure 28. Energy spectrum in shells of radius k . 1024 vortex filaments made of 30720 nodes in a 32×32×32 mesh.
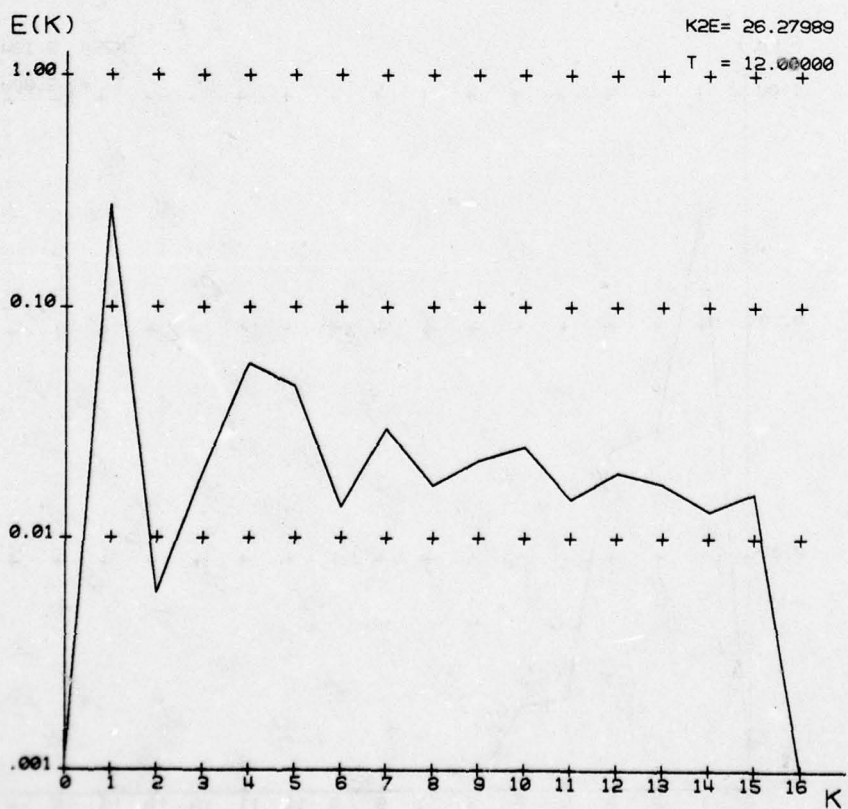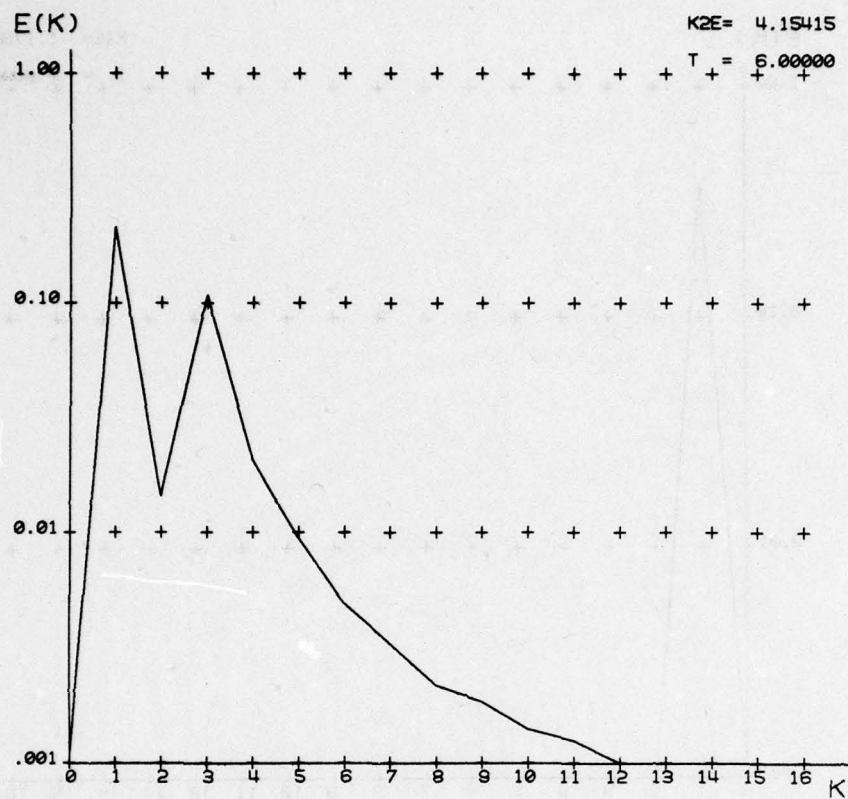
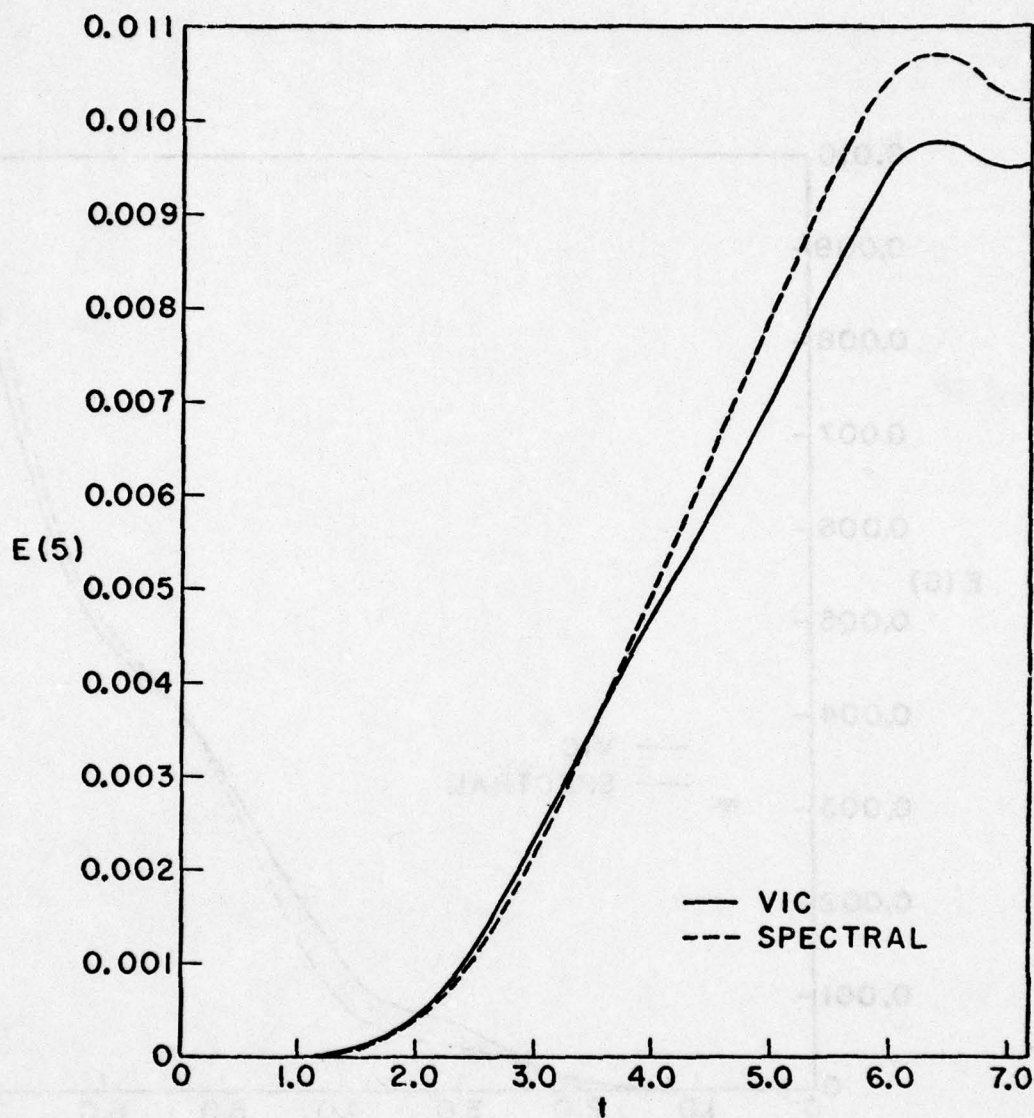Figure 29. Continuation of Figure 28.

78
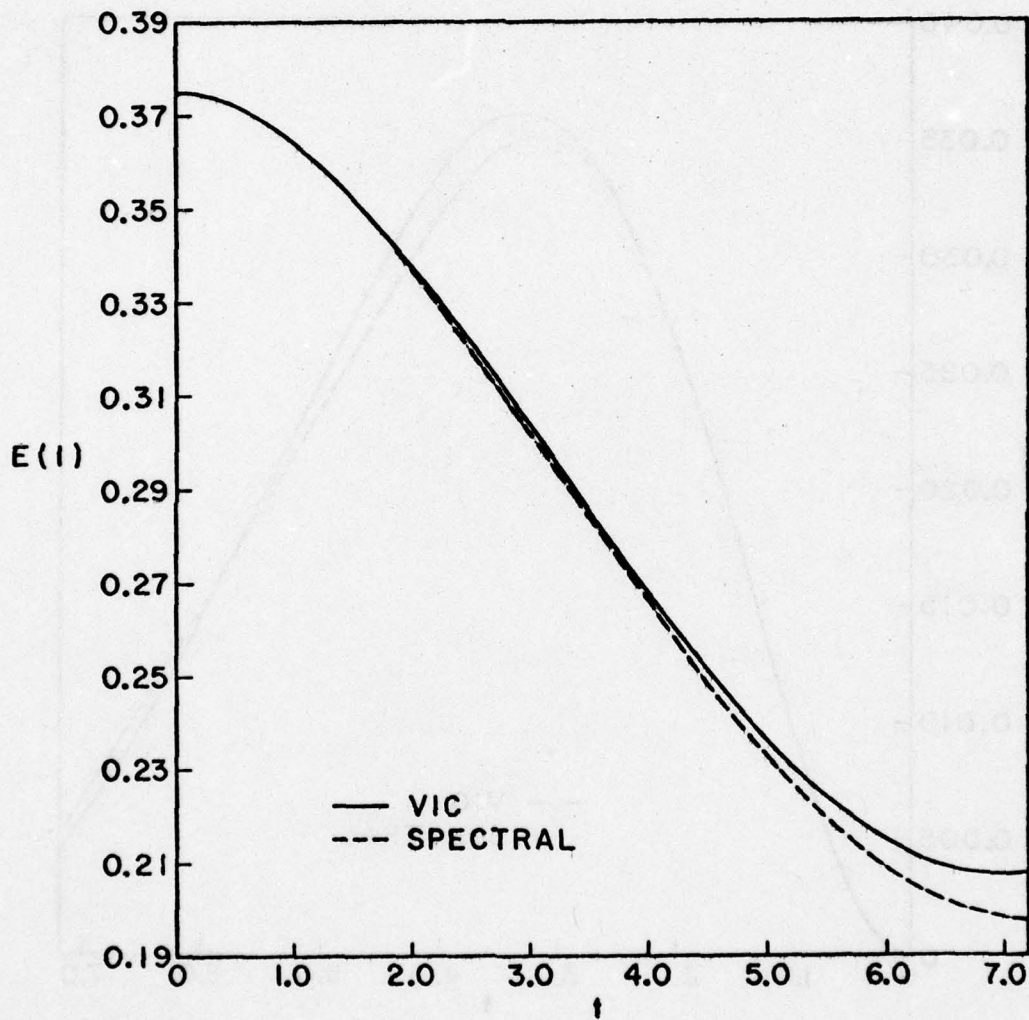
Figure 30. Energy in the first harmonic versus time. Vortex-in-Cell (VIC) method compared with spectral method. 32×32×32 mesh.
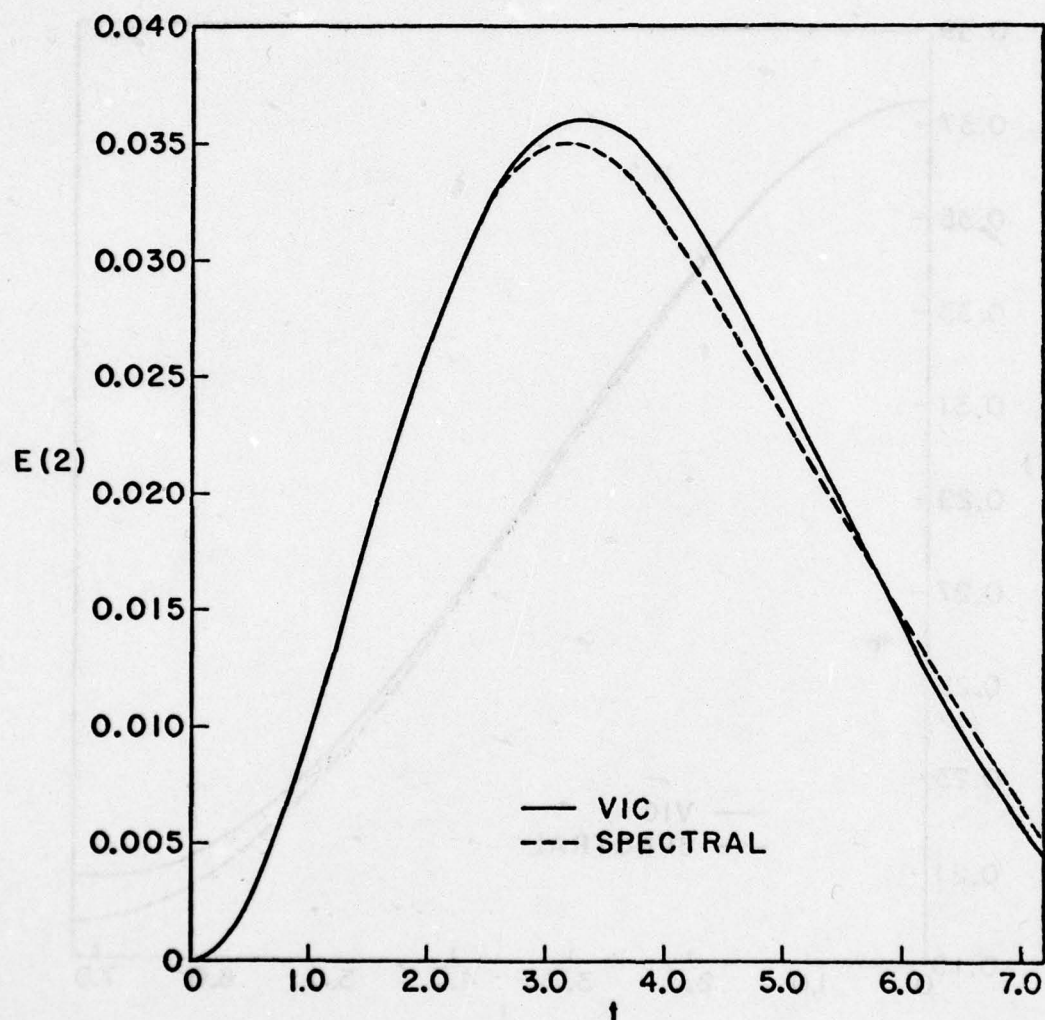
Figure 31. Energy in the second harmonic versus time. Vortex-in-Cell (VIC) method compared with spectral method. 32×32×32 mesh.
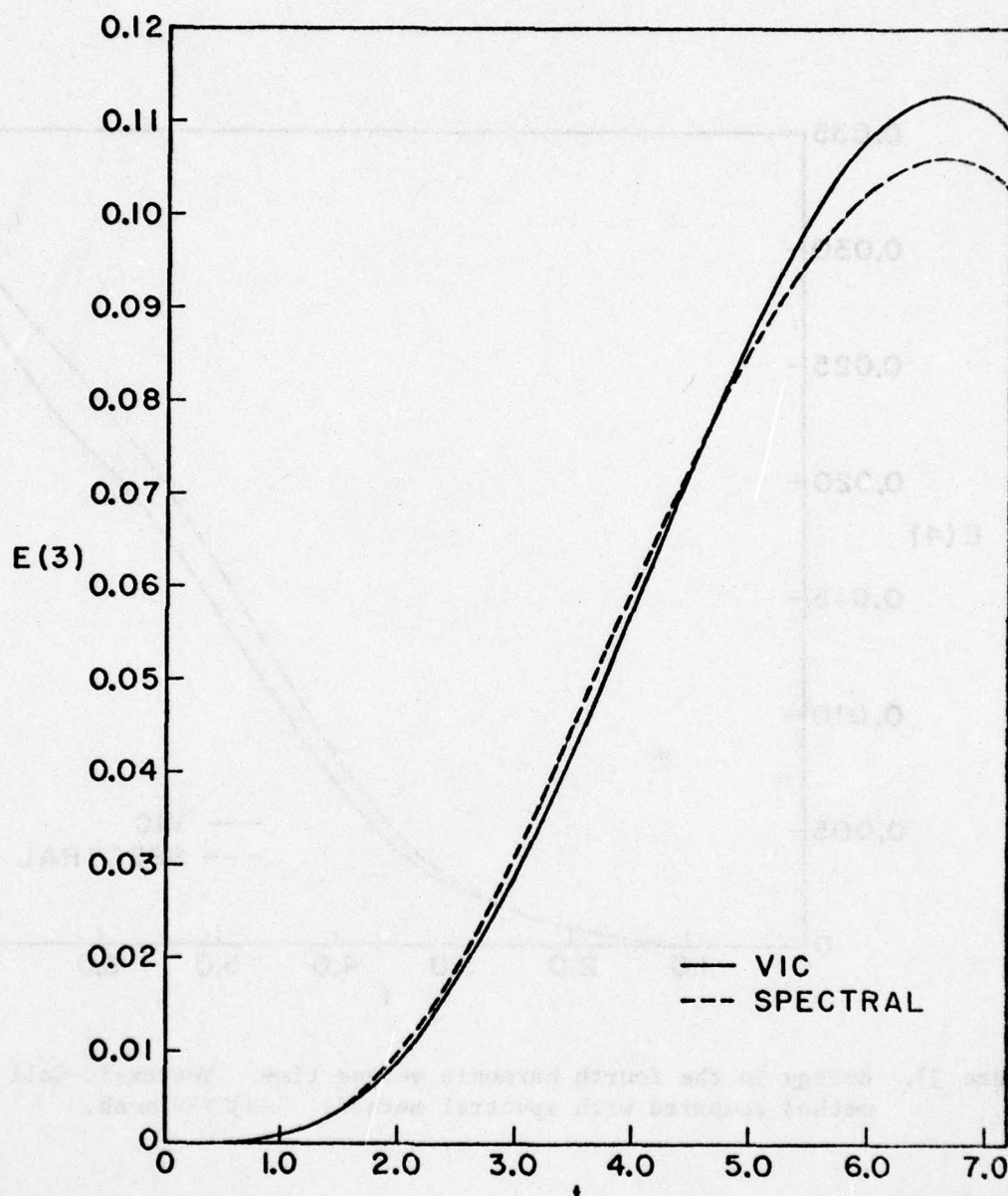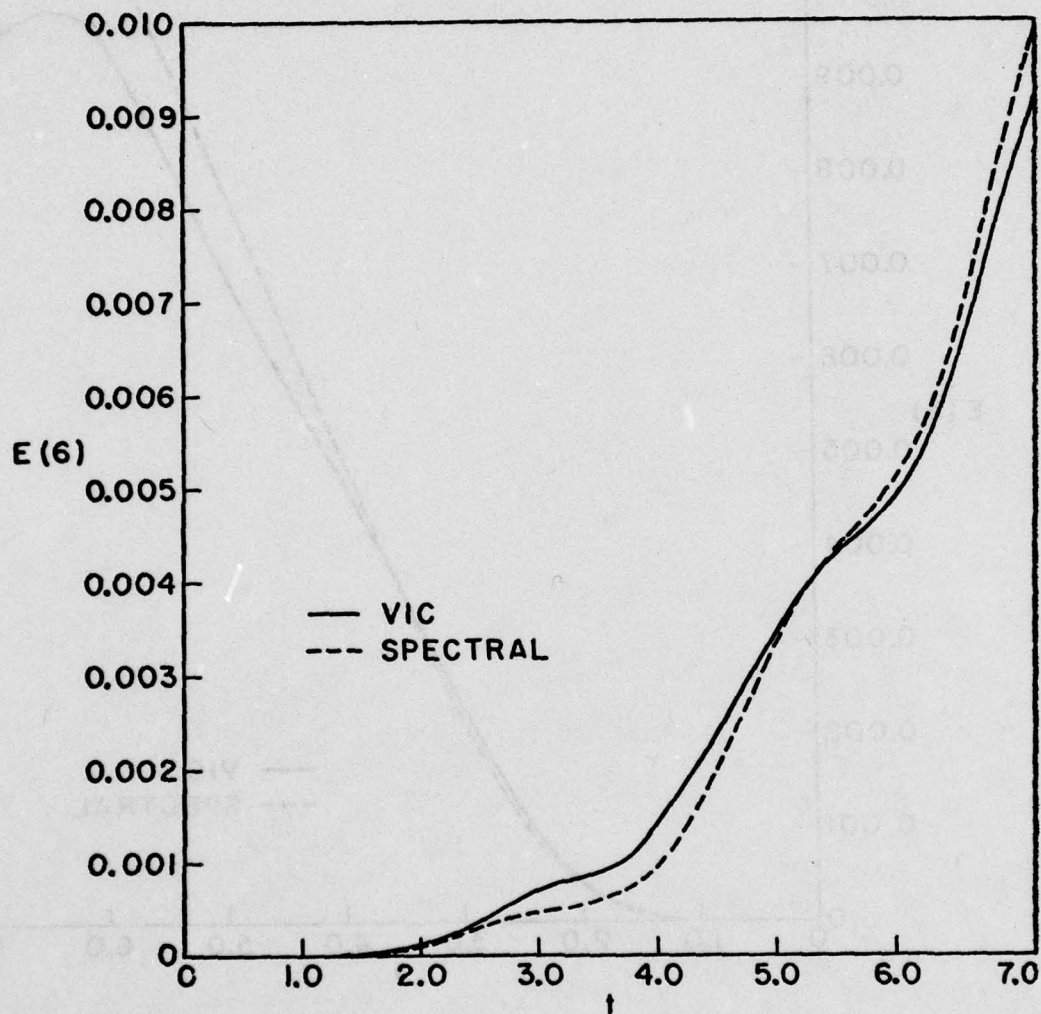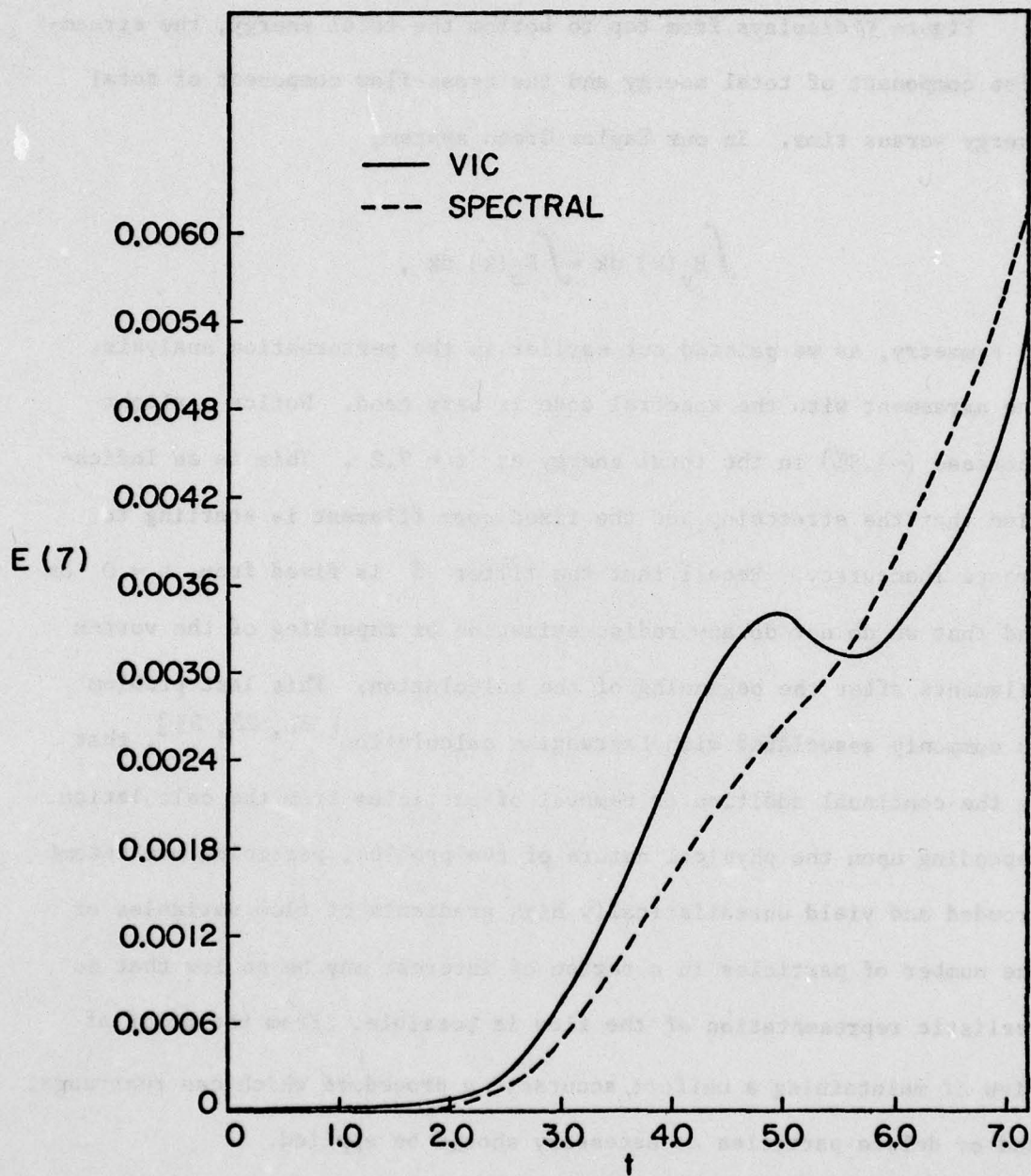
Figure 32. Energy in the third harmonic versus time. Vortex-in-Cell (VIC) method compared with spectral method. 32×32×32 mesh.
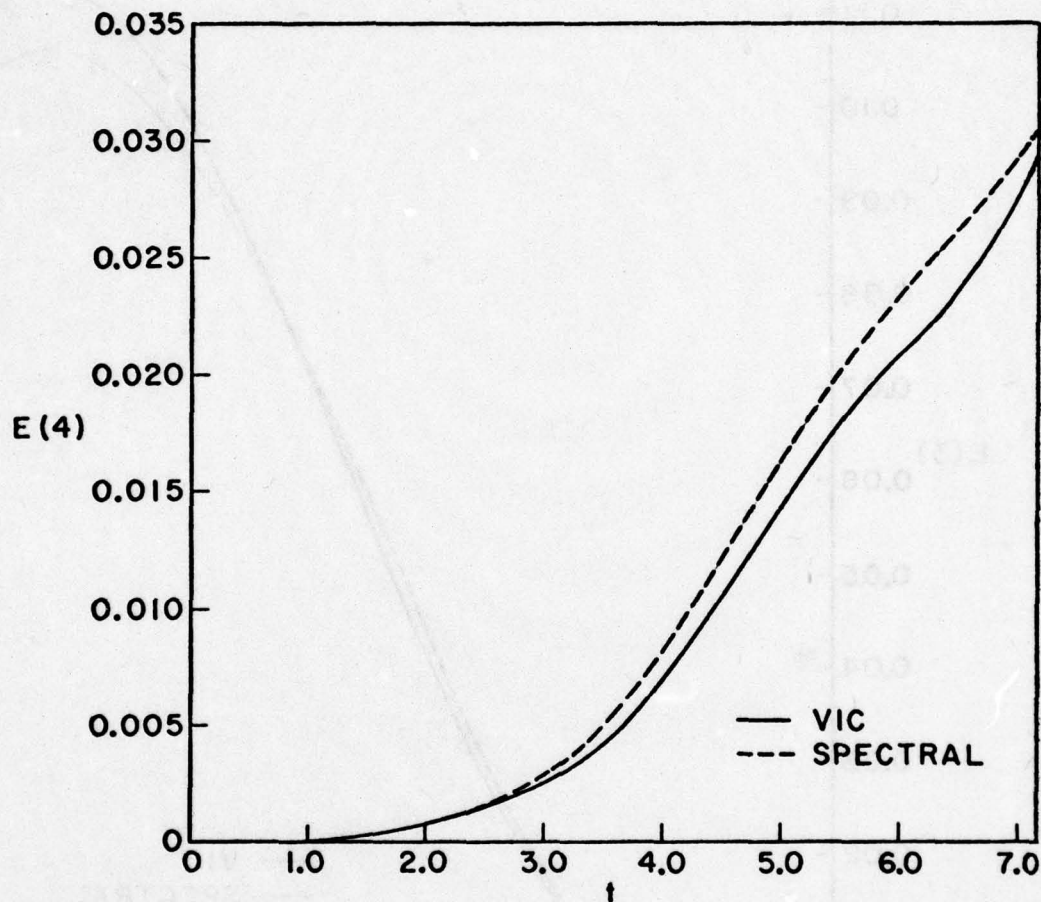
Figure 33. Energy in the fourth harmonic versus time. Vortex-in-Cell (VIC) method compared with spectral method. 32×32×32 mesh.

Figure 34. Energy in the fifth harmonic versus time. Vortex-in-Cell (VIC) method compared with spectral method. 32×32×32 mesh.

Figure 35. Energy in the sixth harmonic versus time. Vortex-in-Cell (VIC) method compared with spectral method. 32×32×32 mesh.

VIC

--- SPECTRAL

0.0060

0.0054

0.0048

0.0042

0.0036

E (7)

0.0030

0.0024

0.0018

0.0012

0.0006

0

0   1.0   2.0   3.0   4.0   5.0   6.0   7.0

t

Figure 36. Energy in the seventh harmonic versus time. Vortex-in-Cell (VIC)
method compared with spectral method. 32×32×32 mesh.

simulation where $\nu = 0$. Our filter $\hat{G}$ was chosen as to fit best the spectral results at $t = 0$ and was left fixed thereafter. The agreement is excellent, specially for early times.

Figure 37 displays from top to bottom the total energy, the streamwise component of total energy and the cross-flow component of total energy versus time. In our Taylor-Green system,

$$\int E_y(k)\ dk = \int E_z(k)\ dk\ ,$$

by symmetry, as we pointed out earlier in the perturbation analysis. The agreement with the spectral code is very good. Notice a slight increase ($\sim 3.5\%$) in the total energy at $t = 7.2$. This is an indication that the stretching and the fixed core filament is starting to create inaccuracy. Recall that the filter $\hat{G}$ is fixed from $t = 0$ on and that we do not do any rediscretization or repacking of the vortex filaments after the beginning of the calculation. This last problem is commonly associated with Lagrangian calculation[21, 22, 23], that is the continual addition or removal of particles from the calculation. Depending upon the physical nature of the problem, particles may become crowded and yield unrealistically high gradients of flow variables or the number of particles in a region of interest may be so low that no realistic representation of the flow is possible. From the point of view of maintaining a uniform accuracy, a procedure which can rearrange, add or delete particles as necessary should be applied.

Finally, Figure 38 shows, on a semi-logarithmic scale the total enstrophy versus time for a longer time span. The agreement with Rogallo's results is again very good until the already mentioned problems come up. On the same figure, we also plotted the total enstrophy versus time when

86
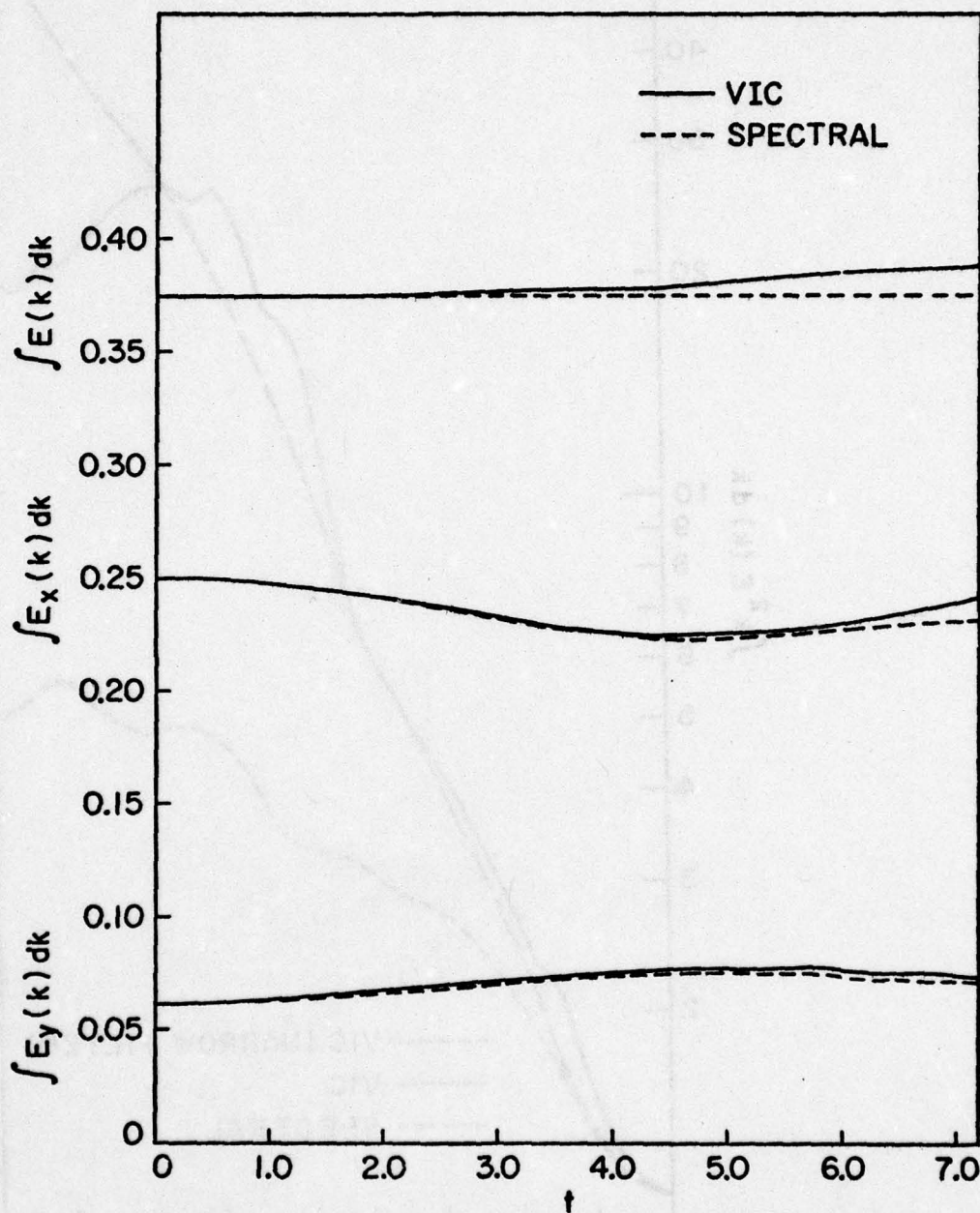
Figure 37. Total energy, x-component and y-component of total energy versus time. Vortex-in-Cell (VIC) method compared with spectral method. 32×32×32 mesh.
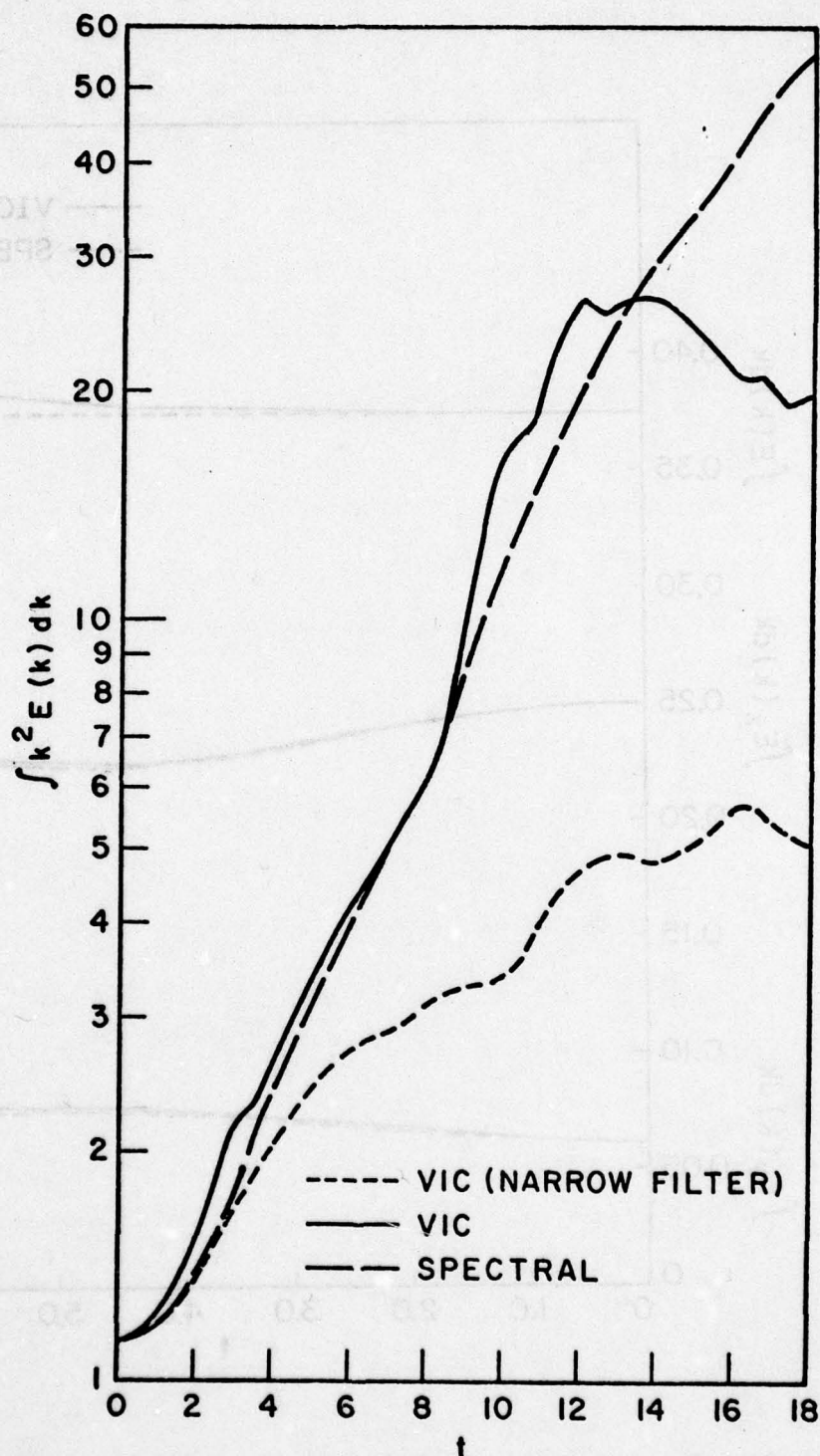
Figure 38. Enstrophy versus time. Vortex-in-Cell (VIC) method compared with spectral method. 32×32×32 mesh.

we initially set an arbitrarily narrower filter $\hat{G}$ for the entire cal-culation. This was like broadening the vortex profiles or making the flow more viscous.

In conclusion, it is clear that a perturbation analysis of the Taylor-Green system does not display much interesting features of the flow pattern for medium or large t or Re. However, our vortex-in-cell method gives very good agreement with a purely spectral decomposi-tion of the flow. The use of the filter $\hat{G}$ provides damping of the high wavenumber components of the vorticity field, damping that would otherwise occur through subgrid scale dissipation[28] or by viscous dissipation[19]. The nature of the dissipation provided by G is not well established at this time. However, based on comparisons with spectral calculations, we can make the following observations. Invis-cid simulations of three-dimensional motions which have no scales smaller than the grid spacing Δ are accurately simulated with no energy loss by the present method using a broad filter $\hat{G}$. However, as the energy cascades to scales smaller than Δ, some dissipative effects must be provided. The application of the gaussian filter $\hat{G}$ provides energy dissipation for the Taylor-Green problem, where such a cascade exists. As a final observation, we pointed out that a reseeding procedure should be incorporated in our code to guarantee numerical stability at later times in the calculations.

89

IV.3 Shear Layer

In many flows of practical interest, there are interactions between irrotational regions and rotational turbulent regions. As an example of such a flow, we chose to simulate the mixing layer. In a mixing layer, at high Reynolds number, the regions are separated by a thin interface across which there is essentially a jump in the vorticity parallel to the layer (see Figure 39, showing such jumps at the top and at the bottom of the layer). The usual difficulty in simulating such a flow arises from the fact that such a vorticity jump would be diffused by finite difference methods. Using the vortex-in-cell method, we can retain sharp gradients in vorticity by avoiding difference approximations to the term representing convective transport of vorticity, $\vec{\omega} \cdot \vec{\nabla u}$ (see Eq. 2.2).

Large coherent eddies have been observed in turbulent shear layers[25,26] and seem to play an important role in the mixing. It has been observed[26] that the pairing of large eddies is central to the question of shear-layer development. Since large eddies have such an importance, it is of considerable interest to attempt to model the amalgamation process. In this section, we follow the evolution of the mixing layer disturbed by simple two- and three-dimensional perturbations.

In our coordinate system, as defined in the previous section, the x-direction is the streamwise direction, the y-direction is the cross-flow direction, along which the vorticity jumps are encountered, and the z-direction is the spanwise direction, along which the unperturbed flow is uniform (see Figure 40). Our mesh system is 32×32×32 cells. As said earlier, using fast Fourier transforms to solve the Poisson's equation generates periodic boundary conditions in each of the three directions. Therefore, in order to insure continuity of the velocity field in the
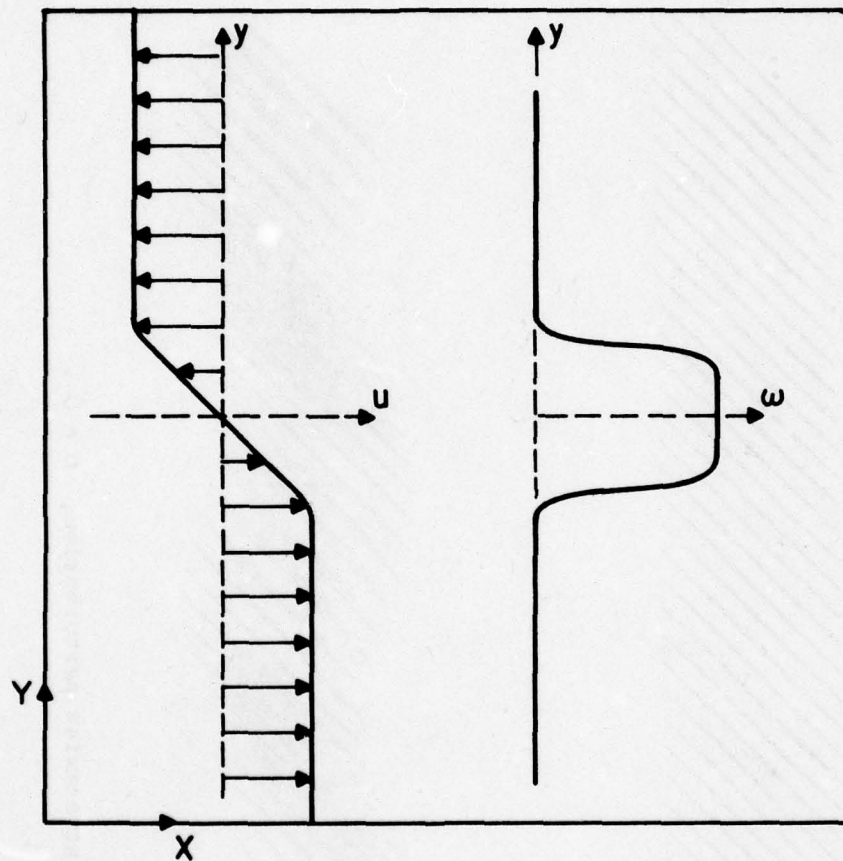
Figure 39. Initial velocity (u) and vorticity (ω) profiles
for a parallel flow with single velocity shear.

Figure 40. Vortex lines for streamwise perturbation, t = 0.

cross-flow direction y , we cannot attempt to study a flow with a
single velocity shear layer. We rather investigate a parallel flow
with two opposite linear velocity shear layers, that is, a flow where
the initial fluid streaming velocity profile is an even function with
respect to the y axis (see Figure 41). The initial vorticity field
consists of two uniform layers of vorticity, infinite in the spanwise
direction z and having opposite vorticity so that their sum equals
zero. In our simulation, these two layers are replaced by arrays of
discrete line vortices divided evenly into two groups and distributed
separately in different parts in space. Those with positive vorticity
are located within a thin layer in the lower half plane (from $y = - 9$
to $y = - 7$) while the others carrying negative vorticity are distri-
buted in the layer at the symmetric position in the upper half plane
(from $y = 7$ to $y = 9$). That is to say y ranges from   -16 to
+16 (Figure 42). This distribution ensures the maximum spacing
between the two layers and their periodic images in the cross-flow
direction y . The results shown in this section were obtained by
initially perturbing only one of the layers so that the effect of the
periodic boundary in the cross-flow direction y can be monitored by
observing subsequent perturbations by the initially undistributed layer.
Each layer is made up of 160 filaments, and each filament resolved into
32 nodes.

As a first case, we choose a streamwise (x) perturbation of the
filaments: $y = y_0 + \sin(\pi x/8)$, x ranging from -16 to +16. The per-
turbation is identical for all z (Figure 40). It means that we in-
troduced a first-harmonic down-stream vorticity variation within the
layer having positive vorticity. This sets a purely two-dimensional
problem where there is no spanwise z dependence for all times. The
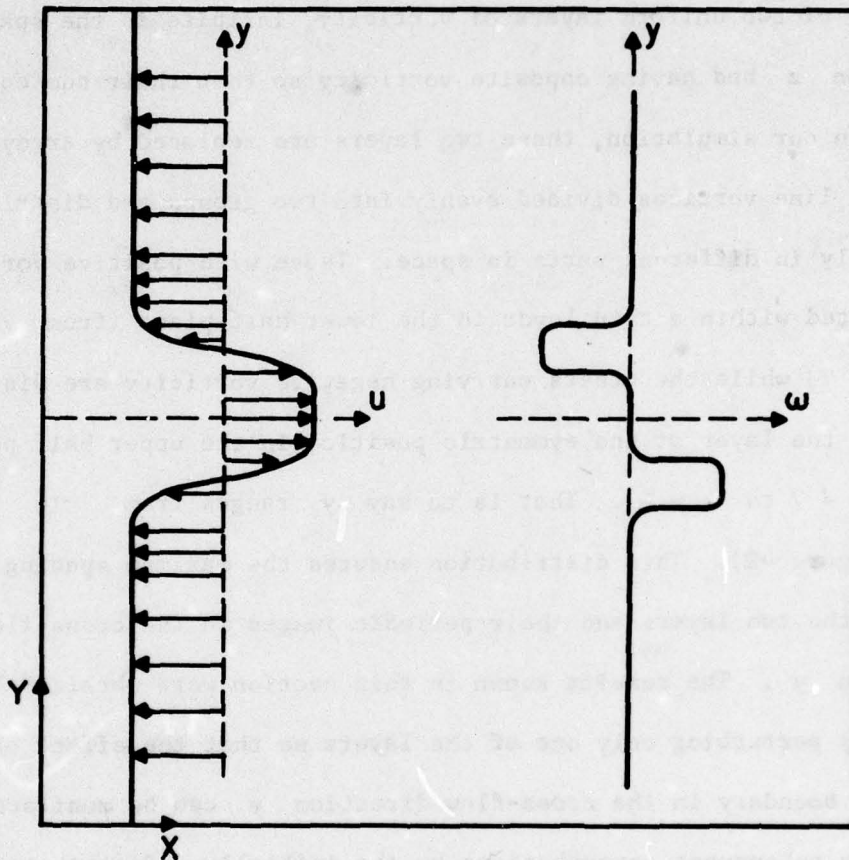
Figure 41. Initial velocity (u) and vorticity (ω) profiles for
a parallel flow with two opposite velocity shears.

z-component of vorticity is the only non-zero component[19]. Figure 40 shows the initial vortex lines. Figures 42 and 43 display stills of the vorticity contours at four instants in time and taken at the center of the computational box, $z = 0$.

In these contour maps and the following ones, the dashed lines stand for negative contours and the solid lines for positive contours; the tiny numbers along the contours indicate the different levels and the small square in the lower right corner of the contours indicate the mesh size. It should be pointed out that the graphics package draws straight lines within the mesh size which explains the lack of smoothness in the contours. On the other hand, recall that our algorithm which governs the temporal evolution of the flow guarantees a higher level of smoothness.

Figures 42 and 43 show the roll-up into two vortices as has been observed by other investigators[14,17,7,57]. This is the phenomenon of amalgamation referred to earlier. Also, the initially unperturbed top layer eventually undergoes the two-dimensional vortex roll disturbances. Notice that the sense of the pairing rotation in the positive layer is opposite to that in the negative layer. No pairing of these vortices further occurs because of the symmetry of the initial disturbance. Notice also that during the initial stages of the rolling-up (up to TIME = 0.9), the initial structure of the rolled-up sheet is still evident. However, once the "eddies" are well formed and begin to rotate, they lose this structure and develop into isolated blobs of vorticity[14]. Contrary to Acton's simulation[14], the two vortex blobs at TIME = 3.6 will not merge into one, due to the symmetrical opposition of the vortices from the negative layer and the fact that we introduced a first-harmonic variation only.

MIN = -2.700E+01   MAX = 2.938E+01

y

x

Z-VORTICITY
TIME =   0.000

MIN = -2.706E+01   MAX = 3.181E+01

y

x

Z-VORTICITY
TIME =   .450

Figure 42. Contours ω_z for streamwise perturbation, z = 0 .

96

MIN = -2.722E+01   MAX = 3.218E+01

Z-VORTICITY
TIME =   .900

MIN = -3.620E+01   MAX = 3.435E+01
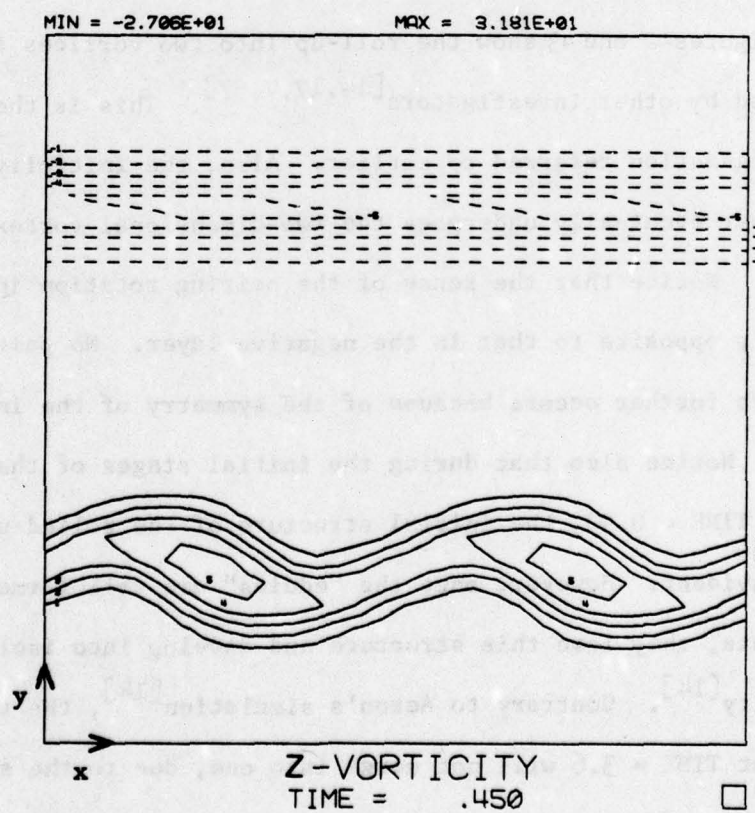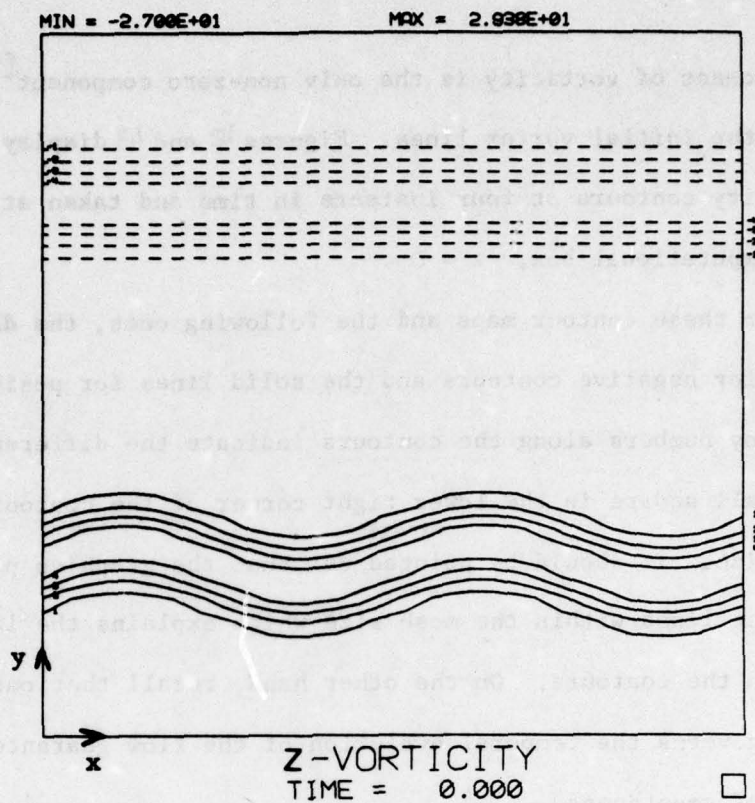
Z-VORTICITY
TIME =   3.600
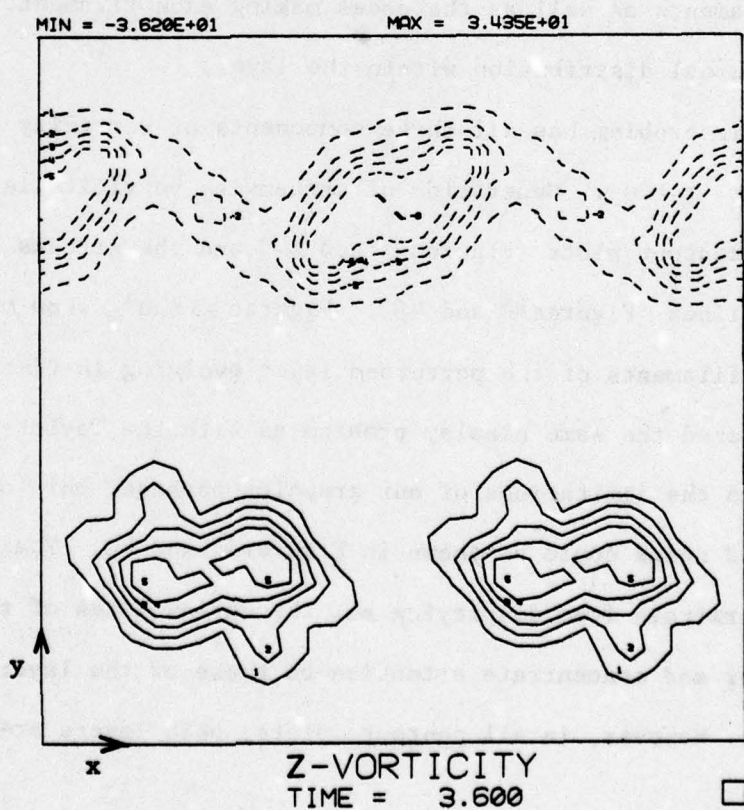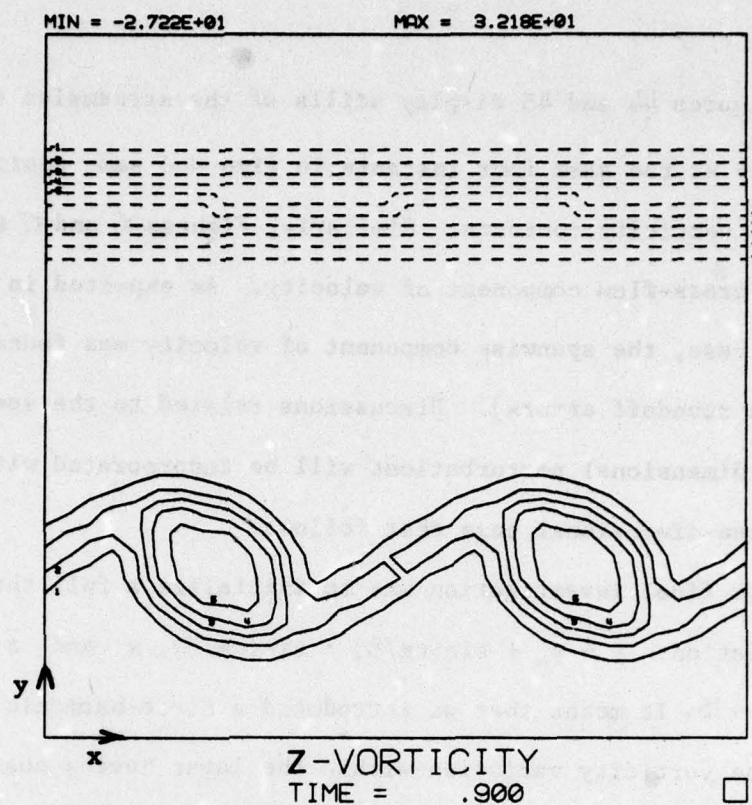
Figure 43. Continuation of Figure 42.

97

Figures 44 and 45 display stills of the streamwise component of

velocity at the same four instants in time and same position in space as

for the vorticity contours. Similarly, Figures 46 and 47 show four stills

of the cross-flow component of velocity. As expected in this two-dimen-

sional case, the spanwise component of velocity was found to be null

(within roundoff errors). Discussions related to the spectral dynamics

of two-dimensional perturbations will be incorporated with the ones on

the three-dimensional case that follows.

Our final investigation was to initialize a full three-dimensional

perturbation: $y = y_0 + \sin(\pi x/8) \cdot \sin(\pi z/8)$, x and z ranging from

-16 to +16. It means that we introduced a first-harmonic streamwise and

spanwise vorticity variation within the layer having positive vorticity;

the filaments as well as the nodes making each filament, both followed

a sinusoidal distribution within the layer.

This problem has all three components of vorticity and velocity pre-

sent for $t > 0$. Generation of streamwise vorticity is observed as shown

by the contour plots (Figures 50 and 51) and the streaks formed by the

vortex lines (Figures 48 and 49). Figures 48 and 49 show two views of the

vortex filaments of the perturbed layer evolving in time. Here we

encountered the same display problem as with the Taylor-Green system;

owing to the limitations of our graphics package, only one-third of the

computed nodes could be shown in Figures 48 and 49. That is the reason

why we refrain from displaying all the vortex lines of the two layers

together and concentrate attention on those of the layer initially dis-

turbed. However, in all <u>contour</u> plots, both layers are displayed to-

gether.

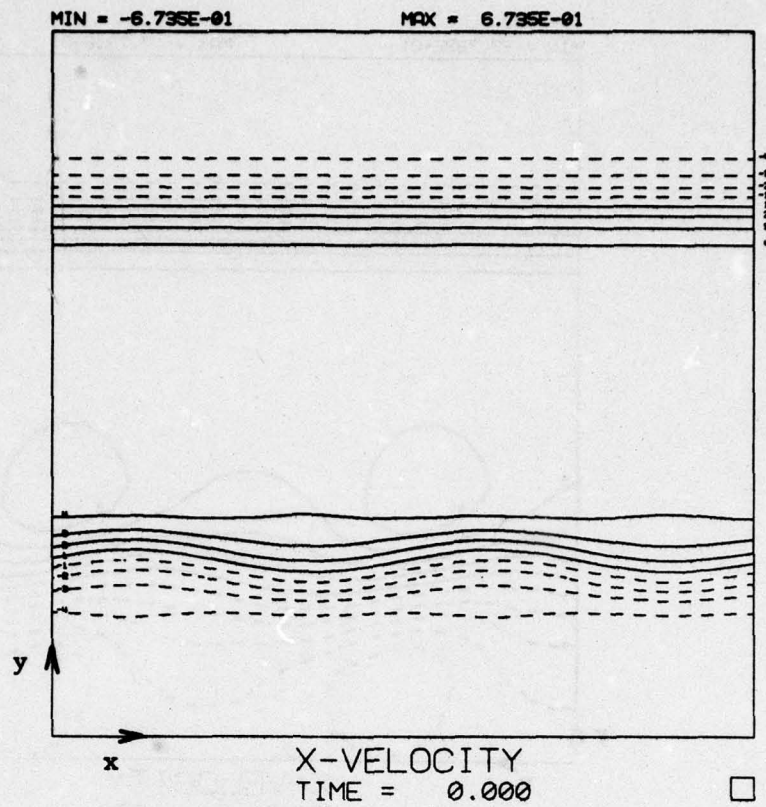Quite early in time, the display of the vortex filaments becomes

MIN = -6.735E-01   MAX = 6.735E-01

X-VELOCITY
TIME =   0.000

MIN = -7.202E-01   MAX = 7.202E-01

X-VELOCITY
TIME =   .450
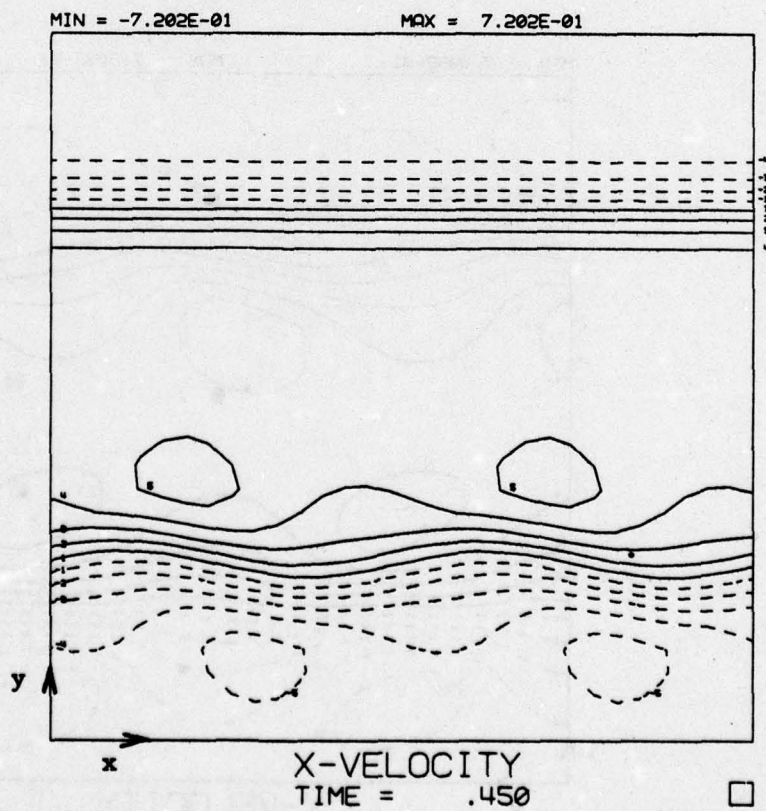
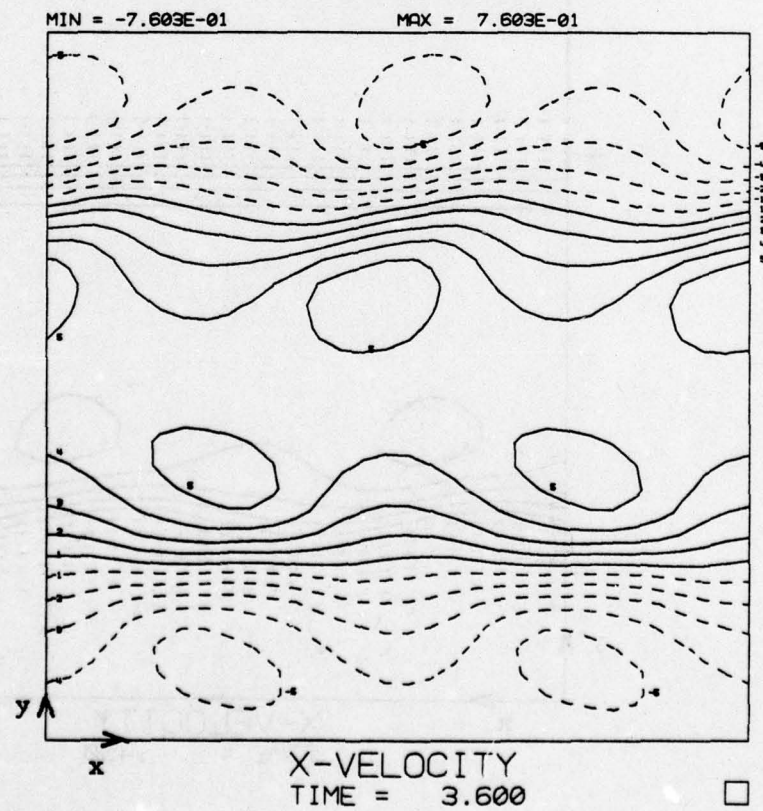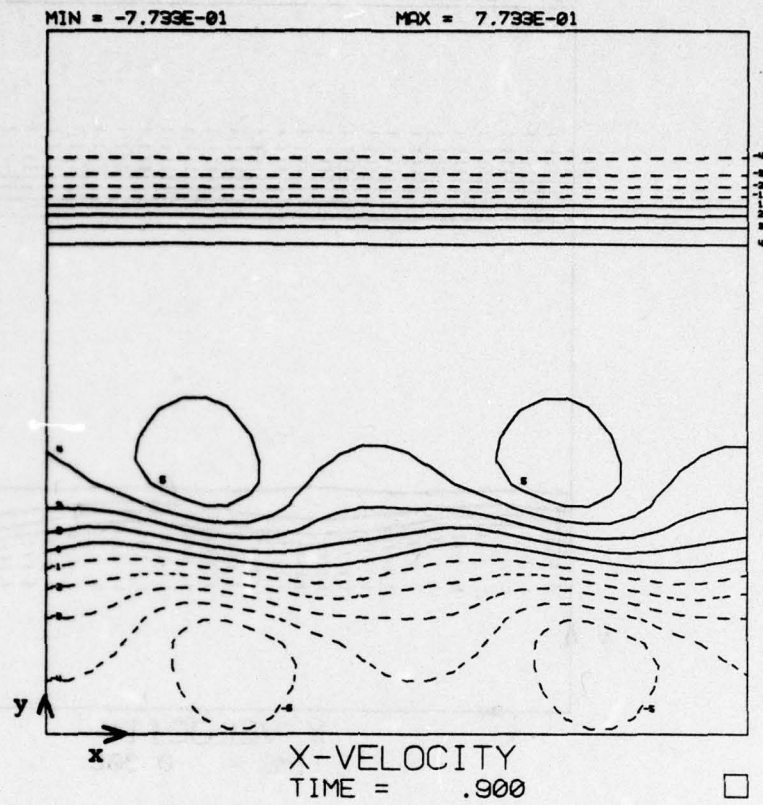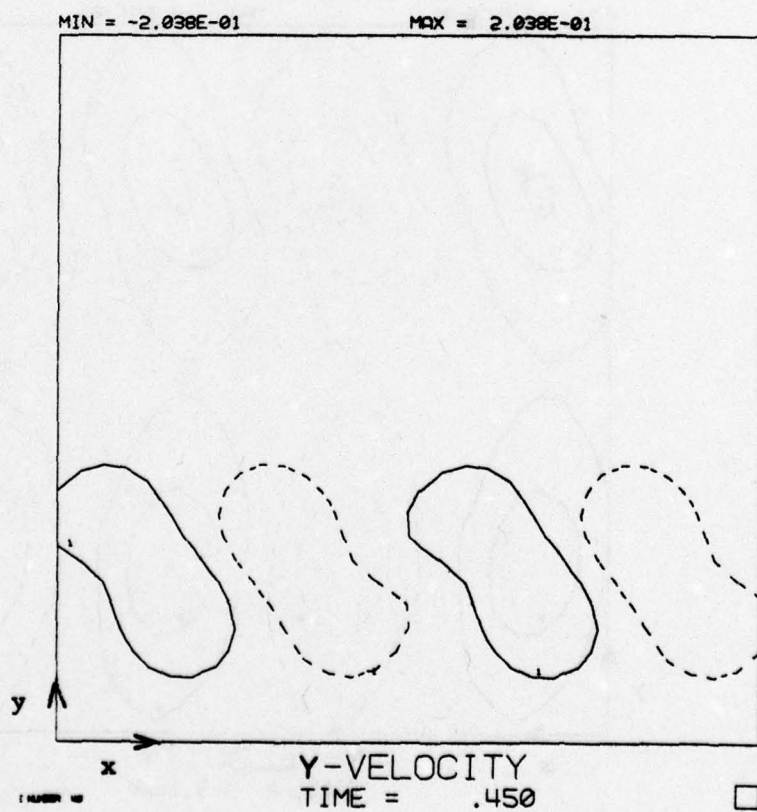Figure 44. Contours u_x for streamwise perturbation, z = 0 .

99
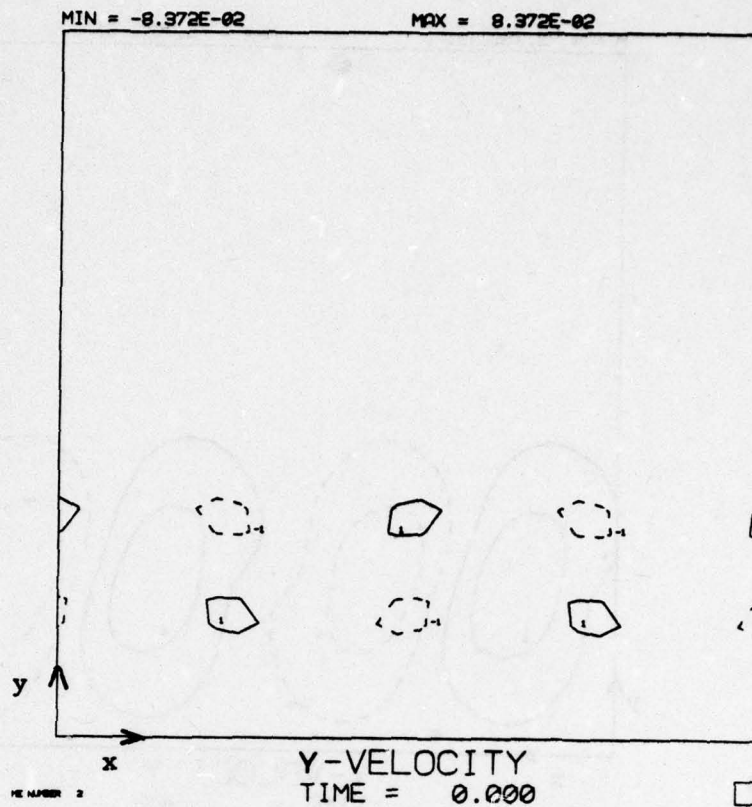
Figure 45. Continuation of Figure 44.

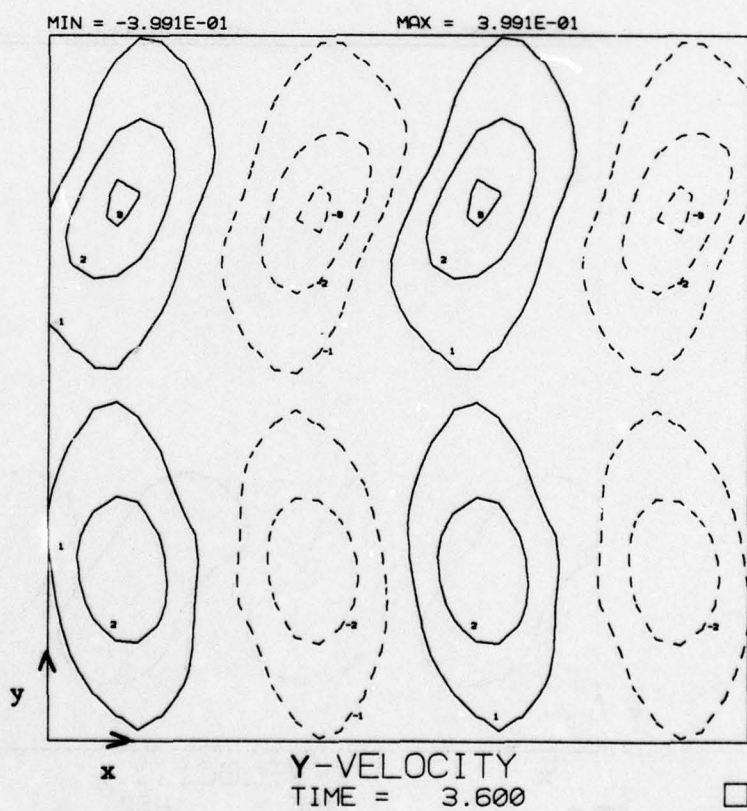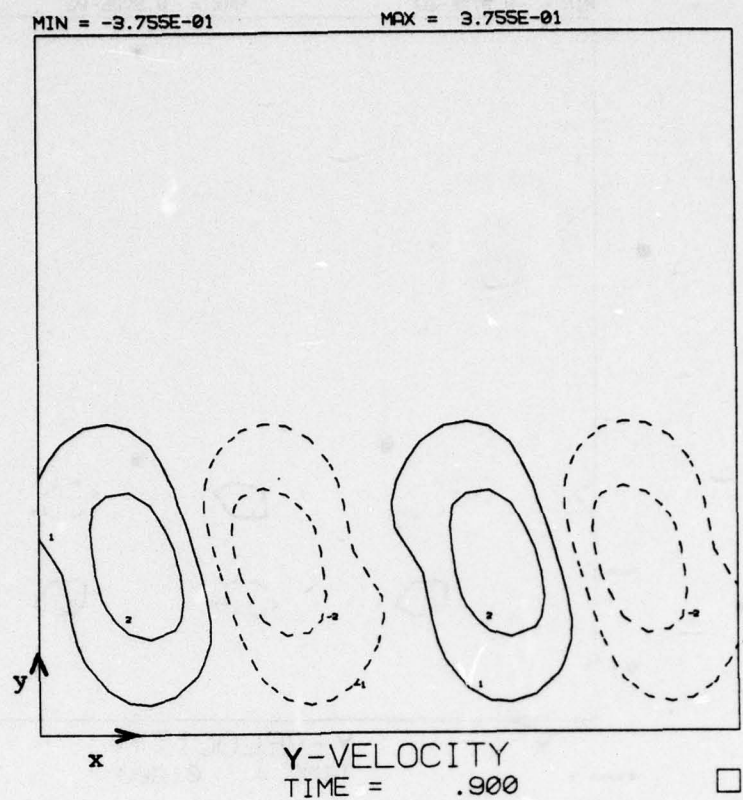Figure 46. Contours u_y for streamwise perturbation, $z = 0$.

101

MIN = -3.755E-01   MAX = 3.755E-01

Y-VELOCITY
TIME =   .900

MIN = -3.991E-01   MAX = 3.991E-01

Y-VELOCITY
TIME =   3.600

Figure 47. Continuation of Figure 46.

102

t = 0.45

t = 0.45

t = 0

t = 0

Figure 48. Vortex lines for 3-D perturbation, perturbed layer.

t = 1.8

t = 0.9

t = 1.8

t = 0.9
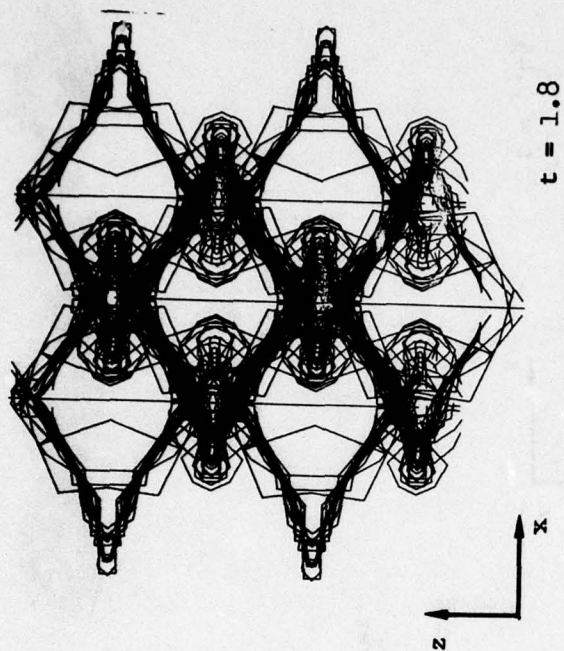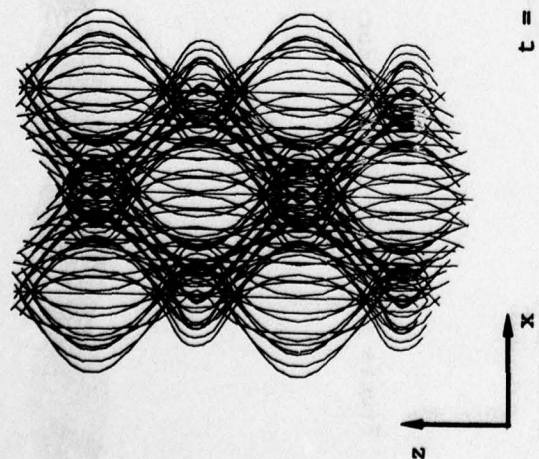
Figure 49. Continuation of Figure 48.
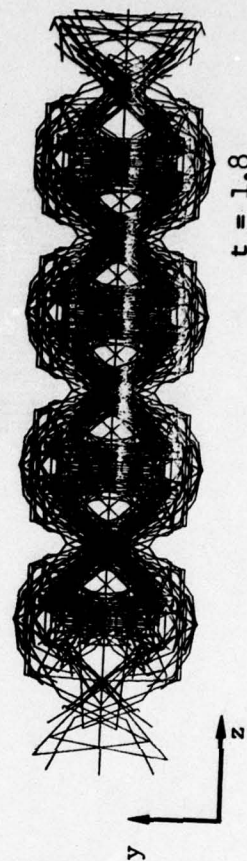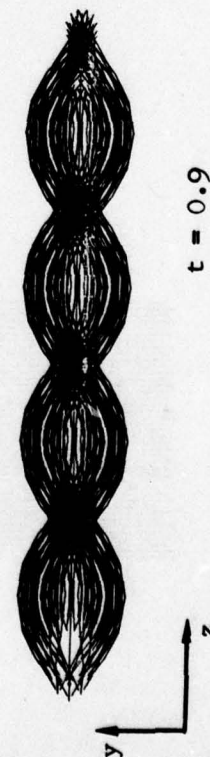
obscure due to the intense stretching of the filaments from streamwise perturbations. It is then more informative to look at the different contours of vorticity and velocity. The twelve next figures (50-61) show six groups of four stills for different contours taken at the center of the computational box, $x = 0$. Sequentially, we have the (y-z) contours of ω_x, ω_y, ω_z, u_x, u_y, and u_z .

In our four last figures, we combine, for comparison purposes, the results obtained through the streamwise perturbation and the ones obtained through the three-dimensional perturbation. Figure 62 displays, on a semi-logarithmic scale, the streamwise and spanwise components of total energy versus time for both cases. Of course, the two-dimensional mixing layer does not exhibit a spanwise contribution of energy since its spanwise component of velocity is null. In Figure 63 , we see the cross-flow component of total energy versus time for both cases; since the energy variation is plotted on a semi-logarithmic scale with respect to time, the initial linear section of the curve represents the exponential growth of the component energy in time, and its slope is hence the linear growth rate[58,59,60,61]. Figure 64 shows the total energy versus time for both cases. In the two-dimensional case, the energy stays constant whereas the three-dimensional case implies stretching of the vortices: at $t = 2.7$, the energy has increased by only one percent but at $t = 3.6$, the total energy is up by eleven percent. Finally in the last figure (65), the total enstrophy versus time is displayed for both cases.

The main conclusion to be drawn from these computer experiments is that the third dimension is extremely important in the evolution of a mixing layer even though it is an "ignorable coordinate" in the idealized uniform shear flow.
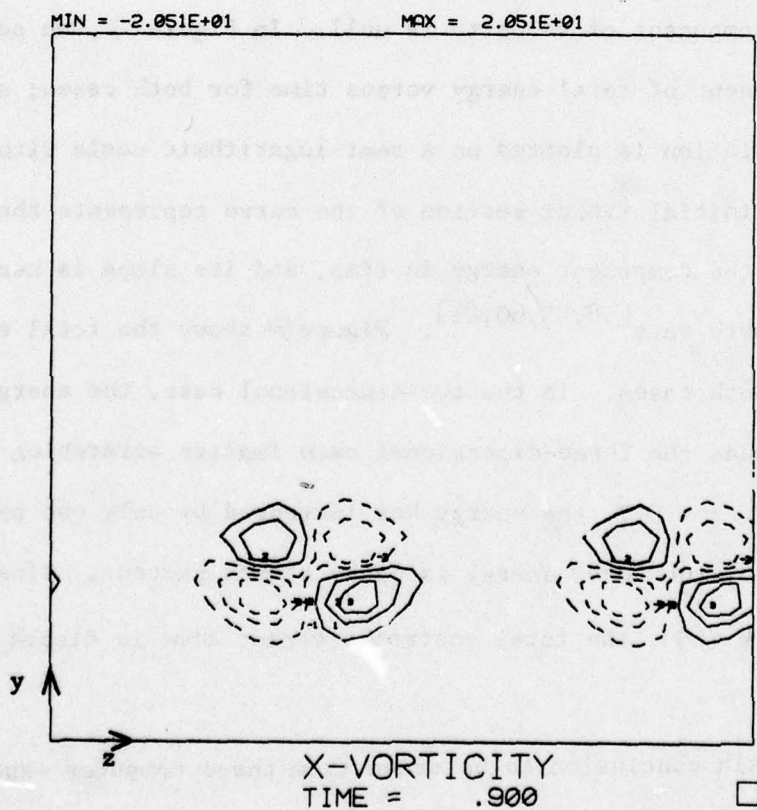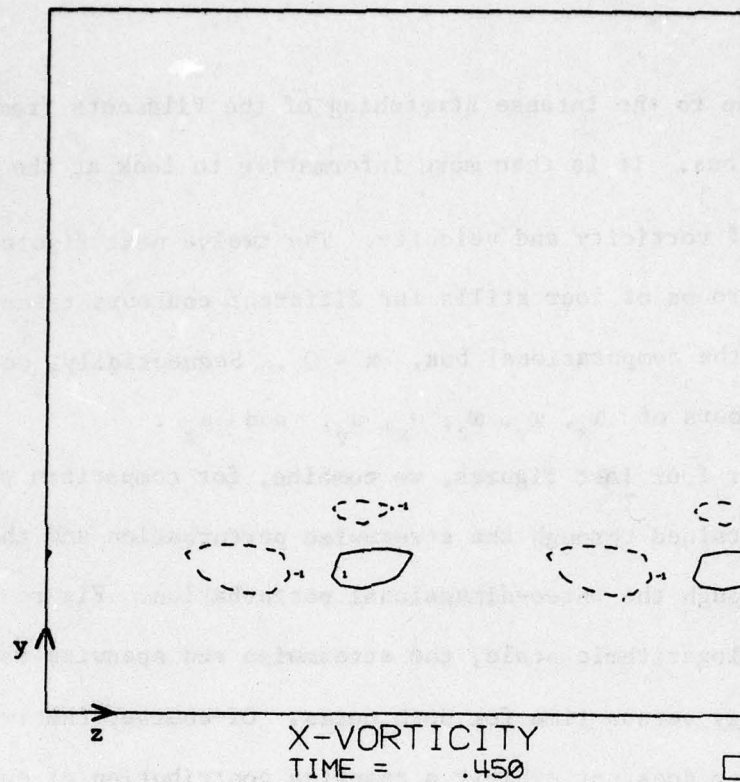
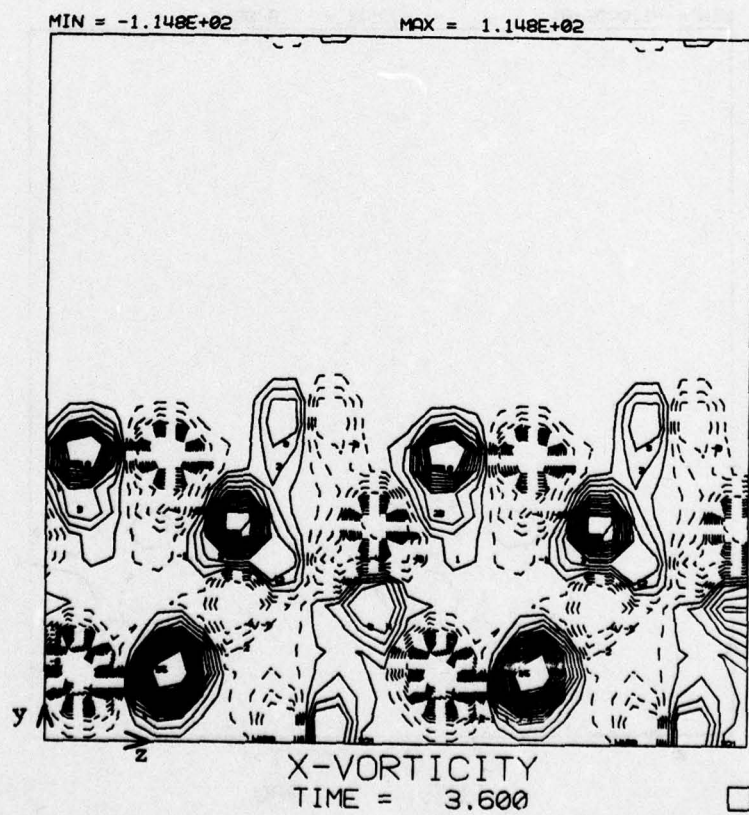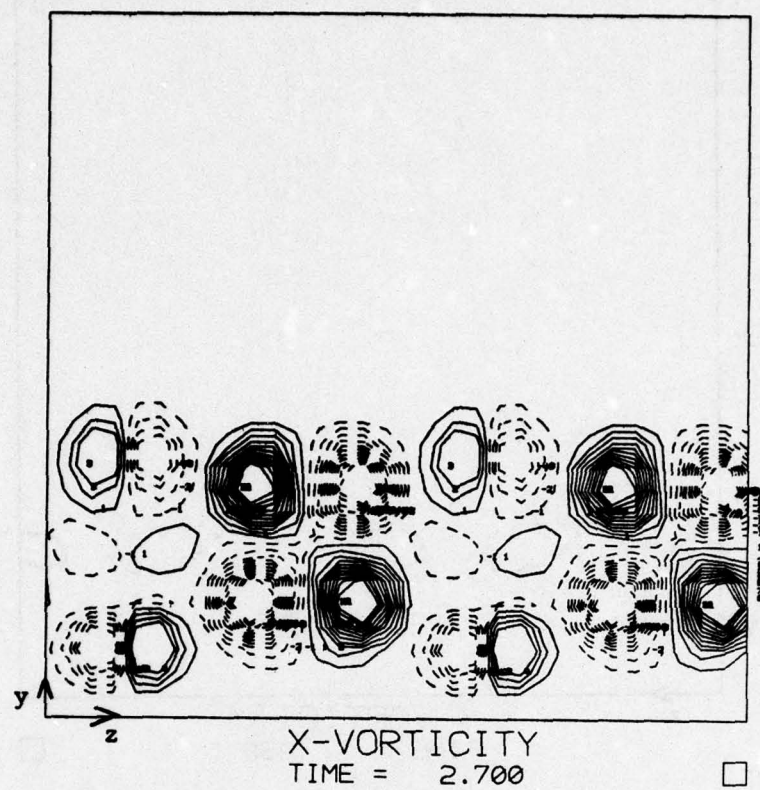Figure 50. Contours ω_x for 3-D perturbation, x = 0 .

106

X-VORTICITY
TIME = 2.700

MIN = -1.148E+02   MAX = 1.148E+02

X-VORTICITY
TIME = 3.600

Figure 51.   Continuation of Figure 50.

107

Figure 52. Contours ω_y for 3-D perturbation, $x = 0$.

Y-VORTICITY
TIME = 2.700

MIN = -3.960E+01   MAX = 3.060E+01

Y-VORTICITY
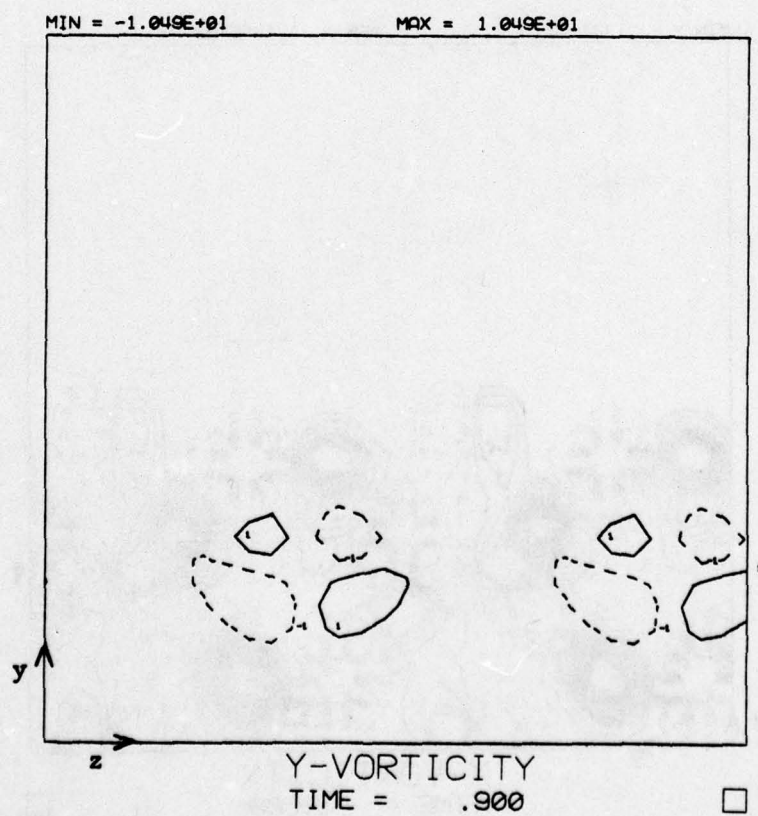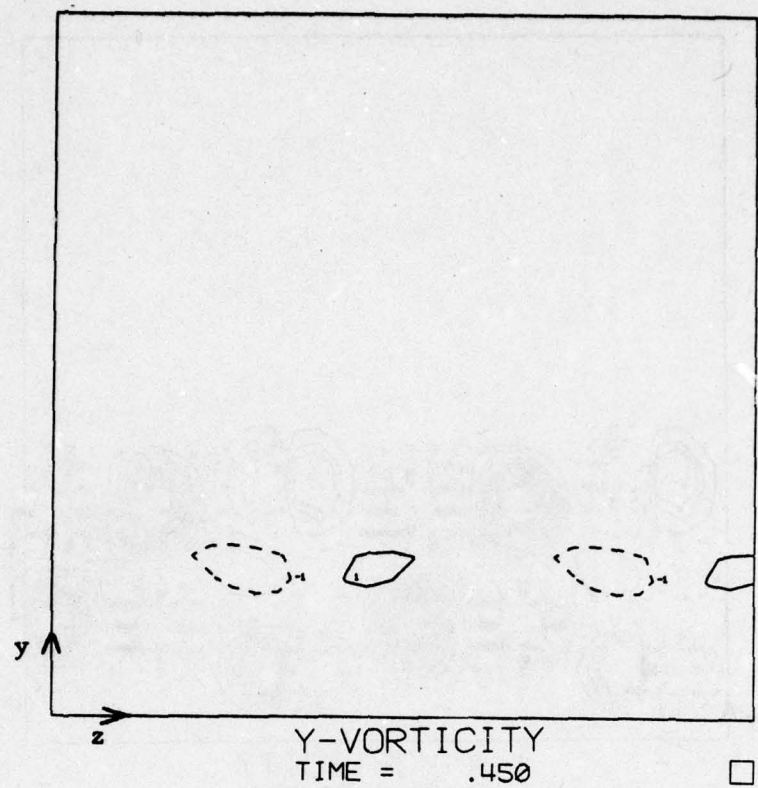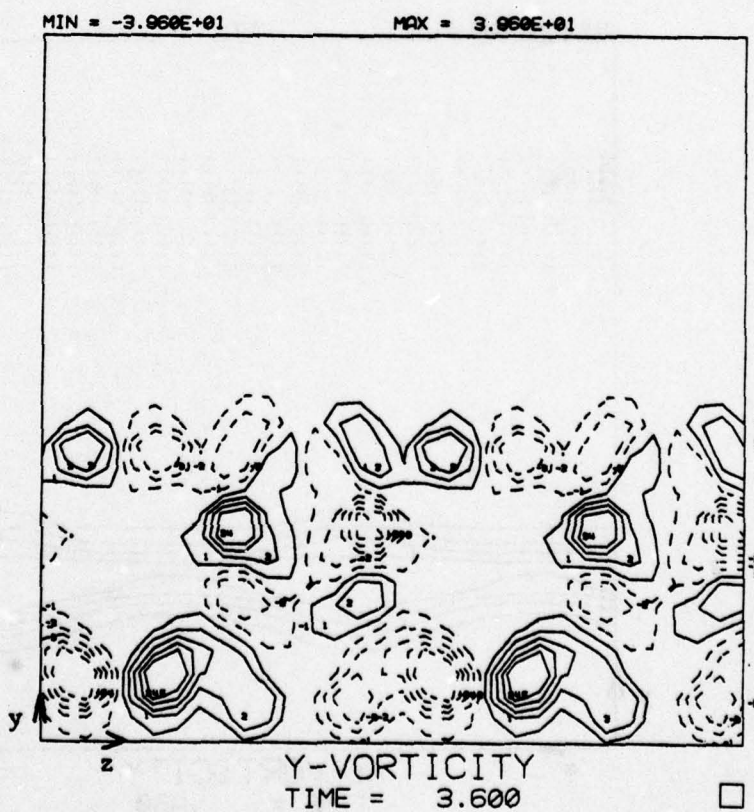TIME = 3.600

Figure 53. Continuation of Figure 52.

109

Figure 54. Contours ω_z for 3-D perturbation, $x = 0$.
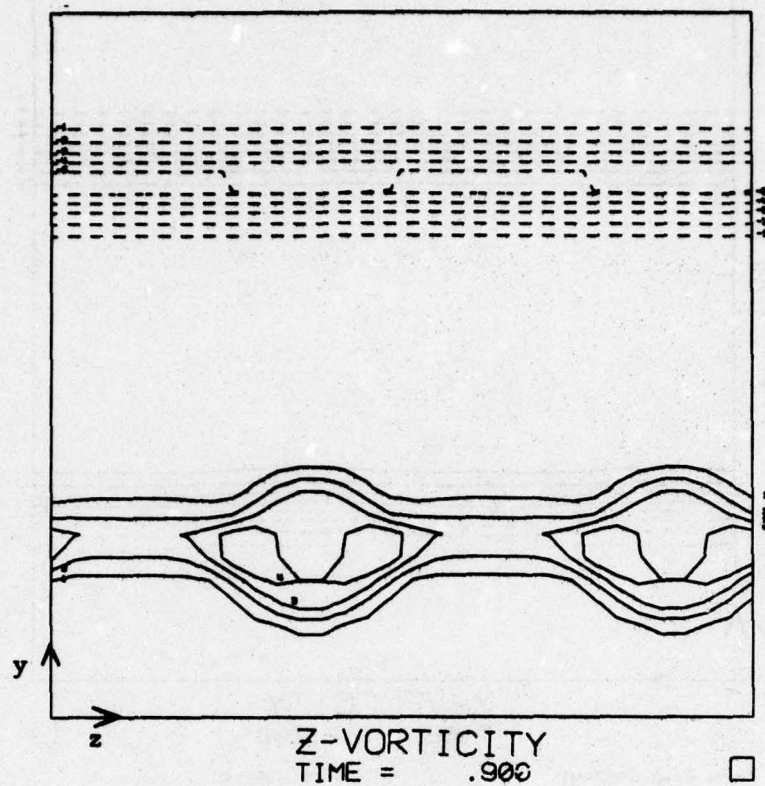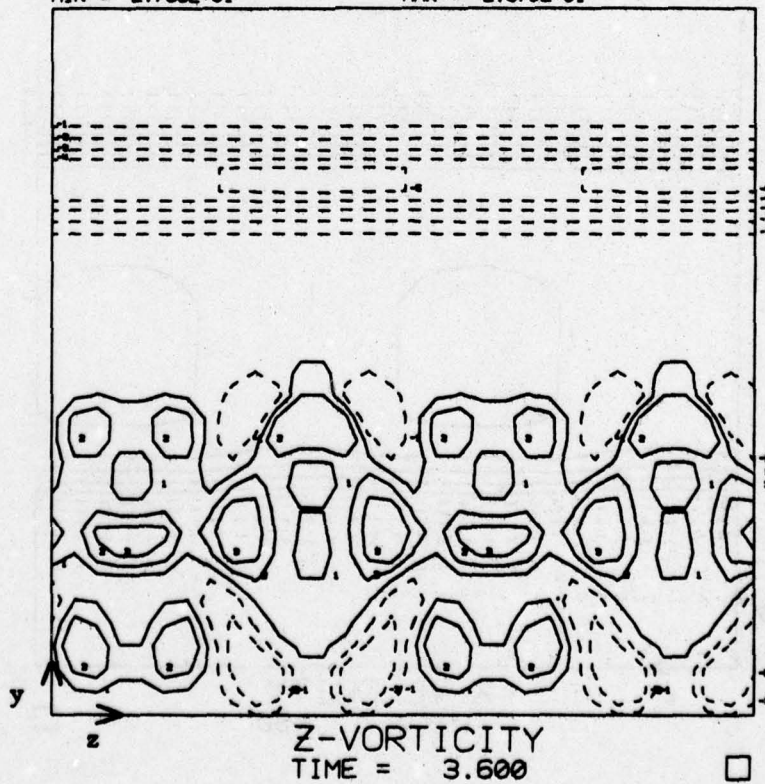
Figure 55. Continuation of Figure 54.

X-VELOCITY
TIME = 0.000

MIN = -6.491E-01   MAX = 6.439E-01

X-VELOCITY
TIME = .450
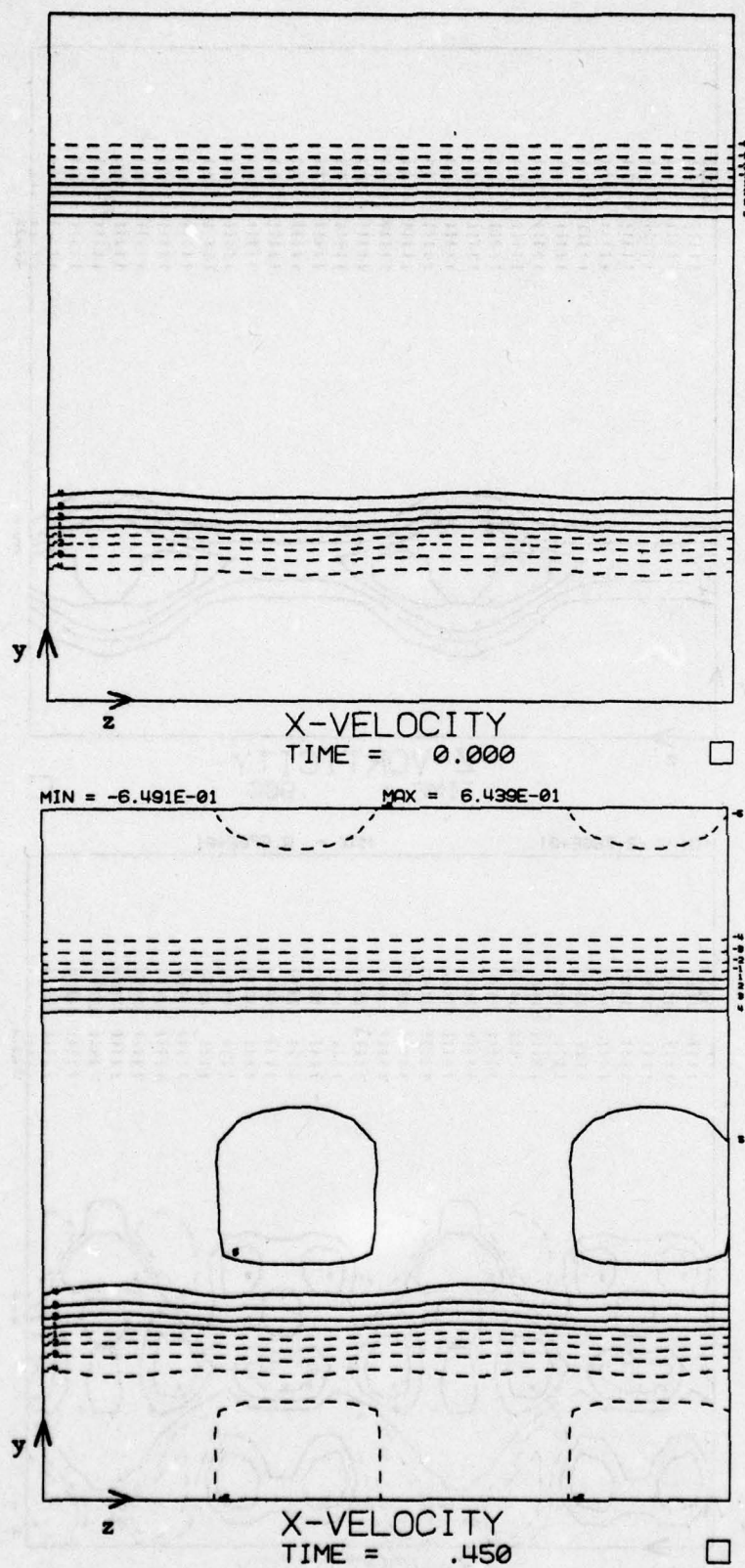
Figure 56. Contours u_x for 3-D perturbation, $x = 0$.

112
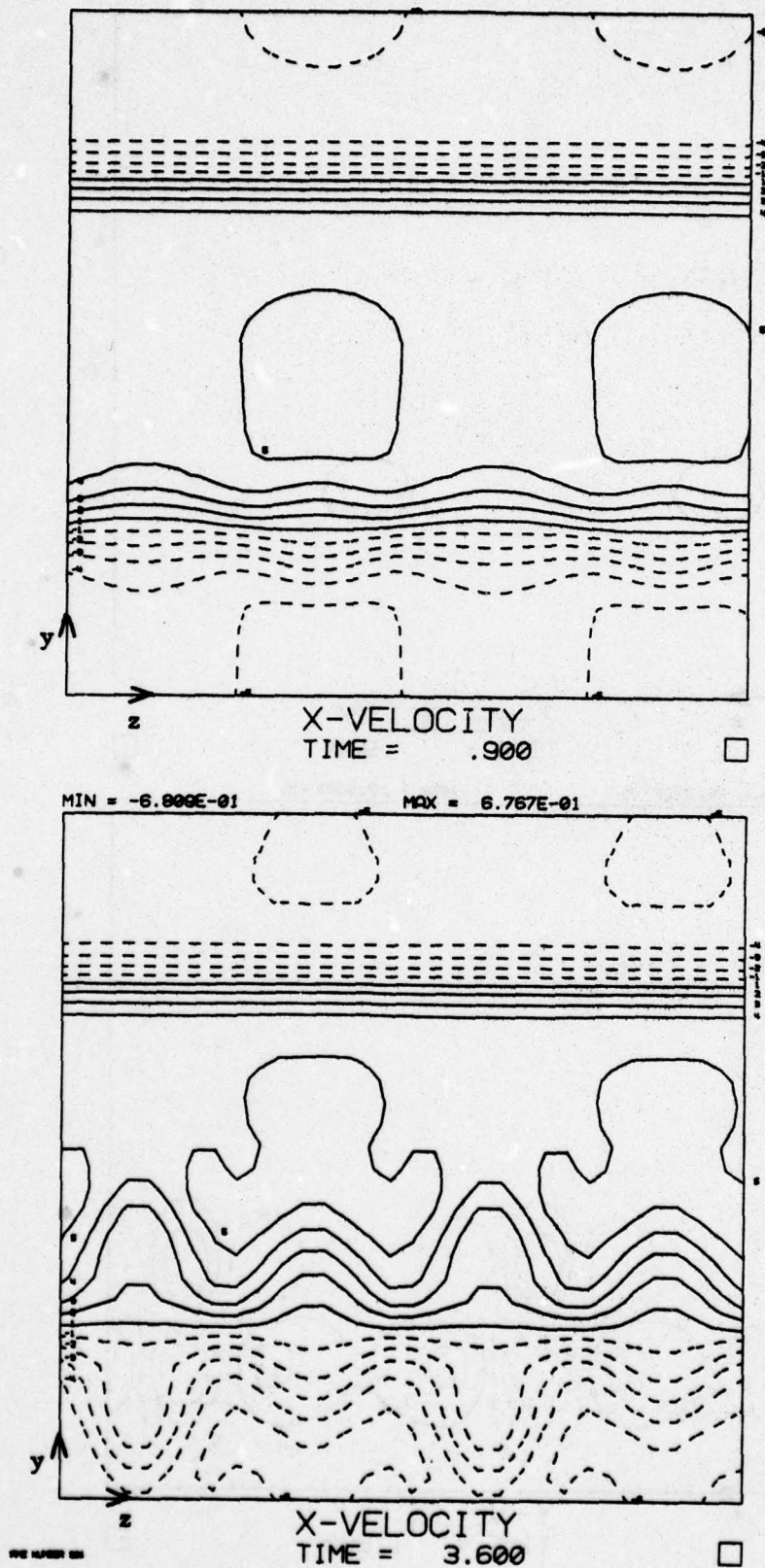
Figure 57. Continuation of Figure 56.

113
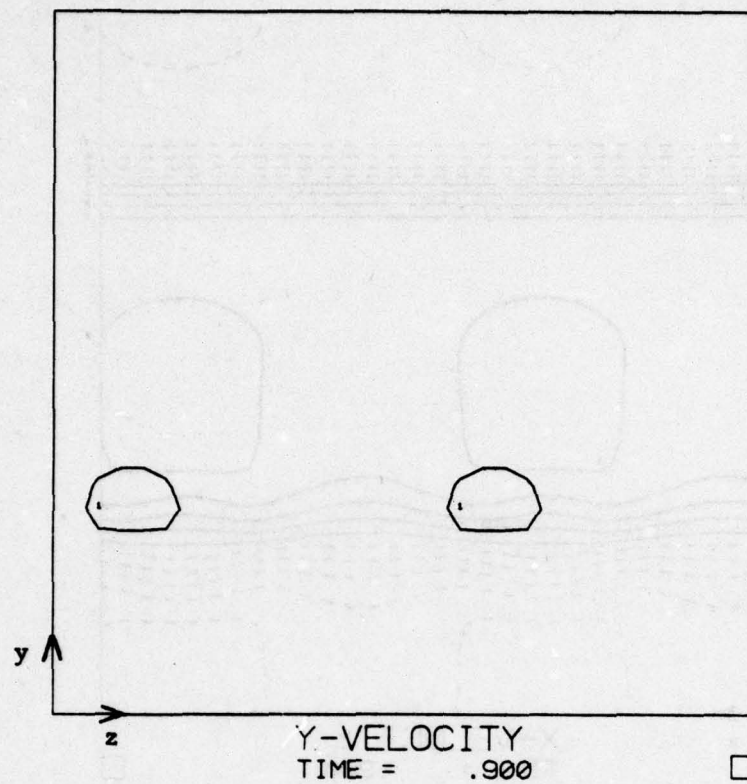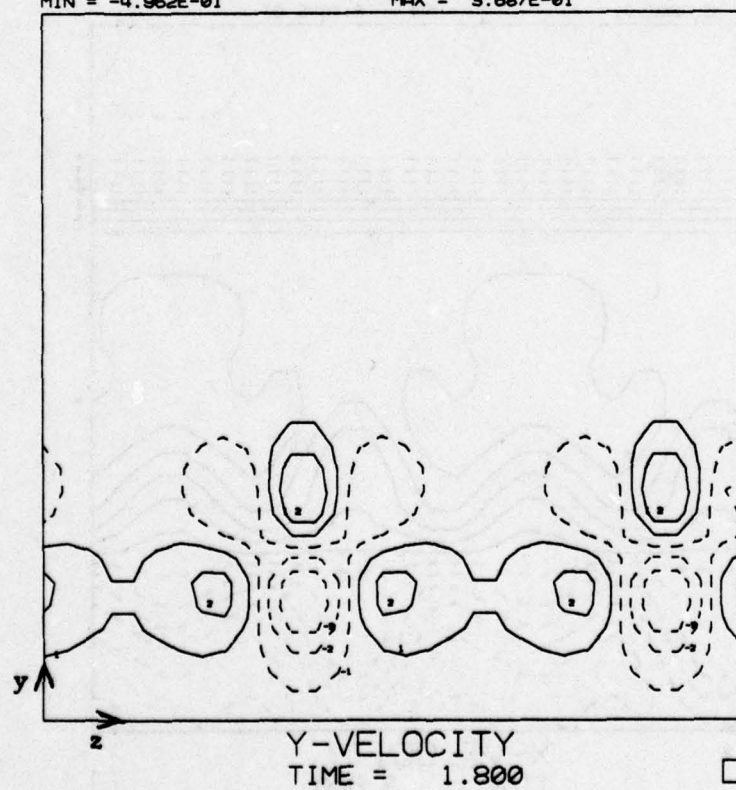
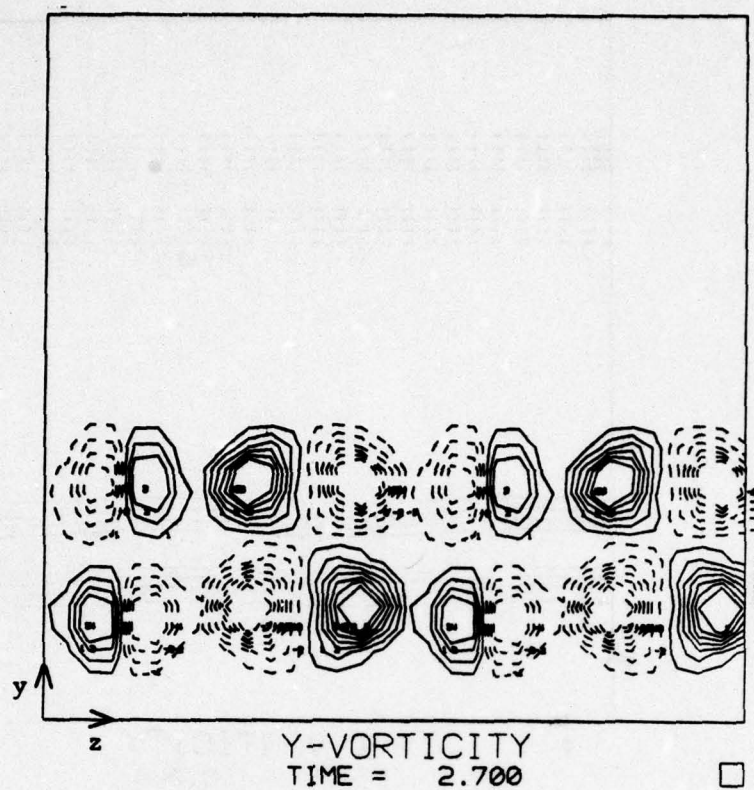Figure 58. Contours u_y for 3-D perturbation, $x = 0$.
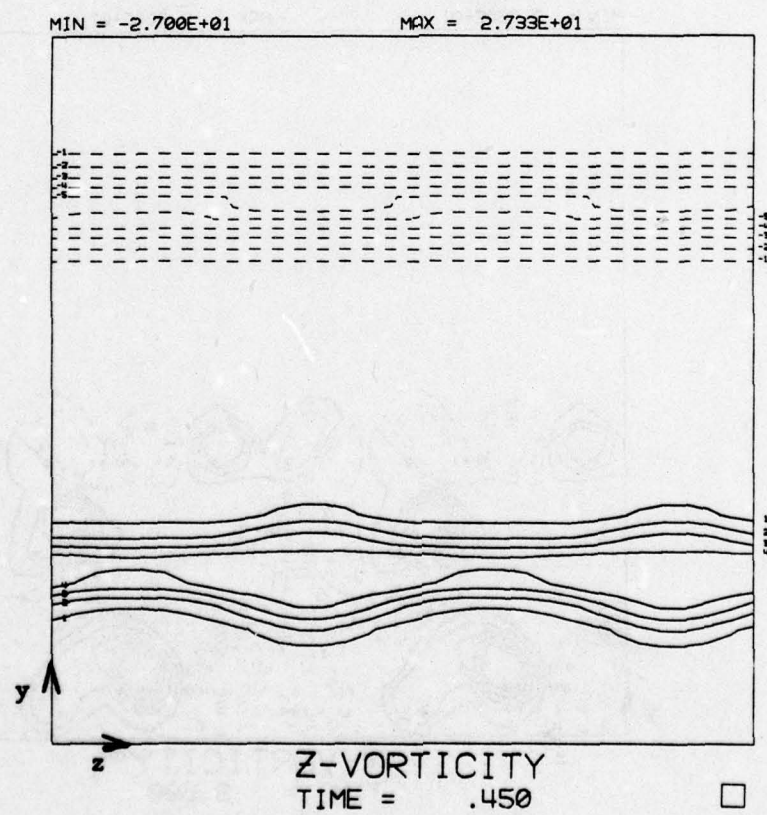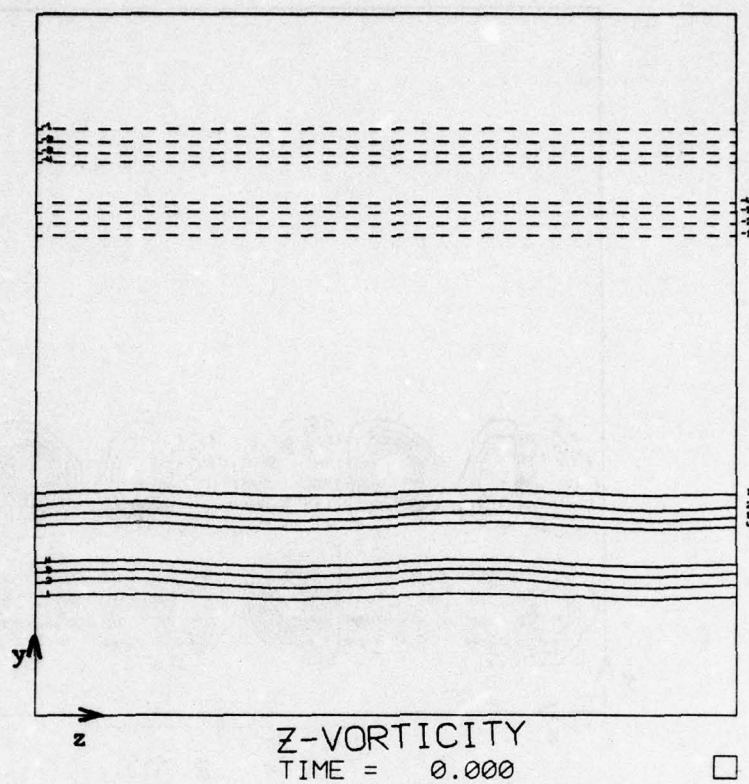
114
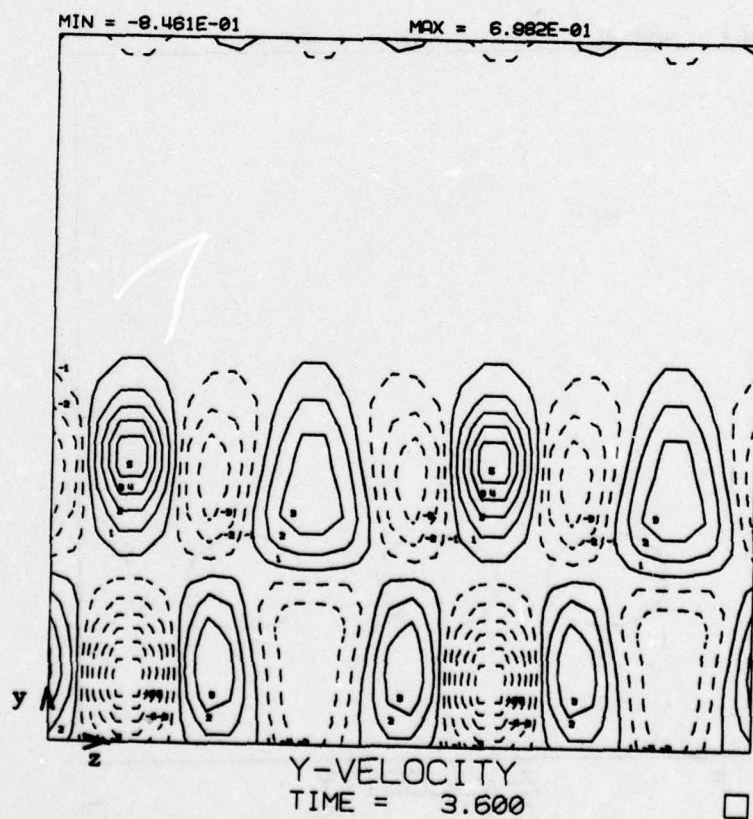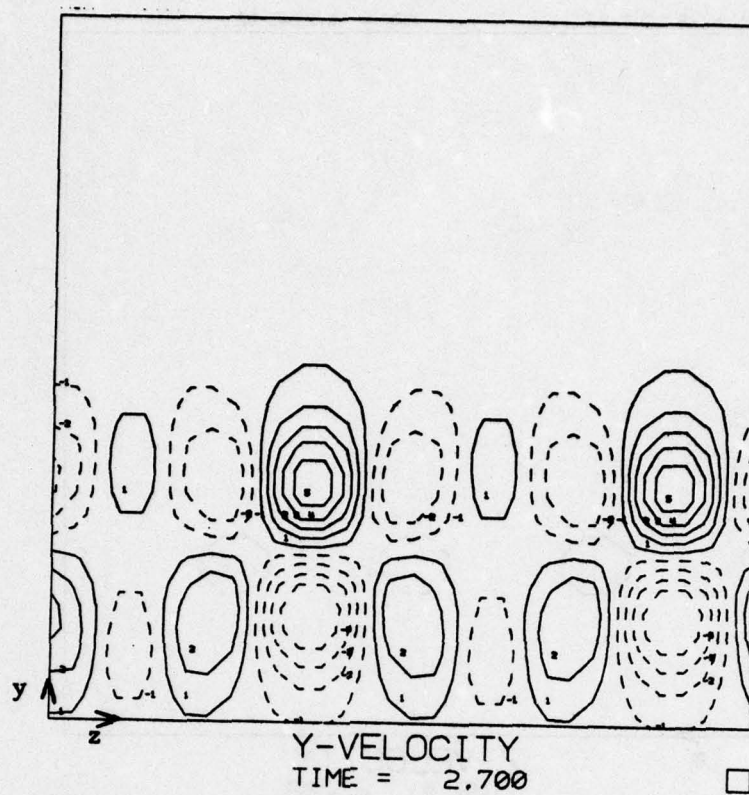
Figure 59. Continuation of Figure 58.

115

MIN = -8.224E-02   MAX = 8.224E-02

Z-VELOCITY
TIME =   0.000

MIN = -1.489E-01   MAX = 1.489E-01

Z-VELOCITY
TIME =   .450
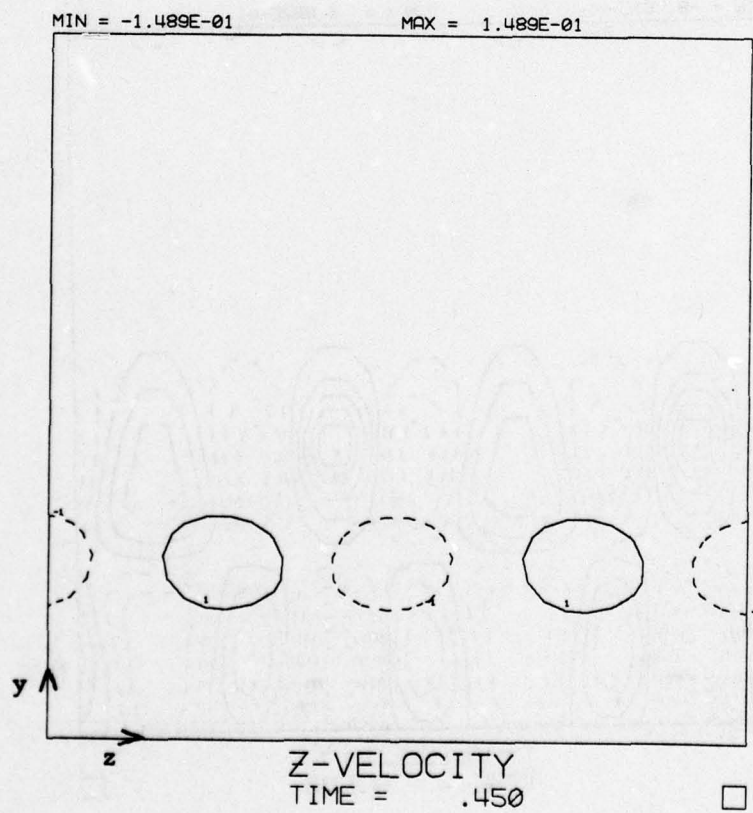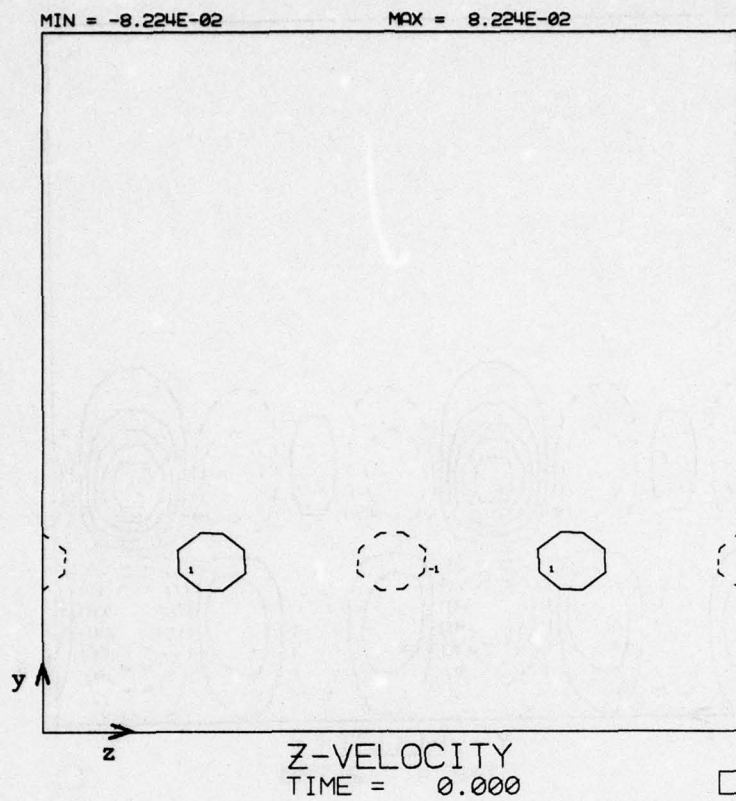
Figure 60. Contours u_z for 3-D perturbation, x = 0 .

Figure 61. Continuation of Figure 60.

117
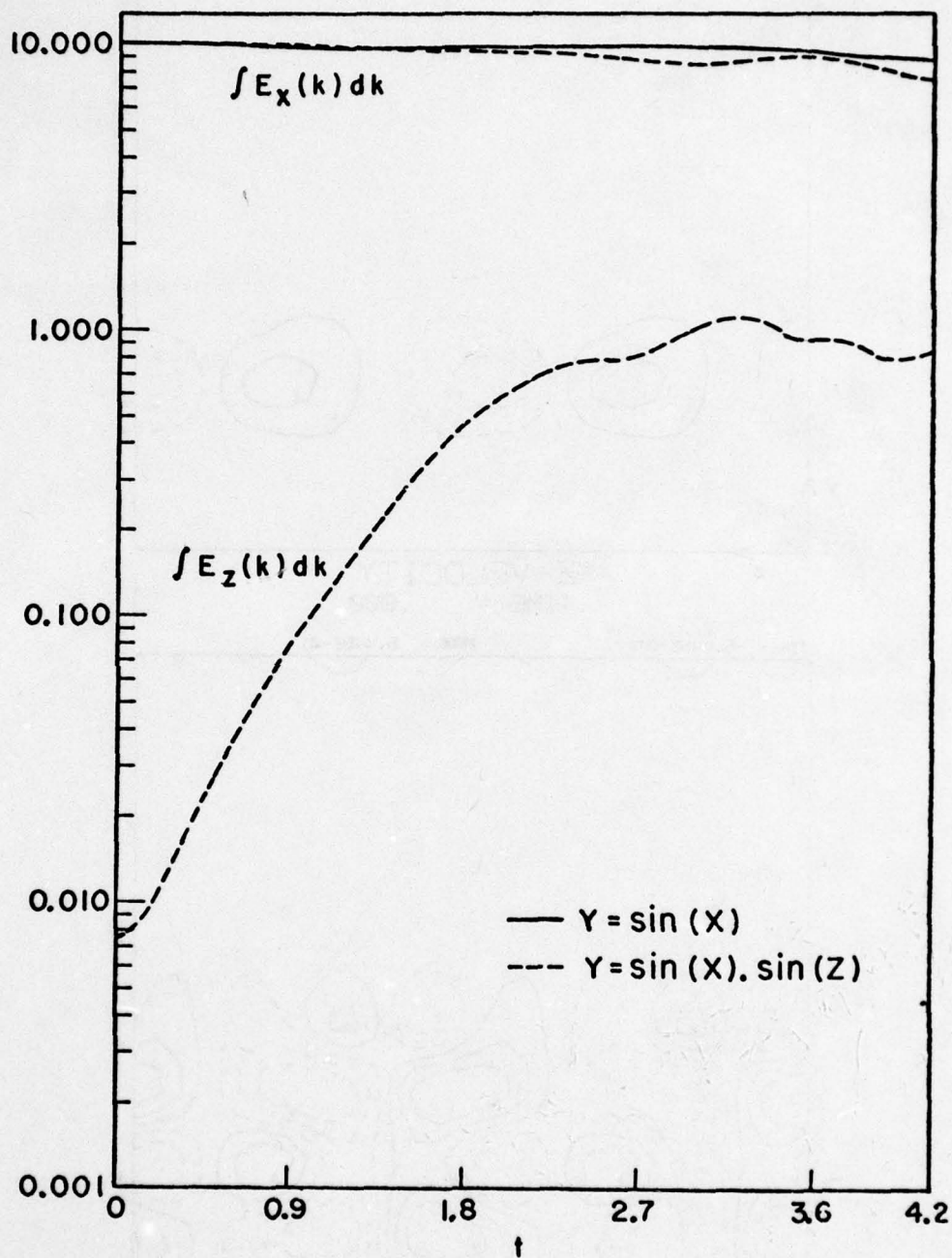
Figure 62. Streamwise and spanwise components of total energy versus time, for 2-D(—) and 3-D(---) perturbations.
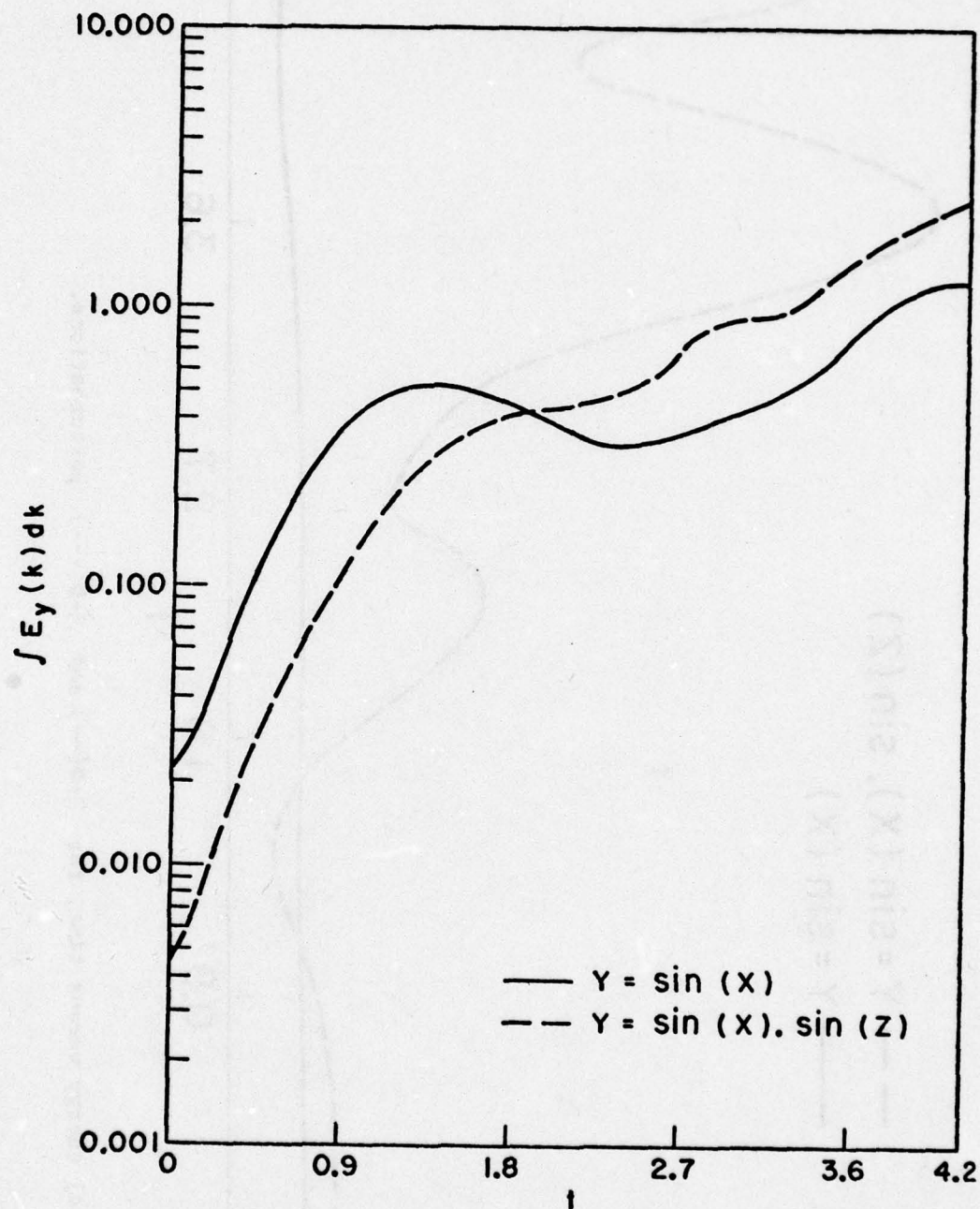
Figure 63. Cross-flow component of total energy versus time, for
2-D(——) and 3-D(---) perturbations.
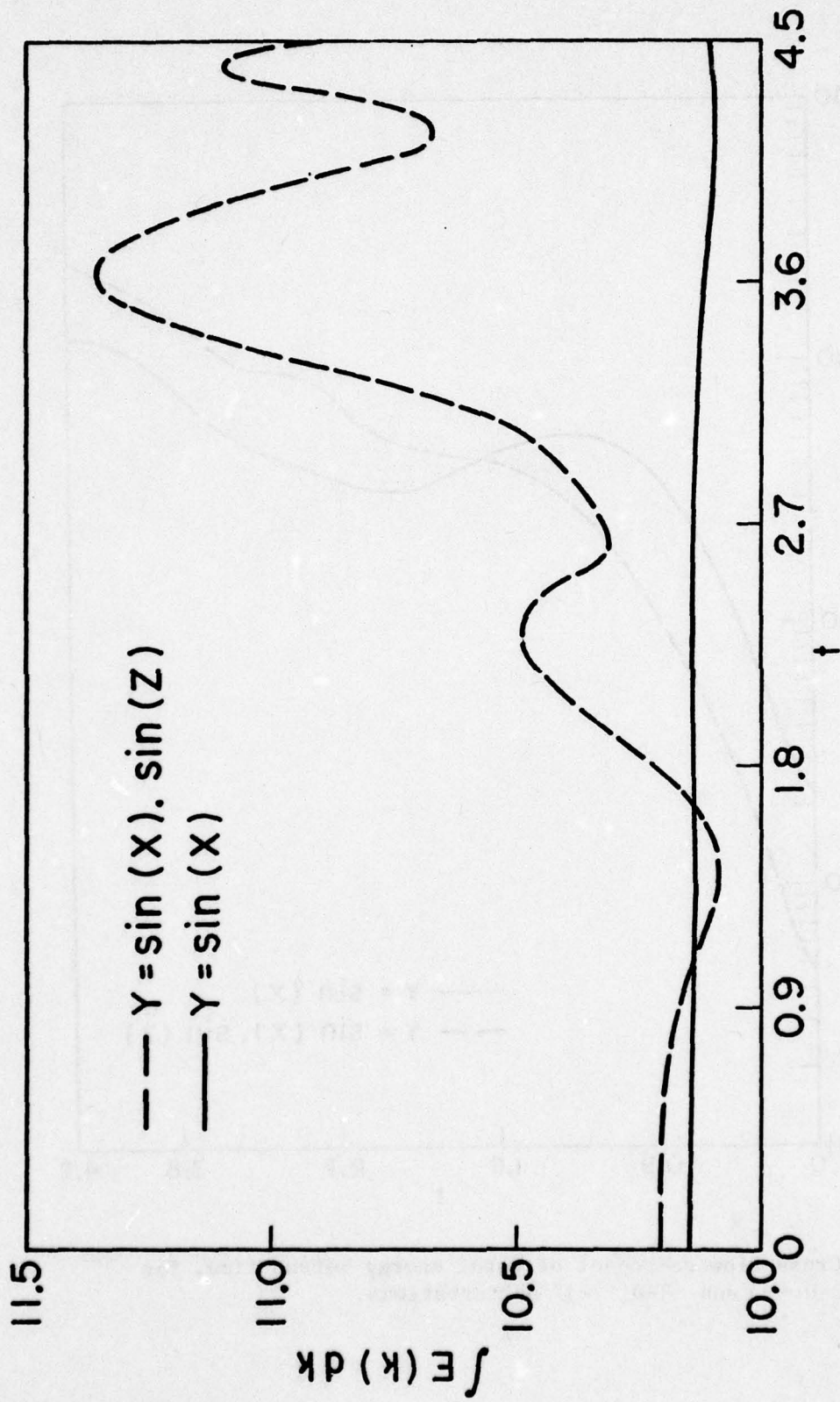
Figure 64. Total energy versus time, for 2-D(——) and 3-D(---) perturbations.
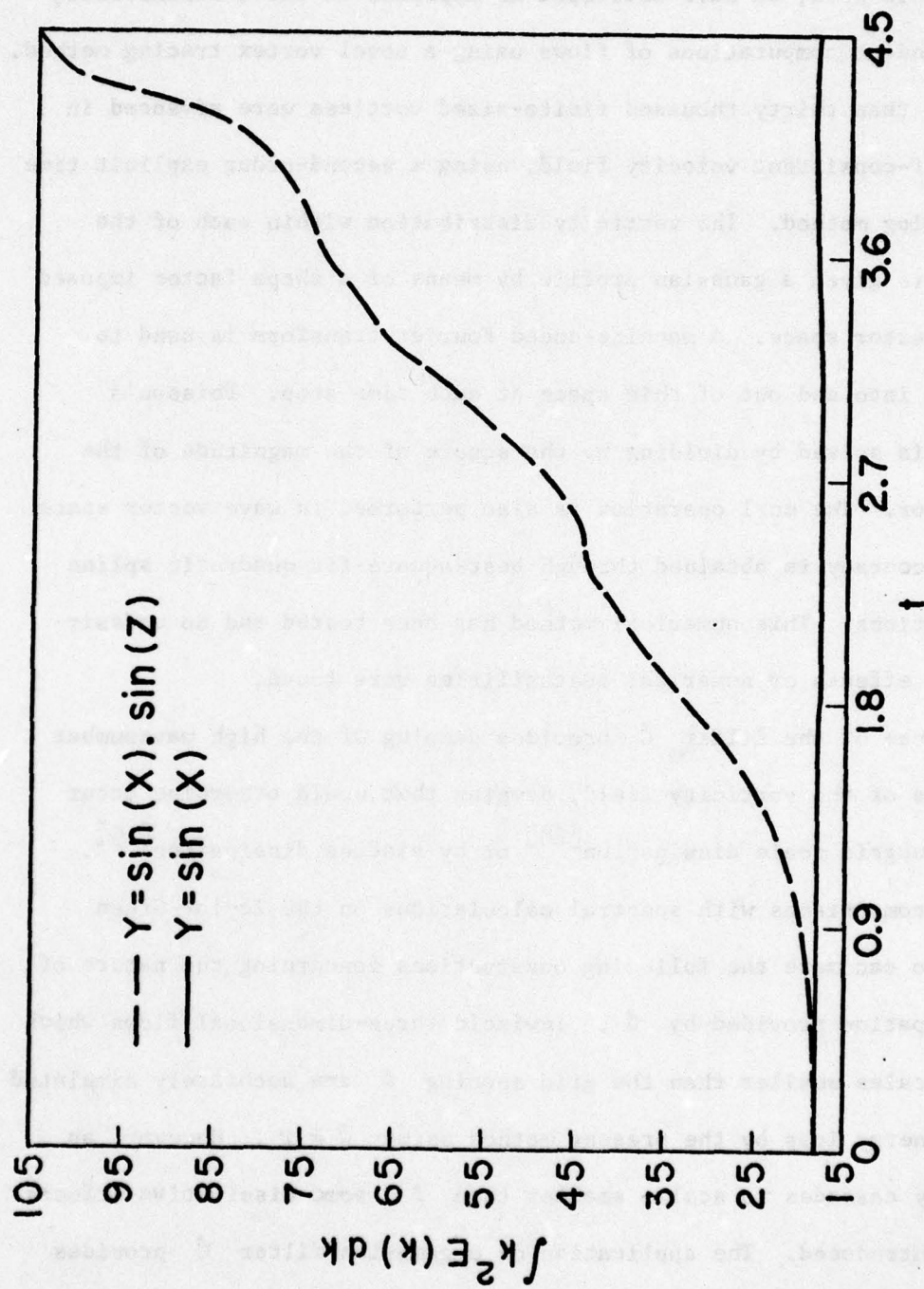
Figure 65. Total enstrophy versus time, for 2-D(—) and 3-D(---) perturbations.

Chapter V

CONCLUSION

In this work, we have developed an approach to three-dimensional, time-dependent computations of flows using a novel vortex tracing method.

More than thirty thousand finite-sized vortices were advanced in their self-consistent velocity field, using a second-order explicit time differencing method. The vorticity distribution within each of the vortices is given a gaussian profile by means of a shape factor imposed in wave vector space. A machine-coded Fourier transform is used to transform into and out of this space at each time step. Poisson's equation is solved by dividing by the square of the magnitude of the wave vector. The curl operation is also performed in wave vector space. Subgrid accuracy is obtained through best-square-fit quadratic spline interpolations. This numerical method has been tested and no undesirable grid effects or numerical instabilities were found.

The use of the filter $\hat{G}$ provides damping of the high wavenumber components of the vorticity field, damping that would otherwise occur through subgrid scale dissipation[28] or by viscous dissipation[19]. Based on comparisons with spectral calculations on the Taylor-Green problem we can make the following observations concerning the natu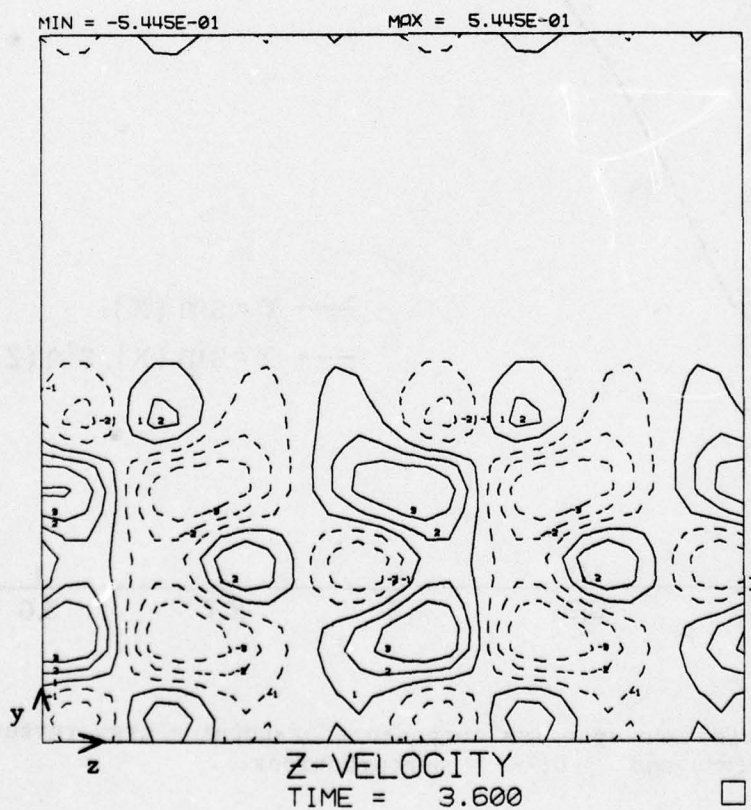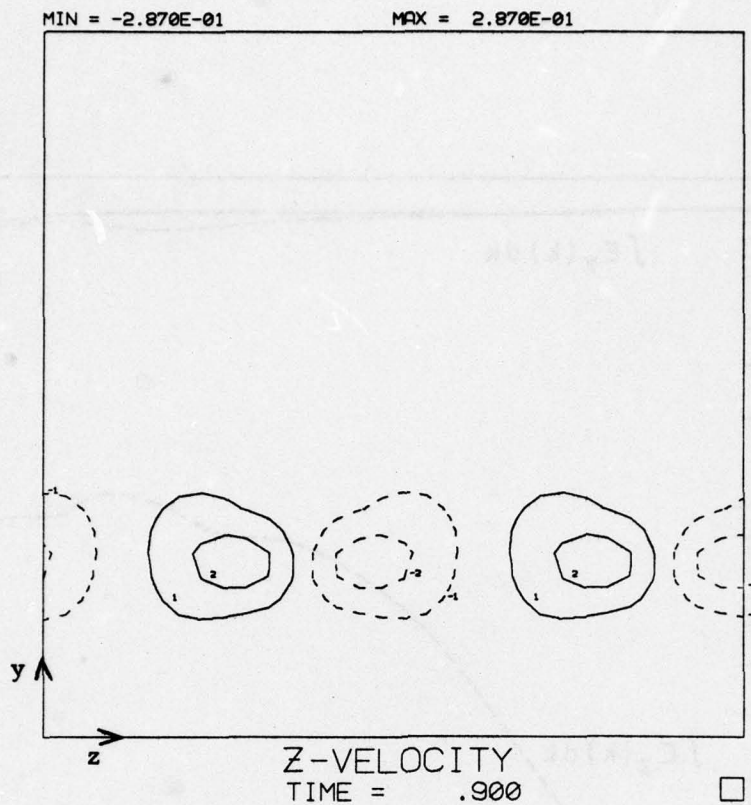re of the dissipation provided by $\hat{G}$. Inviscid three-dimensional flows which have no scales smaller than the grid spacing Δ are accurately simulated with no energy loss by the present method using $\hat{G} = 1$. However, as the energy cascades to scales smaller than Δ , some dissipative effects must be introduced. The application of a gaussian filter $\hat{G}$ provides energy dissipation for the Taylor-Green problem, where such a cascade exists, but produces no loss of energy for the case of a single vortex ring or a pair of coaxial rings, i.e. when there is no cascade. Based

on this limited experience, we believe the use of a filter $\hat{G}$ yields
an appropriate model of subgrid scale dissipation.

Compared with a purely Lagrangian method for the case of the vortex
rings and with a purely spectral method for the Taylor-Green system, we
saw that our vortex-in-cell method can certainly compete in computing
time efficiency and adequately produce the same accuracy for real and
spectral dynamics results. It is a great advantage to be able to gener-
ate direct visualizations of the real flow together with all kinds of
spectra, so useful in the study of turbulence[19]. This advantage was
used to produce movies of the vortex line evolution, for the Taylor-Green
system and for the mixing layer, alongside with movies showing the cas-
cading of energy from the lower to the higher modes.

Also, through vorticity and velocity contours taken at each time
step, our preliminary study of the mixing layer showed the now well-
established two-dimensional vortex roll disturbance. The exponential
growth in the cross-flow component of energy for the two- and three-
dimensional cases was also observed. It was remarkable to see, in the
three-dimensional perturbation case, distinct streamwise distortions
and "cusping" due to the stretching of the vortex lines.

A discussion of the limitations of our method of performing fluid
dynamical experiments on the computer is called for, namely:

    a) the fluid is treated as incompressible

    b) gravitation (buoyancy) has not been taken into account

    c) the viscosity is not defined explicitly

    d) the boundary conditions are periodic

    e) the number of elementary vortices, although large, is finite

    f) all elementary vortices are of the same finite-size profile

123

Limitations (a) and (b) can be overcome by including consideration of potential flow contributions which are affected by pressure and buoyancy (transport of vortices is not). Our method could then be applied to studying, for instance, Rayleigh-Taylor instabilities[62,63].

One way of introducing explicitly the effect of viscosity is to change the size of the elementary vortices according to their age, in other words, to remove the limitation (f) . Some ad-hoc methods for modifying the effective size of vortices have been suggested by Buneman[38]: to some extent, one can make up thinner, younger vortices by surrounding a positive (clockwise) vortex concentrically with a halo of negative (anti-clockwise) vortices. However, the limit of resolution is set by the cut-off imposed in $\vec{k}$-space, and such narrowed patterns tend to result in undesirable sidebands or aliasses. Chorin and Bernard[18] treat close elementary vortices as singular filaments by direct interaction and let only distant vortices interact via the grid. By close and distant, we mean less or greater than a few times the rms vortex profile radius. They then use a random walk of filamentary vortices as a spreading device to simulate viscous effects. Their work was two-dimensional. Such a hybrid method (the PPPM method, for particle-particle/particle-mesh) of treating interacting objects was employed successfully in simulations of molecular interactions[64]. A linked list is kept which allows one to find nearest neighbors up to any chosen distance and calculate their direct effect, as well as the effect which one would have obtained from them via the mesh. The difference is then added to the total mesh field. In this manner, the more localized nature of the flow field due to stretched or young vortices can be properly distinguished from the broader flow field of compressed and old vortices.

Non-periodic boundary conditions can be simulated in a variety of ways. One way is to use readily available sine and cosine transforms instead of complex exponentials to simulate (possibly vortex-shedding) planar walls in one or two of the three dimensions. One would retain periodicity in the third dimension, having in mind the simulation of channel flow or flow through a re-entrant wind tunnel of rectangular cross-section (but with curvature effects absent). Another variant is the simulation of "infinite" boundary conditions using similar approaches as in[65] and in[66]. In the case of the mixing layer, the use of periodic boundary conditions is justifiable only if one moves with the mean speed of the flow. However, the size of the eddies grows linearly with the streamwise distance, and one reaches a point at which the size of the computational box must be increased. This problem can be eliminated if a way can be found to work in an infinite domain. From a practical point of view, this means that we must either use functions appropriate to such a domain, e.g., Laguerre or Hermite polynomials, or use a mapping which makes the transformed domain finite. We shall look into the possibility of making use of some kind of mesh mapping in the crossflow direction. In order to preserve the applicability and usefulness of the Fourier methods, the mapping should be chosen in such a way that these methods can be applied with little loss in convenience or accuracy[67].

Restriction (e) is merely a limitation due to computer memory size and will be alleviated with improved computer technology. 64×64×64 mesh codes handling almost one million particles are already becoming available for plasma simulations and could be adapted to vortex tracing. However, the large data bases required in such codes call for non-trivial modifications of our present mode of operation: first, most data will have to reside on disc most of the time, to be read in for the

arithmetic and immediately written out again. Second, a faster machine than the CDC 7600 is needed to process the many more vortex elements in a run of reasonable duration: one thinks of a Cray-1 or the soon to come Cray-2 computer!

Eventually, it may be possible to treat practical flows such as airfoils, combustion chambers, etc., by our method. Before that can be done, much more effort should first be devoted to developing an explicit model of the viscosity, the treatment of the boundary conditions and the mesh layout and/or mapping.

126

Appendix I

NUMERICAL INTEGRATION

On one hand, using the series expansion for sine, we have,

letting $\vec{k} \cdot \dfrac{(\vec{r}_j - \vec{r}_{j-1})}{2} = \epsilon_j$,

$$\frac{\sin \epsilon_j}{\epsilon_j} = 1 - \frac{1}{6}\epsilon_j^2 + \frac{1}{120}\epsilon_j^4 - \frac{1}{5040}\epsilon_j^6 + \ldots$$

On the other hand, we obtained in (3.2):

$$\widetilde{\vec{w}}(\vec{k}) = \Gamma \sum_{j=1}^{m} (\vec{r}_j - \vec{r}_{j-1}) \, I_j$$

where I_j stands for $\displaystyle\int_0^1 e^{-i\vec{k} \cdot \left[\xi\vec{r}_j + (1-\xi)\vec{r}_{j-1} \right]} \, d\xi$. By using the

trapezoidal rule to evaluate I_j , we get:

$$I_j = \frac{e^{-i\vec{k}\cdot\vec{r}_j} + e^{-i\vec{k}\cdot\vec{r}_{j-1}}}{2} + \text{Error}$$

where

$$|\text{Error}| = \left| \left[\frac{\vec{k}\cdot(\vec{r}_j - \vec{r}_{j-1})}{12} \right]^2 e^{-i\vec{k} \cdot \left[\xi\vec{r}_j + (1-\xi)\vec{r}_{j-1} \right]} \right|_{0 < \xi < 1} = \frac{\epsilon_j^2}{3}$$

This accuracy to the first order in ϵ_j is shown in the resulting

approximation of

$$\frac{\sin \epsilon_j}{\epsilon_j} \approx e^{i\vec{k}\cdot\frac{1}{2}(\vec{r}_j + \vec{r}_{j-1})} \left(\frac{e^{-i\vec{k}\cdot\vec{r}_j} + e^{-i\vec{k}\cdot\vec{r}_{j-1}}}{2} \right)$$

$$= \frac{e^{-i\epsilon_j} + e^{i\epsilon_j}}{2}$$

$$= \cos \epsilon_j = 1 - \frac{\epsilon_j^2}{2} + \ldots$$

To increase accuracy, we may use Simpson's rule to evaluate I_j :

$$I_j = \frac{1}{6} \left(e^{-i\vec{k}\cdot\vec{r}_j} + 4 \, e^{-i\vec{k}\cdot\frac{1}{2}(\vec{r}_j+\vec{r}_{j-1})} + e^{-i\vec{k}\cdot\vec{r}_{j-1}} \right) + \text{Error}$$

where

$$|\text{Error}| = \left| \left[\frac{\vec{k}\cdot(\vec{r}_j-\vec{r}_{j-1})}{2880} \right]^4 e^{-i\vec{k}\cdot\left[\xi\vec{r}_j+(1-\xi)\vec{r}_{j-1} \right]} \right|_{0<\xi<1} = \frac{\epsilon_j^4}{180}$$

The accuracy is now to the third order in ϵ_j as shown in

$$\frac{\sin \epsilon_j}{\epsilon_j} \approx \frac{1}{3} \cos \epsilon_j + \frac{2}{3}$$

$$= \frac{1}{3} \left(1 - \frac{\epsilon_j^2}{2} + \frac{\epsilon_j^4}{24} \ldots \right) + \frac{2}{3}$$

$$= 1 - \frac{\epsilon_j^2}{6} + \frac{\epsilon_j^4}{72} \ldots$$

We have increased the accuracy of our approximation but we needed one more exponential so it increased the complexity of our algorithm.

A compromise is to use a gaussian type formula for I_j[35], keeping the approximation down to the sum of two exponentials. Using the zeros of the second order Legendre polynomial:

$$P_2(x) = \frac{1}{2}(3x^2-1) = 0$$

which implies $x_1 = +\sqrt{\frac{1}{3}}$ and $x_2 = -\sqrt{\frac{1}{3}}$, we obtain

128

$$I_j = \frac{1}{2}\left\{ e^{-i\vec{k}\cdot\frac{1}{2}\left[(1+3^{-\frac{1}{2}})\vec{r}_j+(1-3^{-\frac{1}{2}})\vec{r}_{j-1}\right]} + e^{-i\vec{k}\cdot\frac{1}{2}\left[(1-3^{-\frac{1}{2}})\vec{r}_j+(1+3^{-\frac{1}{2}})\vec{r}_{j-1}\right]} \right\}$$

+ Error where

$$|\text{Error}| = \left| \left[\frac{\vec{k}\cdot(\vec{r}_j-\vec{r}_{j-1})}{135}\right]^4 e^{-i\vec{k}\cdot\left[\xi\vec{r}_j+(1-\xi)\vec{r}_{j-1}\right]} \right|_{0 < \xi < 1}$$

$$= \frac{16\, e_j^4}{135}$$

So the accuracy is still to the third order in ϵ_j :

$$\frac{\sin \epsilon_j}{\epsilon_j} \simeq \frac{e^{-i\epsilon_j 3^{-\frac{1}{2}}} + e^{i\epsilon_j 3^{-\frac{1}{2}}}}{2}$$

$$= \cos\left(\frac{\epsilon_j}{3^{\frac{1}{2}}}\right) = 1 - \frac{\epsilon_j^2}{6} + \frac{\epsilon_j^4}{216} \cdots$$

129

Appendix II

PERFORMING A 2N-POINT TRANSFORM BY MEANS OF AN N-POINT TRANSFORM

The imaginary part of a complex function can be used advantageously to compute the transform of a real function $F(n)$ defined by $2N$ samples by using a discrete transform which sums only over N values. That is, we wish to break the $2N$ point function $F(n)$ into two N sample functions. We divide $F(n)$ as follows:

$$h(n) = F(2n)$$
$$g(n) = F(2n+1) \qquad n = 0, 1, \ldots, N-1$$

That is, function $h(n)$ is equal to the even numbered samples of $F(n)$, and $g(n)$ is equal to the odd numbered samples. (Note that $h(n)$ and $g(n)$ are not the even and odd function decomposition of $F(n)$.) The discrete Fourier transform[45] can then be written as

$$
\begin{aligned}
\hat{F}(k) &= \sum_{n=0}^{2N-1} F(n)\, e^{-i2\pi kn/2N} \\
&= \sum_{n=0}^{N-1} F(2n)\, e^{-i2\pi k(2n)/2N} + \sum_{n=0}^{N-1} F(2n+1)\, e^{-i2\pi k(2n+1)/2N} \\
&= \sum_{n=0}^{N-1} F(2n)\, e^{-i2\pi kn/N} + e^{-i\pi k/N} \sum_{n=0}^{N-1} F(2n+1)\, e^{-i2\pi kn/N} \\
&= \sum_{n=0}^{N-1} h(n)\, e^{-i2\pi kn/N} + e^{-i\pi k/N} \sum_{n=0}^{N-1} g(n)\, e^{-i2\pi kn/N} \\
&= \hat{h}(k) + e^{-i\pi k/N}\, \hat{g}(k) , \quad k = 0, 1, \ldots, N-1 \qquad\qquad \text{(AII.1)}
\end{aligned}
$$

To efficiently compute $\hat{h}(k)$ and $\hat{g}(k)$, let

$$y(n) = h(n) + i\, g(n) .$$

That is, $y(n)$ is constructed to be the sum of two real functions where one of these real functions is taken to be imaginary. From the linearity property[45], the discrete Fourier transform of $y(n)$ is given by

130

$$\hat{y}(k) = \hat{h}(k) + i \hat{g}(k)$$

$$= (\hat{h}_r(k) + i \hat{h}_i(k)) + i(\hat{g}_r(k) + i \hat{g}_i(k))$$

$$= (\hat{h}_r(k) - \hat{g}_i(k)) + i(\hat{h}_i(k) + \hat{g}_r(k))$$

$$= R(k) + i I(k)$$

where we used the decomposition into their real and imaginary parts for $\hat{h}(k)$ and $\hat{g}(k)$. We decompose both $R(k)$, the real part of $\hat{y}(k)$, and $I(k)$, the imaginary part of $\hat{y}(k)$, into even and odd components[36]

$$\hat{y}(k) = \tfrac{1}{2}(R(k) + R(N-k)) + \tfrac{1}{2}(R(k) - R(N-k))$$

$$+ i \tfrac{1}{2}(I(k) + I(N-k)) + i \tfrac{1}{2}(I(k) - I(N-k))$$

Knowing that a real even, a real odd, an imaginary even or an imaginary odd function transforms respectively into a real even, an imaginary odd, an imaginary even or a real odd function[36], we have

$$\hat{h}(k) = \tfrac{1}{2}(R(k) + R(N-k)) + i \tfrac{1}{2}(I(k) - I(N-k))$$

and
$$(AII.2)$$

$$\hat{g}(k) = \tfrac{1}{2}(I(k) + I(N-k)) - i \tfrac{1}{2}(R(k) - R(N-k))$$

Substitution of (AII.2) into (AII.1) yields

$$\hat{F}(k) = \hat{F}_r(k) + i \hat{F}_i(k)$$

where the real part of the discrete Fourier transform of the 2N sample function $F(n)$ is

$$\hat{F}_r(k) = \tfrac{1}{2}(R(k) + R(N-k)) + \tfrac{1}{2}\cos(\pi k/N)(I(k) + I(N-k))$$

$$- \tfrac{1}{2}\sin(\pi k/N)(R(k) - R(N-k)) \qquad (AII.3)$$

and similarly the imaginary part is

131

$$\hat{F}_i(k) = \frac{1}{2}(I(k) - I(N-k)) - \frac{1}{2}\sin(\pi k/N)(I(k) + I(N-k))$$

$$- \frac{1}{2}\cos(\pi k/N)(R(k) - R(N-k)) \qquad \text{(AII.4)}$$

These formulas hold for $k = 0, 1, \ldots, N-1$ but since $F(n)$ is a real function defined by $2N$ samples to start with, its Fourier transform is an hermitian function[36] and the rest of the spectrum is defined from (AII.3) and (AII.4) as follows:

$$\hat{F}_r(N+k) = \hat{F}_r(N-k)$$

$$k = 0, 1, \ldots, N-1$$

$$\hat{F}_i(N+k) = - \hat{F}_i(N-k)$$

As of $\hat{F}(N)$, $\hat{F}_i(N) = 0$ since $F(n)$ is real and we assign $\hat{F}_r(N)$ to be zero through our shape factor.

In a straightforward manner, (AII.3) and (AII.4) can be inverted to yield

$$R(k) = \frac{1}{2}(\hat{F}_r(k) + \hat{F}_r(N-k)) - \frac{1}{2}\cos(\pi k/N)(\hat{F}_i(k) + \hat{F}_i(N-k))$$

$$- \frac{1}{2}\sin(\pi k/N)(\hat{F}_r(k) - \hat{F}_r(N-k))$$

$$I(k) = \frac{1}{2}(\hat{F}_i(k) - \hat{F}_i(N-k)) - \frac{1}{2}\sin(\pi k/N)(\hat{F}_i(k) + \hat{F}_i(N-k))$$

$$+ \frac{1}{2}\cos(\pi k/N)(\hat{F}_r(k) - \hat{F}_r(N-k))$$

Considering the graphical representation of a complex fast Fourier transform[45], the scheme developed above is equivalent to half a level in addition to the $\log_2 N$ levels of the FFT over N points.

Appendix III

VELOCITY OF A SINGLE VISCOUS VORTEX RING

In equation (4.5), we consider a single vortex ring of radius R and of gaussian cross-section σ. We assume that $\sigma^2 \ll R^2$.
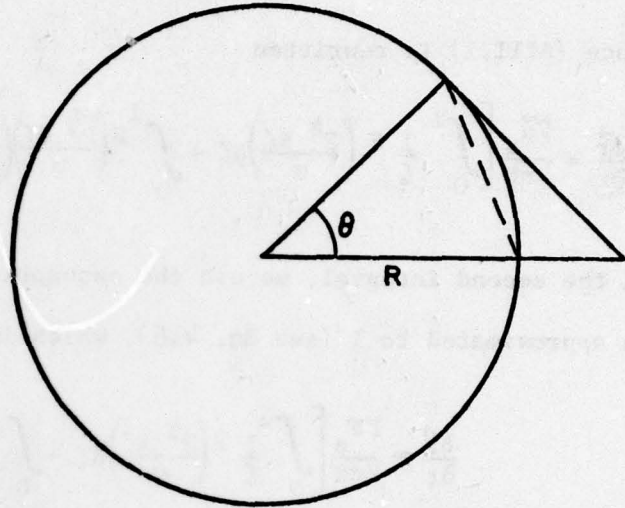
Figure 66.   Vortex ring
of radius R.

From Figure 66, we say that $|\vec{r}| = R$ and that $|\vec{r}-\vec{r}'|$ is the length of the chord subtending the angle θ, therefore $|\vec{r}-\vec{r}'| = 2R \sin(\tfrac{1}{2}\theta)$. By definition of a vector product, we have then

$$(\vec{r}-\vec{r}') \times \frac{\partial\vec{r}'}{\partial\xi} = |\vec{r}-\vec{r}'| \sin(\tfrac{1}{2}\theta) \, \vec{e}_z = 2R \sin^2(\tfrac{1}{2}\theta) \, \vec{e}_z$$

where $\vec{e}_z$ is the unit vector in the direction of translation z. Also, for an arc of θ radians, the length $\xi = R\theta$ so (4.5) becomes

$$\frac{\partial\vec{r}}{\partial t} = \frac{\Gamma\vec{e}_z}{2\pi} \int_0^\pi F\left(\frac{2R \sin(\tfrac{1}{2}\theta)}{\sigma \, 2^{\frac{1}{2}}}\right) \frac{2R^2 \sin^2(\tfrac{1}{2}\theta)}{\left(4R^2 \sin^2(\tfrac{1}{2}\theta)\right)^{3/2}} \, d\theta$$

$$= \frac{\Gamma\vec{e}_z}{4\pi R} \int_0^{\pi/2} F\left(\frac{R 2^{\frac{1}{2}} \sin(\varphi)}{\sigma}\right) \frac{1}{\sin(\varphi)} \, d\varphi$$

Letting $\zeta = \sin(\varphi)$, $d\zeta = \cos(\varphi) \, d\varphi$, so

$$\frac{\partial\vec{r}}{\partial t} = \frac{\Gamma\vec{e}_z}{4\pi R} \int_0^1 F\left(\frac{2^{\frac{1}{2}} R\zeta}{\sigma}\right) \frac{1}{\zeta(1-\zeta^2)^{\frac{1}{2}}} \, d\zeta \qquad\qquad \text{(AIII.1)}$$

133

With ζ ranging from 0 to 1, we can consider a binomial series expansion for $(1-\zeta^2)^{-\frac{1}{2}}$ such that

$$\frac{1}{\zeta(1-\zeta^2)^{\frac{1}{2}}} = \frac{1}{\zeta} + \frac{\zeta}{2} + \frac{3\zeta^3}{8} + \frac{5\zeta^5}{8} + \ldots.$$

Hence (AIII.1) is rewritten

$$\frac{\partial \vec{r}}{\partial t} = \frac{\Gamma \vec{e}_z}{4\pi R}\left[\int_0^1 \frac{1}{\zeta} F\left(\frac{2^{\frac{1}{2}} R\zeta}{\sigma}\right)d\zeta + \int_0^1 F\left(\frac{2^{\frac{1}{2}} R\zeta}{\sigma}\right)\left(\frac{1}{\zeta(1-\zeta^2)^{\frac{1}{2}}} - \frac{1}{\zeta}\right) d\zeta\right] \qquad \text{(AIII.2)}$$

In the second integral, we use the assumption that $\sigma^2 \ll R^2$ so F can be approximated to 1 (see Eq. 4.6), which implies

$$\frac{\partial \vec{r}}{\partial t} \simeq \frac{\Gamma \vec{e}_z}{4\pi R}\left[\int_0^1 \frac{1}{\zeta} F\left(\frac{2^{\frac{1}{2}} R\zeta}{\sigma}\right)d\zeta + \int_0^1 \left(\frac{1}{\zeta(1-\zeta^2)^{\frac{1}{2}}} - \frac{1}{\zeta}\right) d\zeta\right]$$

But

$$\int_0^1 \left(\frac{1}{\zeta(1-\zeta^2)^{\frac{1}{2}}} - \frac{1}{\zeta}\right)d\zeta = \lim_{\epsilon \to 0} \ln\left(\left|1+(1-\epsilon^2)^{\frac{1}{2}}\right|\right)$$

$$= \ln 2$$

So,

$$\frac{\partial \vec{r}}{\partial t} \simeq \frac{\Gamma}{4\pi R}\left[\int_0^1 F\left(\frac{2^{\frac{1}{2}} R\zeta}{\sigma}\right) d\zeta + \ln 2\right]\vec{e}_z$$

Letting $\xi = \frac{2^{\frac{1}{2}} R\zeta}{\sigma}$ and using (4.6),

$$\frac{\partial \vec{r}}{\partial t} \simeq \frac{\Gamma}{4\pi R}\left[\int_0^{2^{\frac{1}{2}} R/\sigma}\left(\frac{1}{\xi} \text{erf}(\xi) - \frac{2}{\pi^{\frac{1}{2}}} e^{-\xi^2}\right) d\xi + \ln 2\right]\vec{e}_z$$

After integrating by parts on the first term of the integrand,

134

$$\frac{\partial \vec{r}}{\partial t} \approx \frac{\Gamma}{4\pi R}\left[\ln\left(\frac{2^{\frac{1}{2}} R}{\sigma}\right)\text{erf}\left(\frac{2^{\frac{1}{2}} R}{\sigma}\right) - \int_0^{2^{\frac{1}{2}} R/\sigma} \frac{2\ln(\xi)\, e^{-\xi^2}}{\pi^{\frac{1}{2}}}\, d\xi\right.$$

$$\left. - \text{erf}\left(\frac{2^{\frac{1}{2}} R}{\sigma}\right) + \ln 2\right] \vec{e}_z$$

Letting $\zeta = \xi^2$, the integral in the above expression becomes

$$\frac{1}{2}\int_0^{2R^2/\sigma^2} \frac{\ln(\zeta)\, e^{-\zeta}}{(\pi\zeta)^{\frac{1}{2}}}\, d\zeta = \frac{1}{2}\int_0^\infty \frac{\ln(\zeta)\, e^{-\zeta}}{(\pi\zeta)^{\frac{1}{2}}}\, d\zeta - \frac{1}{2}\int_{2R^2/\sigma^2}^\infty \frac{\ln(\zeta)\, e^{-\zeta}}{(\pi\zeta)^{\frac{1}{2}}}\, d\zeta$$

Since $\displaystyle\lim_{\zeta\to\infty} \frac{\ln(\zeta)}{\zeta^{\frac{1}{2}}} = 0$, it is safe to say that the second integral of

the right-hand size is of the order e^{-2R^2/σ^2}, so

$$\frac{1}{2}\int_0^{2R^2/\sigma^2} \frac{\ln(\zeta)\, e^{-\zeta}}{(\pi\zeta)^{\frac{1}{2}}}\, d\zeta = \frac{1}{2}\left(- 2\ln(2) - \gamma\right) + 0\left(e^{-2R^2/\sigma^2}\right)$$

where γ is the Euler's constant.

On the other hand, using an asymptotic expansion for the error function, we have

$$\text{erf}\left(\frac{2^{\frac{1}{2}} R}{\sigma}\right) \approx 1 - \frac{\sigma e^{-2R^2/\sigma^2}}{R(2\pi)^{\frac{1}{2}}} + \frac{\sigma^3 e^{-2R^2/\sigma^2}}{R^3(32\pi)^{\frac{1}{2}}} - \ldots \ldots$$

Again, it is safe to say that $\text{erf}\left(\dfrac{2^{\frac{1}{2}} R}{\sigma}\right) \approx 1 - 0\left(e^{-2R^2/\sigma^2}\right)$

asymptotically for $\sigma^2 \ll R^2$.

Finally, we obtain

$$\frac{\partial \vec{r}}{\partial t} \approx \frac{\Gamma}{4\pi R}\left[\ln\left(\frac{2^{\frac{1}{2}} R}{\sigma}\right) + \frac{1}{2}\left(2\ln(2) + \gamma\right) - 1 + \ln(2) + 0\left(e^{-2R^2/\sigma^2}\right)\right]\vec{e}_z \quad \text{(AIII.3)}$$

Hence

$$\frac{\partial \vec{r}}{\partial t} \approx \frac{\Gamma}{4\pi R}\left[\ln\left(\frac{8\,R}{\sigma}\right) - \ln\,(2^{\frac{1}{2}}) + \frac{\gamma}{2} - 1\right]\vec{e}_z$$

or

$$\frac{\partial \vec{r}}{\partial t} \approx \frac{\Gamma}{4\pi R}\left[\ln\left(\frac{8\,R}{\sigma}\right) - C\right]\vec{e}_z \qquad\qquad (AIII.4)$$

where

$$C \approx 1.058$$

136

BIBLIOGRAPHY

1. Rosenhead, L., "The Formation of Vortices from a Surface of Discontinuity", Proc. Roy. Soc. A134, 170-192, 1931.

2. Fink, P. T. and Soh, W. K., "Calculation of Vortex Sheets in Unsteady Flow and Applications in Ship Hydrodynamics", Univ. New South Wales Report, NAV/ARCH 74/1, 1974.

3. Kadomtsev, B. B. and Kostomarov, D. P., "Turbulent Layer in an Ideal Two-Dimensional Fluid", Physics of Fluids 15, 1-3, 1972.

4. Kuwahara, K. and Takami, H., "Numerical Studies of Two-Dimensional Vortex Motion by a System of Point Vortices", J. Phys. Soc. Japan 34, 247-253, 1973.

5. Christiansen, J. P. and Zabusky, N. J., "Instability, Coalescence, and Fission on Finite-Area Vortex Structures", J. Fluid Mech. 61, 219-243, 1973.

6. Chorin, A. J., "Numerical Study of Slightly Viscous Flow", J. Fluid Mech. 57, 785-796, 1973.

7. Ashurst, W. T., "Numerical Simulation of Turbulent Mixing Layers via Vortex Dynamics", Turbulent Shear Flows I, ed. by F. Durst et al., Springer-Verlag, Berlin, 402-413, 1979.

8. Ashurst, W. T., "Vortex Dynamic Calculation of Fluid Motion in a Four Stroke Piston 'Cylinder'--Planar and Axisymmetric Geometry", SAND79-8229. Sandia Labs., Livermore, CA 1978.

9. Shestakov, A. I., "Numerical Solution of the Navier-Stokes Equations at High Reynolds Numbers", Lecture Notes in Physics, Springer-Verlag, 59, 404-409, 1976.

10. Rogallo, R. S., "Discrete Vortex Simulation of Two-Dimensional Incompressible Separated Flows", Proceedings of the Second Computational Fluid Dynamics Conference, AIAA, 67, 1975.

11. Thomson, J.A.L. and Meng, J.C.S., "Studies of Free Buoyant and Shear Flows by the Vortex-in-Cell Method", Lecture Notes in Physics, Springer-Verlag, 35, 401-416, 1974.

12. Meng, J.C.S. and Thomson, J.A.L., "Numerical Studies of Some Nonlinear Hydrodynamic Problems by Discrete Vortex Element Methods", J. Fluid Mech. 84, 433-453, 1978.

13. Michalke, A., "Zur Instabilität und Nichtlinearen Entwicklung einer Gestörten Scherschicht", Ing. Arch. 33, 264-276, 1964.

14. Acton, E., "The Modelling of Large Eddies in a Two-Dimensional Shear Layer", J. Fluid Mech. 76, 561-592, 1976.

15. Christiansen, J. P., "Numerical Simulation of Hydrodynamics by the Method of Point Vortices", J. Computational Physics 13, 363-379, 1973.

16. Aref, H. and Siggia, E. D., "Vortex Dynamics of the Turbulent Shear Layer", Lab. of Atomic and Solid State Physics, Cornell Univ., Ithaca, N.Y. 1979.

17. Wang, S. S., "Grid-Insensitive Computer Simulation of the Kelvin-Helmholtz Instability and Shear Flow Turbulence", Ph.D. thesis, Stanford University Institute for Plasma Research Report No. 710, 1977.

18. Chorin, A. J. and Bernard, P. S., "Discretization of a Vortex Street with an Example of Roll-up", J. Computational Physics 13, 423, 1973.

19. Tennekes, H. and Lumley, J. L., A First Course in Turbulence, M.I.T. Press, 1972.

20. Leonard, A., "Numerical Simulation of Interacting, Three-Dimensional Vortex Filaments", Lecture Notes in Physics, Springer-Verlag, 35, 245-250, 1975.

21. Leonard, A., "Simulation of Three-Dimensional Separated Flows with Vortex Filaments", Lecture Notes in Physics, Springer-Verlag, 59, 280-284, 1976.

22. Meng, J.C.S., "The Physics of Vortex-Ring Evolution in a Stratified and Shearing Environment", J. Fluid Mech. 84, 455-469, 1978.

23. Leonard, A., "Vortex Simulation of Three-Dimensional, Spotlike Disturbances in a Laminar Boundary Layer", Second Symposium on Turbulent Shear Flows, Imperial College, London, 1979.

24. Taylor, G. I. and Green, A. E., "Mechanism of the Production of Small Eddies from Large Ones", Proc. Roy. Soc. A158, 499-521, 1937.

25. Brown, G. L. and Roshko, A., "On Density Effects and Large Structure in Turbulent Mixing Layers", J. Fluid Mech. 64, 775-816, 1974.

26. Winant, C. D. and Browand, F. K., "Vortex Pairing: The Mechanism of Turbulent Mixing-Layer Growth at Moderate Reynolds Number", J. Fluid Mech. 63, 237-255, 1974.

27. Chandrsuda, C., Mehta, R. D., Weir, A. D. and Bradshaw, P., "Effect of Free-Stream Turbulence on Large Structure in Turbulent Mixing Layers", J. Fluid Mech. 85, 693-704, 1978.

28. Ferziger, J. H., "Large Eddy Numerical Simulations of Turbulent Flows", AIAA Journal 15, 1261-1267, 1977.

29. Leonard, A., "Energy Cascade in Large-Eddy Simulations of Turbulent Fluid Flows", Advances in Geophysics 18A, 237-248, 1974.

30. Orszag, S. A. and Patterson, G. S., "Numerical Simulation of Three-Dimensional Homogeneous Isotropic Turbulence", Phys. Rev. Lett. 28, 76-79, 1972.

31. Orszag, S. A. and Raila, D. S., "Test of Spectral Energy Transfer Models of Turbulence Decay", Physics of Fluids 16, 172-173, 1973.

32. Fox, D. G. and Orszag, S. A., "Inviscid Dynamics of Two-Dimensional Turbulence", Physics of Fluids 16, 169-171, 1973.

33. Orszag, S. A., "Numerical Simulation of Incompressible Flows Within Simple Boundaries. I. Galerkin (Spectral) Representations", Studies in Appl. Math. 50, 293-327, 1971.

34. Abernathy, F. H. and Kronauer, R. E., "The Formation of Vortex Streets", J. Fluid Mech. 13, 1-20, 1962.

35. Abramovitz, M. and Stegun, S. A., Handbook of Mathematical Functions, Dover, 1968.

36. Bracewell, R., _The Fourier Transform and its Applications_, McGraw-Hill, 1965.

37. Buneman, O., "Subgrid Resolution of Flow and Force Fields", J. Computational Physics $\underline{11}$, 250, 1973.

38. Buneman, O., "Variationally Optimized, Grid-Insensitive Vortex Tracing", Lecture Notes in Physics, Springer-Verlag, $\underline{35}$, 111-115, 1974.

39. Buneman, O., "The Advance from 2D Electrostatic to 3D Electromagnetic Particle Simulation", Computer Physics Comm. $\underline{12}$, 21-31, 1976.

40. Tung, C. and Ting, L., "Motion and Decay of a Vortex Ring", Physics of Fluids $\underline{10}$, 901-910, 1967.

41. Saffman, P. G., "The Velocity of Viscous Vortex Rings", Studies in Appl. Math. $\underline{44}$, 371, 1970.

42. Henrici, P., _Discrete Variable Methods in Ordinary Differential Equations_, Wiley and Sons, New York, 1962.

43. Hamming, R. W., _Numerical Methods for Scientists and Engineers_, 2nd ed., McGraw-Hill, New York, 1973.

44. Lilly, D. K., "On the Computational Stability of Numerical Solutions of Time-Dependent Non-Linear Geophysical Fluid Dynamics Problems", Mon. Weather Rev. $\underline{93}$, 11-26, 1965.

45. Brigham, E. O., _The Fast Fourier Transform_, Prentice-Hall, New Jersey, 1974.

46. Gradshteyn, I. S. and Ryzhik, I. M., _Table of Integrals, Series and Products_, Academic Press, 4th ed., San Francisco, 1965.

47. Goldstein, S., "Three-Dimensional Vortex Motion in a Viscous Fluid", Phil. Magazine $\underline{30}$, 85-102, 1940.

48. Deissler, R. G., "Nonlinear Decay of a Disturbance in an Unbounded Viscous Fluid", NASA TN D-4947, Appl. Sci. Res. $\underline{21}$, 393-410, 1970.

49. Orszag, S. A., "Numerical Simulation of Incompressible Flows Within Simple Boundaries: Accuracy", SIAM J. Appl. Math. $\underline{49}$, 75-112, 1971.

50. Orszag, S. A., "Numerical Simulation of the Taylor-Green Vortex", _Computing Methods in Applied Science and Engineering_, ed. R. Glowinski and J. L. Lions, Springer-Verlag, 50-64, 1974.

51. Van Dyke, M., "Computer Extension of Perturbation Series in Fluid Mechanics", SIAM J. Appl. Math. $\underline{28}$, 720-733, 1975.

52. Orszag, S. A., "Lectures on Statistical Theory of Turbulence", _Fluid Dynamics_, ed. R. Balian and J. L. Peube, Gordon and Breach, 235, 1977.

53. Betchov, R. and Szewczyk, A. A., "Numerical Study of the Taylor-Green Vortices", Physics of Fluids $\underline{21}$, 871-875, 1978.

54. Orszag, S. A. and Cha-Mei Tang, "Small-Scale Structure of Two-Dimensional Magnetohydrodynamic Turbulence", J. Fluid Mech. $\underline{90}$, 129-143, 1979.

55. Rogallo, R. S., "An ILLIAC Program for the Numerical Simulation of Homogeneous Incompressible Turbulence", NASA Report TM-73, 203, 1977.

56. Orszag, S. A. and Israeli, M., "Numerical Simulation of Viscous Incompressible Flows", _Annual Review of Fluid Mechanics_, ed. M. Van Dyke and W. G. Vincenti, Vol. 6, 1974.

57. Mansour, N. N., Ferziger, J. H. and Reynolds, W. C., "Large-Eddy Simulation of a Turbulent Mixing Layer", Department of Mechanical Engineering Report No. TF-11, 1978.

58. Kelvin, Lord, "Hydrokinetic Solution and Observations", "Influence of Wind and Capillarity on Waves in Water Supposed Frictionless", Mathematical and Physical Papers, Hydrodynamics and General Dynamics, Cambridge, England, 1910.

59. Lamb, Sir Horace, _Hydrodynamics_, Cambridge, England, 1932.

60. Chandrasekhar, S., _Hydrodynamic and Hydromagnetic Stability_, Clarendon Press, Oxford, 1961.

61. Goldstein, S., "On the Stability of Superposed Streams of Fluids of Different Densities", Proc. Roy. Soc. A_132_, 524-548, 1931.

62. Batchelor, G. K., _An Introduction to Fluid Dynamics_, Cambridge Univ. Press, 1974.

63. Landau, L. D. and Lifshitz, E. M., _Fluid Mechanics_, The Addison-Wesley Series in Advanced Physics, Vol. 6, 1959.

64. Hockney, R. W., Goel, S. P. and Eastwood, J. W., "Quiet High-Resolution Computer Models of a Plasma", J. Computational Physics _14_, 148-158, 1974.

65. Lindman, E. L., "'Free-Space' Boundary Conditions for the Time Dependent Wave Equation", J. Computational Physics _18_, 66, 1975.

66. James, R. A., "The Solution of Poisson's Equation for Isolated Source Distributions", J. Computational Physics _25_, 71-93, 1977.

67. Cain, A., Ferziger, J. H. and Reynolds, W. C., "Application of Fourier Methods to Infinite Domains", AIAA 4th Computational Fluid Dynamics Conference, Virginia, July 1979.